UNIVERSIDADE FEDERAL DE SANTA CATARINA
CAMPUS UNIVERSITÁRIO - CENTRO DE CIÊNCIAS FÍSICAS E MATEMÁTICA
PROGRAMA DE PÓS-GRADUAÇÃO EM FÍSICA

Guilherme Luiz Zanin

Quantum Thermodynamics with Photonic Systems

Florianópolis
2021

Guilherme Luiz Zanin

Quantum Thermodynamics with Photonic Systems

Tese submetida ao Programa de Pós-Graduação em Física da Universidade Federal de Santa Catarina para a obtenção do título de Doutor em Física.
Supervisor: Prof. Dr. Paulo Henrique Souto Ribeiro

Florianópolis
2021

Ficha de identificação da obra elaborada pelo autor,
através do Programa de Geração Automática da Biblioteca Universitária da UFSC.

Zanin, Guilherme Luiz
Quantum Thermodynamics with Photonic Systems / Guilherme Luiz Zanin ; orientador, Paulo Henrique Souto Ribeiro , 2021.
112 p.

Tese (doutorado) - Universidade Federal de Santa Catarina, Centro de Ciências Físicas e Matemáticas, Programa de Pós-Graduação em Física, Florianópolis, 2021.

Inclui referências.

1. Física. 2. Termodinâmica Quântica. 3. Óptica Quântica. 4. Conversão Paramétrica Descendente Espontâneaânea . I. , Paulo Henrique Souto Ribeiro. II. Universidade Federal de Santa Catarina. Programa de Pós-Graduação em Física. III. Título.

Guilherme Luiz Zanin

Quantum Thermodynamics with Photonic Systems

O presente trabalho em nível de doutorado foi avaliado e aprovado por banca examinadora composta pelos seguintes membros:

Prof. Dr. Stephen Patrick Walborn
Universidad de Concepción

Prof. Dr Antonio Zelaquett Khoury
Universidade Federal Fluminense

Prof. Dr. Andrew Forbes
University of the Witwatersrand

Certificamos que esta é a **versão original e final** do trabalho de conclusão que foi julgado adequado para obtenção do título de Doutor em Física.

ICP-Edu
Documento assinado digitalmente
Paulo Henrique Souto Ribeiro
Data: 14/09/2021 18:11:21-0300
CPF: 730.886.506-10
Verifique as assinaturas em https://v.ufsc.br

Coordenação do Programa de
Pós-Graduação

ICP-Edu
Documento assinado digitalmente
Paulo Henrique Souto Ribeiro
Data: 14/09/2021 18:10:36-0300
CPF: 730.886.506-10
Verifique as assinaturas em https://v.ufsc.br

Prof. Dr. Paulo Henrique Souto Ribeiro
Supervisor:

Florianópolis, 2021.

This work is dedicated to Railson Mascena Marques.

ACKNOWLEDGEMENTS

First of all, I need to thank my parents, who supported me in all my life decisions. Especially when I decided to study physics (even not believing that I would succeed because I was too lazy, they were still there!).

It’s hard to mention every small contribution that helped me be here. But, at least, in my opinion, every thesis has the participation of many persons in small steps for the final goal.

In between all these contributions, the most important is, of course, Paulão that helped me with any stupid doubts or experimental issues that I have. He also assisted in all possible opportunities to grow, like the proposal for the Ph.D. Sandwich. However, the most important point is that Paulão believed that theoreticians could become experimentalist without damaging any equipment. As a result, I can say that I never burned equipment (except Marcelo’s arm with a near ultra-violet laser in the first week). In the Lab, I can’t forget to mention my day that finished at 3am (at the bar) with Williams (everyone commit this mistake once) and Marcelo! After that day, the friendship with them and professor Renné, André, Gustavo, Thomas just grow!

Then the period in Vienna came! A new country, Lab, friends, supervisors, and research line. Where I also had a really good time and make several friends. First, I need to thank you, Philip Walther, who gave me all the support during my Ph.D. Sandwich. He also believed in me when I proposed an experiment and needed financial support to keep working longer than my fellowship. Second, between my supervisors, I need to give a special thank you to Lee and Maxime. Without their help, I would not have the two amazing works that came out in this period.

I also need to thank the CNPq (National council for scientific development - Brazil), who gave me financial support in the national and international fellowship during my Ph.D. The PPGFSC also gave me fantastic support during my Ph.D., in special Antonio and Ivan.

Last but not least. Bárbara, my wife, helped me by listening to me complaining in the bad moments and screaming (of happiness) in the good ones even if she doesn’t understand what I was talking about.

” All that is gold does not glitter,
Not all those who wander are lost;
The old that is strong does not wither,
Deep roots are not reached by the frost.

From the ashes a fire shall be woken,
A light from the shadows shall spring;
Renewed shall be blade that was broken,
The crownless again shall be king.”

J.R.R. Tolkien, The Fellowship of the Ring, 1954

RESUMO

À medida que os sistemas se tornam menores, chegando a escalas quase atômicas, os efeitos quânticos tornam-se cada vez mais presentes. Nessa linha, tem crescido o interesse pelo estudo da termodinâmica quântica. No entanto, os arranjos experimentais para realizar esses estudos com átomos podem ser complicados, pois requerem sistemas como armadilhas magneto-ópticas. Por outro lado, os fótons são estáveis, relativamente fáceis de produzir e manipular. O principal problema é que os fótons não têm níveis de energia ou massa. Para contornar este problema, usamos uma analogia entre a equação de onda paraxial e a equação de Schrodinger 2D para implementar uma simulação experimental de sistemas quânticos. Nessa analogia, uma medida em momento angular orbital (OAM) está relacionada a uma medida projetiva em energia, permitindo-nos em condições adequadas estudar a Termodinâmica Quântica com sistemas fotônicos. Demonstramos como implementar e manipular estados térmicos usando OAM como um grau de liberdade. Dentro do contexto da Termodinâmica Quântica, também implementamos o primeiro Demônio de Maxwell fotônico com feed-forward ativo usando "interruptores ópticos ultrarrápidos"(UFOS), onde também estudamos como banhos térmicos com correlações poderiam aumentar o poder do Demônio. O último experimento aqui apresentado está fora do contexto da termodinâmica, onde implementamos um protocolo de feed-forward baseado em fibra com o UFOS, permitindo-nos preparar estados de fóton único em polarização com alta fidelidade.

Palavras-chave: Termodinâmica Quântica. Fótons. Feed-forward.

RESUMO EXTENDIDO

Introdução - No final do século XIX/início do século XX, Plank [1, 2] resolveu o problema da radiação do corpo negro, onde introduziu o conceito de que as oscilações atómicas dentro das paredes da cavidade têm valores discretos de energia. Foi o primeiro passo para o desenvolvimento do que viria a ser a mecânica quântica. Foi contra intuitivo na altura, pois a comunidade científica acreditava que a energia era uma quantidade intrinsecamente contínua. Einstein explicou o efeito fotoelétrico [3] descrevendo a luz como pequenos pacotes de energia de $E = h\nu$, que ficou conhecido como um fóton. Usando o mesmo conceito, Einstein desenvolveu também a teoria da emissão estimulada [4, 5], de onde T. H. Maiman [6] foi capaz de construir o primeiro laser (light amplification by stimulated emission of radiation) - amplificação de luz por emissão estimulada de radiação.

A invenção do laser cria a possibilidade de um mundo inteiramente novo na óptica. Esta nova fonte de luz produziu feixes com uma direção de propagação bem definida, espectro de frequência estreito e elevado grau de coerência. Além disso, iniciou uma nova era no estudo da óptica não-linear. Em particular o processo óptico não linear de Conversão Paramétrica Espontânea Descendente (CPDE) surgiu como um sistema interessante e potencialmente útil [7, 8]. Os pares de fótons gerados por SPDC estão emaranhados, o que significa que partilham correlações mesmo à distância.

Os campos produzidos pela CPDE são naturalmente correlacionados em graus de liberdade como frequência e tempo [9], posição e momentum [10], Momento Angular Orbital (MAO) [11] e no número de fótons. Eles também podem ser preparados em estados emaranhados de polarização usando uma variedade de estratégias experimentais, como foi demonstrado, por exemplo, na referência [12]. Nesta tese, usamos correlações no MAO descritas no capítulo 2, correlações em polarização descritas no capítulo 3 e as correlações no número de fótons que foram empregadas em um experimento descrito no capítulo 4.

Mais recentemente testemunhamos o desenvolvimento de uma nova disciplina que tenta reconciliar duas teorias distantes: Termodinâmica e Mecânica Quântica. Ela é chamada Termodinâmica Quântica e tem como objetivo estender conceitos de Termodinâmica como entropia, trabalho e calor ao domínio quântico [13]. Além disso, espera-se que o acesso experimental e o alto grau de controle de alguns sistemas quânticos nos permitam encontrar algum tipo de vantagem quântica para os processos da Termodinâmica. No contexto desta tese, estamos interessados na relação de flutuação introduzida por C. Jarzynski [14] no domínio da física clássica e posteriormente estendida aos sistemas quânticos por H. Tasaki [15]. Relaciona o trabalho gerado em um processo com a mudança na energia livre, que é uma quantidade de equilíbrio que é difícil de ser calculada e medida para sistemas com um grande número de partículas. Experiências recentes demonstraram a reconstrução experimental da distribuição de trabalho de um processo, permitindo a verificação da relação de flutuação Jarzynski, usando ressonância magnética nuclear em estado líquido [16] e um único íon preso em um potencial harmônico [17]. Motivados pelo alto grau de controle que é possível obter sobre um sistema óptico, decidimos estudar a termodinâmica quântica usando fótons. Entretanto, os fótons não têm níveis energéticos nem massa, o que é uma desvantagem em comparação com átomos e moléculas para estudar Termodinâmica. Uma maneira de contornar este problema é usar a analogia entre a equação de Schrödinger 2D e a equação de onda paraxial [18, 19]. Esta analogia nos permite implementar uma simulação experimental de sistemas quânticos usando fótons [20, 21]. Sob condições apropriadas, uma medida do momento angular orbital de um fóton é equivalente à medida da energia de um oscilador harmônico quântico. Usando esta abordagem, é possível implementar o chamado protocolo de duas medidas para determinar a distribuição do trabalho de um processo e, em seguida, testar a relação Jarzynski.

Na maioria dos experimentos relativos à Termodinâmica Quântica, os estados térmicos devem ser preparados e manipulados no Laboratório. Para testes experimentais da relação Jarzynski, entretanto, pode ser mais conveniente preparar autoestados de energia, executar o processo e então utilizar estatísticas térmicas no processando de dados, ao invés de preparar os estados térmicos de inicio [20, 21]. Para os fins onde os estados térmicos são necessários, desenvolvemos um método para preparar os estados térmicos MAO de um fotón. Fazemos uso do fato de que os pares de fótons produzidos no CPDE estão naturalmente emaranhados em MAO [11]. Ao medir um dos fótons e realizar o traço sobre o grau de liberdade do MAO, o fóton conjugado é preparado remotamente em estado térmico. Além disso, estudamos o efeito de alguns processos que atuam sobre ele. Um dos processos é a simulação de turbulência atmosférica, que é um processo interessante que aparece naturalmente nos canais de comunicação do espaço livre.

Na linha da termodinâmica clássica, Maxwell propôs a experiência de pensamento [22] conhecida como Demônio de Maxwell, para testar os limites da 2ª lei da termodinâmica. Mais tarde, após algumas reinterpretações, descobriu-se que o paradoxo do Demônio de Maxwell poderia ser explicado em termos de informação (feed-forward – alimentar o sistema) e extração de trabalho. Atualmente, tornou-se possível realizar experimentos que implementam e estudam este e outros aspectos fundamentais da Termodinâmica, como o princípio de Landauer [23–34]. Em sistemas fotônicos M. D. Vidrighin *et. al* [35] apresentaram uma prova de princípio de um Demônio fotônico, no qual dois feixes térmicos em dois modos diferentes são enviados a dois fotodiodos em um circuito onde eles estão a um capacitor com polaridades. Sem a ação do Demônio, a carga líquida no capacitor seria nula, pois ambos os modos têm a mesma temperatura, ou seja, o mesmo número médio de fótons. Ao ajustar um divisor de feixe com baixa refletividade em ambos os modos e detectores de fótons nos braços refletidos, o Demônio adquire a informação sobre qual é o modo com maior número de fótons. Com este conhecimento, ele pode inverter a polaridade dos terminais do capacitor para que seja atingida uma carga líquida. Isso é possível, pois os feixes térmicos têm um efeito de "bunching" (agrupamento). No entanto, eles não implementam a ação de feed-forward no Demônio, realizando somente a análise condicional dos dados.

No capítulo 4, descrevo uma configuração baseada em fibra para implementar um Demônio de Maxwell fotônico com feed-forward ativo, onde podemos variar parâmetros como as informações do Demônio e implementar diferentes tipos de banhos térmicos. Nosso protocolo de feed-forward é baseado em um interruptor óptico ultra-rápido (UFOS – Ultrafast optical switch), um dispositivo baseado em fibra com duas entradas/saídas, e condicionado a um determinado sinal eletrônico, ele cruza ou deixa as entradas/saídas paralelas, selecionando o caminho dos fótons. A operação de troca dos caminhos ópticos é equivalente à troca da polaridade do capacitor. Estudamos primeiro como o Demônio pode aumentar a diferença no número de fótons entre os modos (efeito do Demônio) usando as informações para alimentar o sistema em banhos térmicos não correlacionados produzidos por fontes pseudotérmicas. Também estudamos como um único estado térmico dividido em dois modos não fornece informações úteis para o Demônio, reduzindo seu efeito a zero. Finalmente, fomos além dos banhos térmicos usuais, implementando banhos térmicos correlacionados que foram capazes de superar o desempenho do Demônio em comparação com os não correlacionados. Utilizamos os fótons correlacionados provenientes da CPDE e os estados NOON de dois fótons preparados com um interferômetro do tipo Hong-Ou-Mandel.

A última experiência é a única fora do escopo da termodinâmica quântica. Trata de uma abordagem de preparação remota de estado utilizando feed-forward a qual foi realizada antes do experimento sobre o Demônio Maxwell [35]. No entanto, percebemos que os UFOS seriam adequados para implementar o Demônio de Maxwell fotônico. Este experimento implementa uma preparação remota de estado de um único fóton em uma configuração experimental baseada em fibra, usando apenas componentes ópticos largamente disponíveis no mercado. Na preparação de estado remota, quando projetamos um dos fótons, preparamos remotamente o estado do outro. Entretanto, como a polarização é uma base bidimensional, há duas projeções, a *correta* e a *errada* uma, que ao somarmos ambas as contribuições obtemos um estado misto. Para obter o estado desejado no regime de um único fóton o tempo todo, preparamos inicialmente o estado (Ψ^-), o que significa que se projetarmos o fóton complementar, sabemos exatamente o estado do fóton sinal, e com esta informação, podemos decidir quando o fóton precisa ser corrigido.

Trabalhos anteriores implementaram sistemas para preparação remota de estados de um único fóton com componentes óticos que utilizam o efeito Pockels [36–39] que são dispositivos que podem agir como uma placa de onda controlada por pulsos elétricos. A utilização de três células Pockels permite a transformação de qualquer estado de polarização de um ponto arbitrário para outro na esfera de Poincaré. Entretanto, elas requerem calibrações complexas que produzem erros consideráveis, e requerem até kV para operar. À nossa maneira, implementamos as operações unitárias com placas de ondas fixas, e redirecionamos o caminho dos fótons para as operações unitárias adequadas usando os UFOS. Com este protocolo, alcançamos a maior fidelidade para a preparação remota no regime de um único fóton até o momento, alcançando uma media de 99%.

Os resultados descritos no capítulo 2 foram obtidos em Florianópolis na UFSC, e são resultados preliminares do projeto. Os resultados descritos nos capítulos 3 e 4 foram obtidos na Universidade de Viena, sob a supervisão do Prof. Philip Walther, Lee A. Rozema e Maxime J. Jacquet. Fiquei lá por 18 meses, sendo 14 meses financiados pelo CNPq (Conselho Nacional de Desenvolvimento Científico - Brasil), e durante os últimos quatro meses, fui financiado pelo grupo do Prof. Walther.

Objetivos - O principal objetivo desde trabalho é o estudo experimental de termodinâmica quântica utilizando sistemas fotônicos. Para realizar este estudo queremos implementar experimentalmente a preparação remota de estado térmicos utilizando MAO como grau de liberdade. Discutiremos também como produzir o estado remoto de um únici fóton com uma alta fidelidade utilizando os UFOS para a implementação de um protocolo de feed-forward. Por último discutimos a implementação de um Demônio de Maxwell fotônico com feed-forward ativo. Neste sistema, além dos banhos térmicos usuais, implementamos banhos térmicos com correlações clássicas e demonstramos que eles podem aumentar em até duas ordens de grandezas o efeito do Demônio.

Metodologia - Para a implementação de todos os objetivos utilizam-se os pares fótons emaranhados produzidos pela CPDE. No primeiro trabalho os fótons estão emaranhados nos graus transversais, a partir dos quais utilizamos o emaranhamento em MAO para produzir remotamente os estados térmicos. Estes estados podem ser utilizados nos estudos de termodinâmica quântica com sistemas fotônicos.

No segundo objetivo utilizamos a CPDE para produzir pares de fotos maximamente emaranhados em polarização, os chamados estados de Bell, a partir dos quais ao realizar a projeção de um deles em uma determinada base, produzimos remotamente o estado do outro. Porém esta projeção tem dois estados possíveis o desejado e um ortogonal. Utilizando um sistema experimental baseado nos UFOS, podemos redirecionar os fótons que estão na projeção errada para serem corrigidos. Neste caso quando a projeção desejada é realizada não precisamos agir no sistema, e os fótons com a projeção errada são corrigidos, obtendo assim o estado desejado o tempo todo.

No último sistema também utilizamos os UFOS para implementar um Demônio de Maxwell fotônico. Neste sistema ao realizar medidas, o Demônio obtém informação sobre o sistema e a partir disso pode tomar decisões para aumentar a extração de trabalho no sistema. Além dos estados térmicos usuais, implementamos estados térmicos com correlações, produzidos pela CPDE, demonstrando que estas correlações extras podem aumentar o efeito do Demônio.

Resultados obtidos Nesta tese demonstramos como preparar remotamente um estado térmico utilizando MAO como grau de liberdade. Para tal feito, utilizamos fato de que a CPDE é naturalmente emaranhada em MAO e a distribuição espectral da CPDE em MAO tem o decaimento exponencial característico de um estado térmico. Demonstramos como realizar a preparação remota do estado de polarização de um único fóton com uma alta fidelidade. Para tal realização utilizamos um sistema com feed-forward utilizando os UFOS que nos permitiu corrigir os fótons com estado de polarização errada. Demonstramos com duas famílias de estado que nosso sistema nos permite criar estados com altíssima fidelidade, tendo na média 99%. No último estudo implementamos o primeiro Demônio de Maxwell fotônico com feed-forward ativo em tempo real. Demonstramos também que a utilização de banhos térmicos com correlações clássicas provém informações extras ao Demônio, em relação ao estado térmico clássico, que permite que o Demônio aumente seu efeito.

Palavras-chave: Termodinâmica Quântica. Fótons. Feed-forward.

ABSTRACT

As systems become smaller, going to almost atomic scales, the quantum effects become more and more present. Following this line, the interest in the study of quantum thermodynamics has grown. However, the experimental setups to perform these studies with atoms can be complicated, as they require systems as magneto-optical traps, for example. On the other side, photons are stable, relatively easy to produce and manipulate. The main problem is that photons do not have energetic levels or mass. To overpass this problem, we use an analogy between the paraxial wave equation and the 2D Schrodinger equation to implement experimental simulations of quantum systems. In this analogy, a measurement in orbital angular momentum (OAM) is related to a projective measurement in energy, allowing us in the proper conditions to study Quantum Thermodynamics with photonic systems. Here we demonstrate how to implement and manipulate thermal states using OAM as a degree of freedom. Inside the Quantum Thermodynamics context, we also implemented the first photonic Maxwell's Demon with active feed-forward by using ultra-fast optical switches (UFOS), where we also studied how thermal baths with correlations could enhance the Demon's power. The last experiment presented here is outside the context of thermodynamics, where we implemented a fiber-based photonic feed-forward protocol with the UFOS, allowing us to prepare single-photon states in polarization with high fidelity.

Keywords: Quantum Thermodynamics. Photons. Feed-forward.

LIST OF FIGURES

LIST OF TABLES

CONTENTS

1 INTRODUCTION

At the end of the XIX century/beginning of XXth, Plank [1, 2] solved the black body radiation problem, where he introduced the concept that the atomic oscillations inside the cavity walls have discrete values of energy. It was the first step for the development of what would become quantum mechanics. It was counterintuitive at that time as the scientific community believed that the energy was an intrinsically continuous quantity. Einstein explained the photoelectric effect [3] describing the light as tiny packages of energy of $E = h\nu$, that became known as a photon. Using the same concept, Einstein also developed the theory of the stimulated emission [4, 5], from where T. H. Maiman [6] was able to construct the first laser - light amplification by stimulated emission of radiation.

The invention of the laser creates the possibility of a whole new world in optics. This new light source produced beams with a well-defined direction of propagation, narrow frequency spectrum and high degree of coherence. Moreover, it started a new era in the study of nonlinear optics. In particular the nonlinear optical process of Spontaneous Parametric Down Conversion (SPDC) has emerged as an interesting and potentially useful system [7, 8]. The photon pairs generated by SPDC are entangled, meaning that they share correlations even at a distance.

The fields produced by SPDC are naturally correlated in degrees of freedom like frequency and time [9], position and momentum [10], Orbital Angular Momentum (OAM) [11] and in the photon number. They can also be prepared in polarization-entangled states using a variety of experimental strategies, as it was demonstrated, for instance in Ref. [12]. In this thesis, we have used correlations in OAM, described in chapter 2, polarization correlations, described in chapter 3 and the photon number correlations, which were employed in an experiment described in chapter 4.

More recently, we have witnessed the development of a new discipline that attempts to reconcile two distant theories: Thermodynamics and Quantum Mechanics. It is called Quantum Thermodynamics and aims at extending concepts of Thermodynamics like entropy, work and heat to the quantum domain [13]. Moreover, the experimental access and high degree of control of some quantum systems is expected to allow us to find some kind of quantum advantage for Thermodynamics processes. In the context of this thesis, we are interested the fluctuation relation introduced by C. Jarzynski [14] in the classical physics domain and later extended to quantum systems by H. Tasaki [15]. It relates the work generated in a process with the free energy change, which is an equilibrium quantity that is hard to calculate and measure for systems with a large number of particles.

Recent experiments have demonstrated the experimental reconstruction of the work distribution of a process, allowing the verification of the Jarzynski fluctuation relation, using liquid-state nuclear magnetic resonance [16] and a single ion trapped in a harmonic potential [17]. Motivated by the high degree of control that is possible to achieve over an optical system, we have decided to study quantum thermodynamics using photons. Nevertheless, photons have no energetic levels and no mass, which is a disadvantage in comparison with atoms and molecules for the purpose of studying Thermodynamics. One way around this problem is to use the analogy between the 2D Schrödinger and the paraxial wave equation [18, 19]. This analogy allows us to implement an experimental simulation of quantum systems using photons [20, 21]. Under appropriate conditions, the measurement of the orbital angular momentum of a photon is equivalent of measuring the energy of a quantum harmonic oscillator. Using this approach, it is possible to implement the so called two-measurement protocol for determination of the work distribution of a process and then testing the Jarzynski relation.

In most of the experiments concerning Quantum Thermodynamics, thermal states must be prepared and manipulated in the Laboratory. For experimental tests of the Jarzynski relation however, it may be more convenient preparing energy eigenstates, performing the process for each one at a time and computing the thermal statistics by processing the data, instead of preparing initial thermal states [20, 21]. For the purposes where thermal states are required, we have developed a method for preparing single-photon OAM thermal states. We make use of the fact that the pairs of photons produced in SPDC are naturally entangled in OAM [11]. By measuring one of the photons and performing the trace over the OAM degree of freedom, the conjugate photon is remotely prepared in a thermal state. In addition, we study the effect of a few processes acting on it. One of the processes is simulated atmospheric turbulence, which is an interesting process that naturally appears in free space communication channels.

In the line of classical thermodynamics, Maxwell proposed the thought experiment [22] know as Maxwell's Demon, to test the limits of the 2nd law of thermodynamics. Later on, after some reinterpretations, it was found that the Maxwell's Demon paradox could be explained in terms of information (feed-forward) and work extraction. Nowadays, it has become possible to realize experiments that implement and study this and other fundamental aspects of Thermodynamics, like the Landauer principle [23–34]. In photonic systems M. D. Vidrighin *et. al* [35] presented a proof of principle of a photonic Maxwell's Demon, wherein two thermal beams in two different modes are sent to two photodiodes in a circuit where they are connected with opposite polarities to a capacitor. Without the Demon's action, the net charge in the capacitor would be null as both modes have the same temperature, meaning the same average photon number. By setting a beam-splitter with low reflectivity in both modes and photon detectors in the reflected arms, the Demon acquires the information about what is the mode with higher number of photons. With this knowledge, he can flip the polarity of the capacitor terminals so that a net charge is achieved. It is possible as thermal beams have a bunching effect. However, they do not implement the feed-foward action of the Demon.

In chapter 4, I describe a fiber-based setup to implement a photonic Maxwell Demon with active feed-forward, where we can vary parameters as the Demon's information and implement different types of thermal baths. Our feed-forward protocol is based on an ultrafast optical switch (UFOS), a fiber-based device with two inputs/outputs, and conditioned on a given signal, it crosses or leaves the input/outputs paralell, exchanging the photonic paths or leaving them inaltered. The operation of switching the optical paths is equivalent of switching the capacitor polarity. We first studied how the Demon can increase the difference in the photon number between the modes (Demon's power) using the information to feed the system in uncorrelated thermal baths produced by pseudo-thermal sources. We also studied how a single thermal state split into two modes provides no helpful information for the Demon, reducing his power to zero. Finally, we have gone beyond the usual thermal baths, implementing correlated thermal baths that were able to surpass the Demon's performance compared to uncorrelated ones. We have used SPDC correlated photons and two-photon NOON states prepared with a Hong-Ou-Mandel interferometer.

The last experiment is the only one outside the Quantum Thermodynamics scope. It deals with the feed-forward approach and it was actually realized before the experiment about the Maxwell's Demon [35]. However, we realized that the UFOS scheme would be suitable for implementing the photonic Maxwell's Demon. This experiment implements a single photon remote state preparation in a fiber-based setup using just bulk components. In the remote state preparation, when we project one of the photons, we remotely prepare the state of the other. However, as polarization is a bi-dimensional basis, there are two projections, the *correct* and the *wrong* one, making the final state a mixed state. To obtain a single-photon state in the desired one all the time, we prepare the singlet state ($|\Psi^-\rangle$), meaning that if we project the idler, we know precisely the signal's state, and by this knowledge, we can decide when the photon needs to be corrected.

Previous works have implemented the feed-forward in the single-photon preparation using Pockels cells [36–39] that are devices that can act as a wave plate by implementing the correct signal. Using three Pockels cells allows the transformation of any polarization state from one point to another arbitrary one in the Poincaré sphere. However, they require complex calibrations that produce considerable errors, and they require up to kV to operate. In our way, we implement the unitary operations by fixed wave plates, and we re-route the path of the photons to proper unitary operations using the UFOS. With this protocol, we achieved the highest average fidelity in this type of remote state preparation to date, achieving 99%.

The results described in chapter 2 were partially obtained in Florianópolis at UFSC. In this thesis, I present the initial results obtained with my participation. The results described in chapters 3 and 4 were obtained at the University of Vienna under the supervision of Profs. Philip Walther, Lee A. Rozema and Maxime J Jacquet. I stayed there for 18 months, wherein 14 months I was funded by CNPq (National council of scientific development - Brazil), and during the last four months, I was funded by Prof. Walther's group.

1.0.1 Outline of the Thesis

In chapter 2, we provide an overview of quantum thermodynamics with structured light, presenting the fundamental concepts and discussing of some previous experiments that have motivate us. We then discuss the implementation of a remote state preparation of a thermal state using orbital angular momentum as a degree of freedom. We then show our experimental results and an initial study of how to control the temperature of the distributions. In the last section, we present our conclusions about the preliminary results.

In chapter 3 we discuss our fiber-based single-photon remote state preparation, where we discuss the theoretical aspects of using polarization as a degree of freedom. We also discuss the theory to project the theoretical and the experimental two-photon state into the projected family of states for the calculus of the fidelity of the states. We show how to prepare each family of states and the relative unitary operation that corrects the state. We demonstrate how the UFOS operate, as they are the core of the experiments in chapter 3 and 4. Finally, in the last subsections, we present the experimental results and discussions.

In chapter 4, we present our photonic Maxwell Demon, providing a discussion about all thermal baths studied and their relation with the Maxwell's Demon thought experiment. We also present the theory developed to support the experimental data. In the last sections, we show the experimental implementation and results for all baths analyzed. Finally, in the last section, we discuss our conclusions and future perspectives.

1.0.2 List of Publications

1. **G. L. Zanin**, M. Antesberger, M. J. Jacquet, P. H. S. Ribeiro, L. A. Rozema, P.Walther, Enhanced Photonic Maxwell's Demon with Correlated Baths, **2021** - arXiv:2107.09686

2. **G. L. Zanin**, M. J. Jacquet, M. Spagnolo, P. Schiansky, I. A. Calafell, L. A.Rozema, P. Walther, "Fiber-compatible photonic feed-forward with 99% fidelity", Optics Express **2021**, 29, 3425–3437.

3. P. H. Souto Ribeiro, T. Häffner, **G. L. Zanin**, N. Rubiano da Silva, N. Rubiano, R. Medeiros de Araújo, W. C. Soares, R. J. de Assis, L. C. Céleri and A. Forbes, "Experimental study of the generalized Jarzynski fluctuation relation using entangled photons", Physical review A **2020**, 101, 052113
4. T. Häffner, **G. L. Zanin**, R. M. Gomes, L. C. Céleri, P. H. S. Ribeiro, “Remote preparation of single photon vortex thermal states”, The European Physical Journal Plus **2020**, 135, 601.
5. **G. L. Zanin**, T. Häffner, M. A. A. Talarico, E. I. Duzzioni, P. H. S. Ribeiro, G. T. Landi, L. C. Céleri, “Experimental Quantum Thermodynamics with Linear Optics”, Brazilian Journal of Physics **2019** , 49, 783–798.

The first paper is under review at Physical Review X.

2 EXPERIMENTAL PHOTONIC RESOURCES FOR QUANTUM THERMODYNAMICS

A beam of light carries angular momentum in two forms. The first form is the spin angular momentum [40] ($\pm\hbar$ per photon), which is related to its polarization. The second form corresponds to the spatial distribution of the wavefronts. M. Padgett & L. Allen [41] demonstrated that helical wavefronts carry orbital angular momentum (OAM). The solutions of the paraxial Helmholtz equation that naturally contain angular momentum are the Laguerre-Gaussian modes $LG_{p\ell}$ [42], in which p is the radial quantum number and ℓ is the azimuthal quantum number. In the results presented in this thesis, we will only be concerned with ℓ, hence for convenience we choose $p = 0$.

This type of beam is widely used due to its easy creation and manipulation [43], besides the applications in classical [44] and quantum [45] communications, and quantum simulations [20]. In the field of communications in specific, LG modes have great applicability because they are a set of modes with arbitrary dimension (qudit), allowing to encode a more significant amount of information in a single photon.

In a previous work of Araújo *et al.* [20], they implemented intense beam with thermal statistics using OAM as a degree of freedom. However, in this project, we will work in the single-photon regime produced by spontaneous parametric down-conversion (SPDC) [46]. SPDC creates a pair of photons that are entangled in their angular spectra [47], as a consequence, they are also entangled in orbital angular momentum [11]. The entanglement between the photon pair will be the crucial tool for the remote preparation of thermal states. J. P. Torres *et al.* [48] showed that the spectrum of the photon pairs in terms of their orbital angular moments has an exponential decay type dependence on the ℓ modulus, the azimuthal quantum number. Furthermore, we can relate photonic states with OAM to two-dimensional quantum oscillators [18, 20]. Thus, we can start from an OAM entangled state of two photons, measure one of the photons (signal), using detection in coincidences to announce the presence of the other photon (idler). If we do not select any value of OAM at the signal, we remotely prepare a thermal state in OAM at the idler. It means that by performing the partial trace at one side, we remotely prepare a thermal state in OAM at the other.

The development of Thermodynamics is a theory that was in the context of macroscopic systems. However, new technologies allow the manipulation of physical systems on ever-smaller scales. In this regime, classical and quantum fluctuations become highly relevant. Fluctuation-dissipation relations have been developed along these lines. In our work, the Jarzynski relation [14] is the chosen one. It establishes a relation between equilibrium quantities, such as free energy, and non-equilibrium quantities, such as the work distribution relative to some physical process. This relation requires that the system be reversible on small time scales (micro-reversibility) and that the system's initial state is thermal. This fluctuation-dissipation relation was initially developed for classical systems, but was quickly extended to quantum systems [15, 49, 50].

To perform the calculations using Jarzynski's relation, it is also necessary to know the work distribution of some process acting on the system in question. For quantum systems, the work is defined as the difference between two projective measurements in energies, requiring the so-called two-measurement protocol. These measurements are non-trivial, making the number of experimental works available in the literature small. The first measurement of a quantum work distribution is from T. Batalhão *et al.* [16] using a nuclear magnetic resonance platform, followed by Shuoming et al. [17] who used ions in a trap. Another work along these lines is the one by R. M. de Araujo *et al.* [20], in which they use the analogy between Schrödinger's equation for a harmonic oscillator in two dimensions and Helmholtz's paraxial wave equation to simulate a quantum system using linear optics. Within this analogy, a measurement in OAM becomes equivalent to a projective measurement in energy. We will use the same analogy in our work to calculate the temperature of the thermal distributions, such as their average energy before and after applied processes.

This chapter is divided as follows: In the first section, we are going to present the fundamental concepts as the Helmholtz paraxial wave equation and its leading solutions (sec. 2.1.1), spontaneous parametric down-conversion and its entanglement in the transverse degrees of freedom (sec. 2.1.2) and the Jarzynski fluctuation-dissipation relation (sec. 2.1.3). The second section presents some previous experiments in quantum thermodynamics with optical systems that motivate the work presented in this and the following chapters. In the third section, the first results related to the remote preparation of a thermal state in OAM and some applications will be presented and the theory that validated the thermal state. The results presented in this thesis were the preliminary results in the project, in which the group finished later and, the final results are published in [51]. In the last section, we will present the conclusions of the results generated in this project.

2.1 FUNDAMENTAL CONCEPTS

In this section, I will present the fundamental concepts required for a better understanding. In section 2.1.1, I will demonstrate the Helmholtz paraxial wave equation and its leading solutions. In section 2.1.2, an explanation is given of how the process of spontaneous parametric down-conversion occurs, focusing on the transverse degrees of freedom and how it applies to our context. In section 2.1.3 we will look at Jarzynski's fluctuation relation, which will be used in the context of quantum thermodynamics.

2.1.1 Paraxial wave equation

The wave equation in Cartesian coordinates has the following form:

$$\nabla^2 U - \frac{1}{c^2}\frac{\partial^2 U(\boldsymbol{r},t)}{\partial t^2} = 0, \tag{2.1}$$

where $c = 1/\mu_0\epsilon_0$ is the speed of light and ∇^2 is the Laplacian operator, which is defined as:

$$\nabla^2 = \frac{\partial^2}{\partial x^2} + \frac{\partial^2}{\partial y^2} + \frac{\partial^2}{\partial z^2}. \tag{2.2}$$

To solve the wave equation, let's propose a solution for a monochromatic wave:

$$U(\boldsymbol{r},t) = U(\boldsymbol{r})e^{-i\omega t}, \tag{2.3}$$

where $U(\boldsymbol{r})$ is the complex amplitude of the wave and ω is its frequency. Substituting the equation 2.3 into equation 2.1 we arrive at the Helmholtz equation:

$$(\nabla^2 + k^2)U(\boldsymbol{r}) = 0, \tag{2.4}$$

with $k = \omega/c$.

A usual light source is a laser that propagates in a well-defined direction (z), without many variations in the other directions during its propagation. It allows us to perform the paraxial approximation, in which we can write our function $U(\boldsymbol{r})$ concerning an envelope function $A(\boldsymbol{r})$, taking into account that its longitudinal components have a tiny variation about e^{ikz}.

$$U(\boldsymbol{r}) = A(\boldsymbol{r})e^{ikz}. \tag{2.5}$$

The function e^{ikz} is a plane wave. We also consider that the envelope function $A(\boldsymbol{r})$ varies slowly in respect to the z-direction, meaning that if the beam propagates a distance $\Delta z = \lambda$, the variations in ΔA are much smaller than A ($\Delta A << A$). The variation of ΔA is $\Delta A = \frac{\partial A}{\partial z}\Delta z = \frac{\partial A}{\partial z}\lambda$, from which we can calculate the derivatives:

$$\frac{\partial A}{\partial z} << kA \rightarrow \frac{\partial^2 A}{\partial z^2} << k^2 A. \tag{2.6}$$

We can observe that the first derivative is small, showing that the second one is even smaller, allowing us to discard this therm. Substituting the paraxial equation (eq. 2.5) into the Helmholtz equation (eq. 2.4) and neglecting the second derivative in z concerning the first one, we obtain:

$$\nabla_T^2 A + i2k\frac{\partial A}{\partial z} = 0, \tag{2.7}$$

where $\nabla_T^2 = \partial^2 A/\partial x^2 + \partial^2 A/\partial y^2$ is the Laplace operator in the transverse coordinates.

2.1.1.1 Gaussian Solution

The simplest solution of the paraxial Helmholtz equation is the paraboloidal wave:

$$A(\boldsymbol{r}) = \frac{A_1}{q(z)} exp\left[-ik\frac{\rho^2}{2q(z)}\right], \tag{2.8}$$

from which we obtain the Gaussian solution by considering $q(z) = z + iz_0$, where z_0 is the Rayleigh range. In order to separate the amplitude and phase of the complex envelope, we will rewrite $1/q(z)$ concerning its real $R(z)$ and complex $W(z)$ parts:

$$\frac{1}{q(z)} = \frac{1}{R(z)} - i\frac{\lambda}{\pi W^2(z)}, \tag{2.9}$$

where $R(z)$ is the curvature of the wavefront and $W(z)$ is the beam width. Substituting the equation 2.9 into 2.8 and using the paraxial equation (eq. 2.5) we obtain the following form for the Gaussian wave function:

$$U(\boldsymbol{r}) = A_0\frac{W_0}{W(z)} exp\left[-\frac{\rho^2}{W^2(z)}\right] exp\left[-ikz - ik\frac{\rho^2}{2R(z)} + i\zeta(z)\right], \tag{2.10}$$

in which

$$W(z) = W_0\left[1 + \left(\frac{z}{z_0}\right)^2\right]^{\frac{1}{2}} \tag{2.11}$$

$$R(z) = z\left[1 + \left(\frac{z_0}{z}\right)^2\right] \tag{2.12}$$

$$\zeta(z) = tan^{-1}\left(\frac{z}{z_0}\right) \tag{2.13}$$

$$W_0 = \left(\frac{\lambda z_0}{\pi}\right)^{\frac{1}{2}}, \tag{2.14}$$

with $A_0 = A_1/iz_0$. The equations 2.11 to 2.14 are the parameters that completely determine a Gaussian beam.

2.1.1.2 Laguerre-Gaussian solution

Another solution to Helmholtz's paraxial wave equation (eq. 2.7) are the Laguerre-Gaussian (LG) modes. LG modes are the essential solution in the present work because they carry [41] angular orbital momentum (OAM). For this solution, it is necessary to rewrite the Helmholtz paraxial wave equation in cylindrical coordinates:

$$\left(\frac{1}{r}\frac{\partial}{\partial r}\left(r\frac{\partial}{\partial r}\right) + \frac{1}{r^2}\frac{\partial^2}{\partial\phi^2} + 2ik\frac{\partial}{\partial z}\right) LG_{p\ell}(r, \phi, z) = 0. \tag{2.15}$$

LG modes have the following form:

$$\begin{aligned} LG_{p\ell}(r,\phi,z) =& c_{p\ell}\frac{W_0}{W(z)}\left(\frac{\sqrt{2}\rho}{W(z)}\right)^{|\ell|} L_p^{|\ell|}\left(\frac{2\rho^2}{W^2(z)}\right) exp\left(-\frac{\rho^2}{W^2(z)}\right) \\ & \times exp\left[-i\left(\frac{k\rho^2}{2R(z)} + (2p+|\ell|+1)\zeta(z)\right)\right] exp(-i\ell\phi), \end{aligned} \tag{2.16}$$

L_p^ℓ are the Laguerre modes in which ℓ and p are the azimuthal and radial quantum numbers. Figure 1 shows the intensity profile of the LG modes.

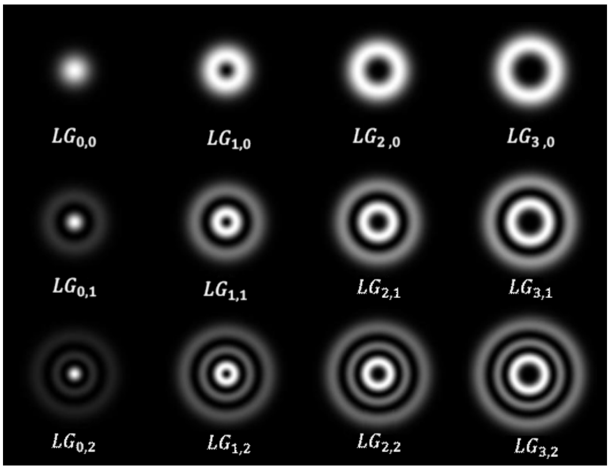

Figure 1 – $LG_{p\ell}$ modes with ℓ from 0 to 3 and p from 0 to 2.

2.1.2 Parametric down-conversion and the entanglement in transverse spatial degrees of freedom.

Parametric down-conversion is a process where a light beam interacts with a non-linear medium. This non-linear medium consists of a birefringent crystal with different refractive indices for different beam propagation directions. The photons from the pump beam are absorbed by the crystal and be re-emitted as a pair of photons, commonly known as twin photons. This process is called spontaneous parametric down-conversion (SPDC). The figure 2 illustrates the process.

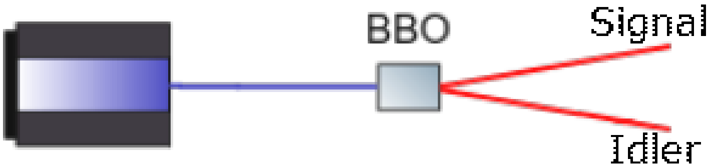

Figure 2 – A laser shines on the nonlinear crystal and creates a pair of photons called signal (s) and idler (i). Where the energy is conserved as in equation 2.18.

This work will focus on the spatial correlations arising from the angular spectrum of photons in the SPDC. Therefore the treatment given will be in the transverse degrees according to the references [52, 53], in which they studied how to manipulate the transferred angular spectrum for twin photons.

We will consider that the pump beam has a wave vector $\boldsymbol{k_p}$ and frequency ω_p. The photon pair, on the other hand, will be called signal (s) and idler (i), having wave vectors $\boldsymbol{k_s}$, $\boldsymbol{k_i}$ and frequencies ω_s, ω_i respectively. Since this process conserves momentum and energy, we have that:

$$\boldsymbol{k_p} = \boldsymbol{k_s} + \boldsymbol{k_i} \tag{2.17}$$

and

$$\omega_p = \omega_s + \omega_i. \tag{2.18}$$

The pump beam is incident on a nonlinear crystal (BBO-type I), located at the origin of the coordinate system, with dimensions (L_x, L_y and L_z). In a multi-mode description [54], the quantum state of the twin photons generated in SPDC is:

$$|\psi\rangle = \alpha\,|vac\rangle + \beta \int d\boldsymbol{k_s} \int d\boldsymbol{k_i} sinc\left[\frac{1}{2}(\omega_s + \omega_i - \omega_p)t\right] \Phi(\boldsymbol{k_s}, \boldsymbol{k_i})\,|1, \boldsymbol{k_s}\rangle\,|1, \boldsymbol{k_i}\rangle\,, \tag{2.19}$$

the first term represents the situation where SPDC did not occur, and the pump beam did not interact with the crystal, and the second term represents the entangled state of the twin photons. We have that α and β are constants such that $\langle\psi|\psi\rangle = 1$, with $|\alpha|^2 \gg |\beta|^2$, i.e., the probability rate of the pump beam not interacting with the crystal is much higher than the rate of a photon pair be created in the SPDC. These probabilities depend on the dimensions and the nonlinearity (χ^2) of the crystal. The phase-matching conditions for the process to occur and the conservation of energy (eq. 2.18) are consequences of the *sinc* function. The polarization labels are present in the wave function, but we omit them in our treatment as our focus is on the transverse degrees of freedom.

The function $\Phi(\boldsymbol{k_s}, \boldsymbol{k_i})$ expresses the emission spectrum of twin photons, and its explicit form is given by:

$$\Phi(\boldsymbol{k_s}, \boldsymbol{k_i}) = \int d\boldsymbol{k_p} V(\boldsymbol{k_p}) \left[\frac{\omega_s \omega_i \omega_p}{n^2(\boldsymbol{k_s}) n^2(\boldsymbol{k_i}) n^2(\boldsymbol{k_p})}\right]^{1/2} \prod_{j=1}^{3} sinc\left[\frac{1}{2}(\boldsymbol{k_s} + \boldsymbol{k_i} - \boldsymbol{k_p})_j L_j\right], \tag{2.20}$$

$V(\boldsymbol{k_p})$ is the angular spectrum of the pump beam in the plane of the crystal, and $n(\boldsymbol{k_i})$ is the linear refractive index of the crystal.

From now on, we will apply some approximations on the twin photons state, equation 2.19, referring to the type of analysis we wish to perform, relating it to the experimental apparatus that we work with. We will consider that the angular frequencies of interest are well defined using interference filters and narrow bandwidth (≈ 10 *nm*).

In our case, the pump beam has a wavelength of 405 *nm*, and the pair of photons of interest has a wavelength of 810 *nm*. We can treat our system as monochromatic, writing $\omega_s + \omega_i = \omega_p$. This allows us to perform the following approximation on the *sinc* function at equation 2.19:

$$sinc\left[\frac{1}{2}(\omega_s + \omega_i - \omega_p)t\right] = 1. \tag{2.21}$$

We will consider that the three beams (pump, signal, and idler) propagate close to their propagation axes, making $|\boldsymbol{k}| \gg |\boldsymbol{q}|$, where $\boldsymbol{q}$ is the transverse component of the wave vector $\boldsymbol{k}$. Since the refractive indices can be considered approximately constant, let us assume that the transverse dimensions of the crystal (L_x and L_y) are large compared to the inverse of the modulus of the transverse components of its wave vectors and that L_z is small compared to the inverse of the modulus of the longitudinal wave vectors. We then obtain:

$$sinc\left[\frac{1}{2}(\boldsymbol{k_s} + \boldsymbol{k_i} - \boldsymbol{k_p})_x L_x\right] sinc\left[\frac{1}{2}(\boldsymbol{k_s} + \boldsymbol{k_i} - \boldsymbol{k_p})_y L_y\right] \approx \delta(\boldsymbol{q_s} + \boldsymbol{q_i} - \boldsymbol{q_p}) \tag{2.22}$$

and

$$sinc\left[\frac{1}{2}(\boldsymbol{k_s} + \boldsymbol{k_i} - \boldsymbol{k_p})_z L_z\right] \approx 1. \tag{2.23}$$

Since we are in the monochromatic approximation $\boldsymbol{k_p}$ is constant, then $\int d\boldsymbol{k_p} \to \int d\boldsymbol{q_p}$ and $V(\boldsymbol{k_p}) \equiv V(\boldsymbol{q_p})$. With this we obtain:

$$\Phi(\boldsymbol{k_s}, \boldsymbol{k_i}) \approx \int d\boldsymbol{q_p} V(\boldsymbol{q_p})\delta(\boldsymbol{q_s} + \boldsymbol{q_i} - \boldsymbol{q_p}) = V(\boldsymbol{q_s} + \boldsymbol{q_i}). \tag{2.24}$$

With all these approximations, the equation state for the SPDC (eq. 2.19) in the transverse degrees of freedom becomes:

$$|\psi\rangle = \alpha\,|vac\rangle + \beta \int d\boldsymbol{q_s} \int d\boldsymbol{q_i} V(\boldsymbol{q_s} + \boldsymbol{q_i})\,|1, \boldsymbol{q_s}\rangle\,|1, \boldsymbol{q_i}\rangle\,. \tag{2.25}$$

Analyzing $|\psi\rangle$ it can be seen that this state is entangled in the transverse degree of freedom, since it is not possible to separate the probability amplitude, as $V(\boldsymbol{q_s} + \boldsymbol{q_i}) \neq V(\boldsymbol{q_s})V(\boldsymbol{q_i})$, due to the fact that $\boldsymbol{q_p} = \boldsymbol{q_s} + \boldsymbol{q_i}$. This fact demonstrates the transfer of the angular spectrum of the pump beam to the twins photons state.

To observe the effect of the transfer of the angular spectrum of the pump beam, we will calculate the single counts and coincidence counts, considering that we will detect the signal and idler photons at the $\boldsymbol{r_s}$ and $\boldsymbol{r_i}$ positions, respectively. It is necessary to take into account that the aperture of the detector is small. Figure 3 illustrates the process of simple and coincidence counts.

The single count rate for the signal (idler) is $S(\boldsymbol{r_s})$ ($S(\boldsymbol{r_i})$) is proportional to the 2nd order correlation function $G^{(1,1)}(\boldsymbol{r_i}, \boldsymbol{r_i}) = \langle\psi|\,\hat{E}_i^{(-)}(\boldsymbol{r_i})\hat{E}_i^{(+)}(\boldsymbol{r_i})\,|\psi\rangle$, where $\hat{E}_i^{(-)}(\boldsymbol{r_i})$ and $\hat{E}_i^{(+)}(\boldsymbol{r_i})$ represent the operators of the electric field of the signal and idler. The field

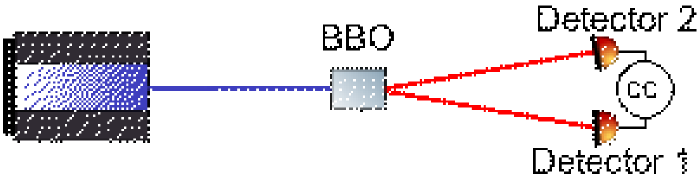

Figure 3 – This figure illustrates the process of detection for the signal and idler beams. In single counts, we record the number of photons detected in a given time. In the case of coincidence counts, the detector that registers a photon triggers the window of coincidence, in our case 5 *ns*, and if the other photon clicks in this interval, we consider it a coincidence. An FPGA analyzes the electrical pulses coming from each detector to determine whether or not it was a coincidence detection.

contains all the information about the optical components inserted in the propagation path. In our case, the propagation will be along the z axis. Let us then write the electric field operator in terms of plane waves:

$$\hat{E}_i^{(+)}(\boldsymbol{r_i}) = \frac{i}{(2\pi)^{2/3}} \int d\boldsymbol{k_i} \sqrt{\frac{\hbar\omega_i}{2\epsilon_0}}\hat{a}(\boldsymbol{k_i}) exp[i\boldsymbol{k_i} \cdot \boldsymbol{r_i}], \tag{2.26}$$

where $\hat{a}(\boldsymbol{k_i})$ is the annihilation operator for a mode with $\boldsymbol{k_i}$ and $\hat{E}_i^{(-)}(\boldsymbol{r_i}) = \left[\hat{E}_i^{(+)}(\boldsymbol{r_i})\right]^{\dagger}$. Using the paraxial approximation, we obtain:

$$exp\left[i\boldsymbol{k_i} \cdot \boldsymbol{r_i}\right] \approx exp\left[i\left(\rho_i \cdot q_i - \frac{q_i^2}{2k_i^2} z_i\right)\right], \tag{2.27}$$

where $\boldsymbol{r} = (\rho_x, \rho_y, z)$ and $\boldsymbol{k_i} = (q_x, q_y, k_z)$. It has been taken into account that $k_i \gg q_i$. The field becomes:

$$\hat{E}_i^{(+)}(\boldsymbol{r_i}) = i\sqrt{\frac{\hbar\omega_i}{16\pi^3\epsilon_0}} e^{ik_i z} \int d\boldsymbol{q_i} \hat{a}(\boldsymbol{q_i}) exp\left[i\left(\rho_i \cdot q_i - \frac{q_i^2}{2k_i^2} z_i\right)\right]. \tag{2.28}$$

Using this field, the single count rate for the signal beam becomes:

$$\begin{aligned} S(\rho_s, z_s) &\propto \left|\hat{E}_s^{(+)}(\boldsymbol{r_s})\left|\psi\right\rangle\right|^2 \\ &\propto \left|\int d\boldsymbol{q'_s} \hat{a}(\boldsymbol{q'_s}) exp\left[i\left(\rho_s \cdot q'_s - \frac{q_s'^2}{2k'_s} z_s\right)\right]\right. \\ &\quad \times \left.\left[\left|vac\right\rangle + \int d\boldsymbol{q_s} \int d\boldsymbol{q_i} V(\boldsymbol{q_s} + \boldsymbol{q_i}) \left|1, \boldsymbol{q_s}\right\rangle \left|1, \boldsymbol{q_i}\right\rangle\right]\right|^2. \end{aligned} \tag{2.29}$$

To perform the integrals in equation 2.29, we will rewrite the angular spectrum of the pump beam in its Fourier integral representation:

$$V(\boldsymbol{q_s} + \boldsymbol{q_i}) = c \int d\rho W(\rho) exp\left[-i(\boldsymbol{q_s} + \boldsymbol{q_i}) \cdot \rho\right]. \tag{2.30}$$

We need to use the commutation relations between the annihilation and creation operators $[a(q'_S), a^{\dagger}(q_S)] = \delta(q'_S - q_S)$.

The single count rate becomes:

$$\begin{aligned}S(\rho_S, z_S) \propto \int d\boldsymbol{q'_s} \int d\boldsymbol{q'_i} \int d\rho' W^{*}(\rho') exp\left[i\left(\boldsymbol{q'_s} - \boldsymbol{q'_i}\right)\rho'\right] exp\left[-i\left(\boldsymbol{q'_s}\rho_{\boldsymbol{s}} - \frac{q_S'^2}{2k_S} z_S\right)\right] \\ \times \int d\boldsymbol{q_s} \int d\boldsymbol{q_i} \int d\rho W(\rho) exp\left[-i\left(\boldsymbol{q_s} - \boldsymbol{q_i}\right)\rho\right] exp\left[i\left(\boldsymbol{q_s}\rho_{\boldsymbol{s}} - \frac{q_S^2}{2k_S} z_S\right)\right] \\ \times \delta(\boldsymbol{q'_i} - \boldsymbol{q_i}).\end{aligned} \tag{2.31}$$

The integral in $\boldsymbol{q_s}$ is a Gaussian integral and has the following result:

$$\int d\boldsymbol{q_s} exp\left\{i\left[(\rho_{\boldsymbol{s}} - \rho)\boldsymbol{q_s} - \frac{q_S^2}{2k_S} z_S\right]\right\} = Cexp\left[i|\rho_{\boldsymbol{s}} - \rho|^2 \frac{k_S^2}{2z_S}\right]. \tag{2.32}$$

After performing integrations and simplifications, we arrive at the following expression for the single count rate:

$$S(\rho_S, z_S) \propto \int d\rho \left|W(\rho)\right|^2. \tag{2.33}$$

After analyzing the single count rate expression, it is possible to observe that it depends only on the intensity of the pump beam, i.e., the angular spectrum of the pump beam does not affect the simple count rate distribution.

We then want to observe if it is possible to observe the transfer of the angular spectrum of the pump beam to the coincidence rate $C(\boldsymbol{r_s}, \boldsymbol{r_i})$ between twin photons. This rate is proportional to the fourth-order correlation function and has the following form:

$$C(\boldsymbol{r_s}, \boldsymbol{r_i}) \propto G^{2,2}(\boldsymbol{r_s}, \boldsymbol{r_i}) = \langle\psi| \hat{E}_S^{(-)}(\boldsymbol{r_s})\hat{E}_i^{(-)}(\boldsymbol{r_i})\hat{E}_i^{(+)}(\boldsymbol{r_i})\hat{E}_S^{(+)}(\boldsymbol{r_s})|\psi\rangle, \tag{2.34}$$

rewriting it in terms of the field operators: (eq. 2.26)

$$\begin{aligned}C(\boldsymbol{r_s}, \boldsymbol{r_i}) \propto \Bigg|\int d\boldsymbol{q_s} \int d\boldsymbol{q_i} V(\boldsymbol{q_s} + \boldsymbol{q_i}) exp\left[i\left(\boldsymbol{q_s}\cdot\rho_{\boldsymbol{s}} - \frac{q_S^2}{2k_S} z_S\right)\right] \\ \times exp\left[i\left(\boldsymbol{q_i}\cdot\rho_{\boldsymbol{i}} - \frac{q_i^2}{2k_i} z_i\right)\right]\Bigg|^2.\end{aligned} \tag{2.35}$$

The resolution process is similar to that of single counts, using the equations 2.30 and 2.32 we obtain:

$$C(\boldsymbol{r_s}, \boldsymbol{r_i}) \propto \left|\int d\rho W(\rho) exp\left[i\frac{k_p}{2Z_0}\left|\boldsymbol{R} - \rho\right|^2\right]\right|^2, \tag{2.36}$$

with

$$\frac{1}{Z_0} = \frac{k_S}{k_p}\frac{1}{z_S} + \frac{k_i}{k_p}\frac{1}{z_i} \tag{2.37}$$

and

$$\boldsymbol{R} = \frac{Z_0}{z_s}\frac{k_s}{k_p}\boldsymbol{\rho_s} + \frac{Z_0}{z_i}\frac{k_i}{k_p}\boldsymbol{\rho_i}. \tag{2.38}$$

The integral in equation 2.36 describes the propagation of the pump beam from the position $z = 0$ (crystal) to the plane $z = z_0$ in the paraxial approximation. Solving the integral we obtain:

$$C(\boldsymbol{r_s}, \boldsymbol{r_i}) \propto \left| W(\boldsymbol{R}, Z_0) \right|^2. \tag{2.39}$$

The coincidence rate is dependent on the intensity distribution of the pump beam at position Z_0. This effect comes from the transfer of the angular spectrum of the pump beam. If we insert an object like a slit or lens into the pump beam before the crystal, it will modify the profile formed at z_0 to the coincidence counts between the twin photons.

Among the studies of entanglement in spatial modes, it was demonstrated that spontaneous parametric down-conversion conserves angular momentum [55–57]. A. Mair *et al.* [11] have experimentally demonstrated that the angular momentum of the pump beam is transferred to the twin photons $\ell_p = \ell_s + \ell_i$. This fact will be crucial in the preparation of thermal states in OAM, as in the results presented in section 2.3 because change the beam diameter can change the temperature of the thermal distribution.

To understand how remote preparation of thermal states in OAM occurs in the context of SPDC, let us write its density operator using the equation 2.25:

$$\rho^{si} = |\Psi\rangle\langle\Psi|. \tag{2.40}$$

This density matrix represents the entangled state of the signal and idler photons. However, to perform remote preparation of thermal states in OAM, we need to use the signal beam to announce the presence of one of the photons in the pair. For this purpose, the detector is left entirely open, which does not discriminate any OAM values. By performing the OAM measurement in coincidence in the idler, we remotely obtain a thermal state. Mathematically, this operation is equivalent to performing the partial trace on the signal subsystem, leaving the idler information on the other arm of the experiment. By performing the partial trace, we obtain the reduced matrix of the idler beam:

$$\rho^i \equiv tr_S\left(\rho^{si}\right), \tag{2.41}$$

the partial trace is calculated as:

$$tr_S\left(\rho^{si}\right) \equiv \int d\boldsymbol{q_i} \int d\boldsymbol{q'_i} \left[\int d\boldsymbol{q_s} V^*(\boldsymbol{q_s} + \boldsymbol{q_i}) V(\boldsymbol{q_s} + \boldsymbol{q'_i})\right] |1, \boldsymbol{q_i}\rangle\langle 1, \boldsymbol{q'_i}|. \tag{2.42}$$

With equations 2.42 and 2.41 we get the reduced matrix of the idler beam. After the basis change to the Laguerre-Gaussian modes, the coefficients from equation 2.42 are related with the thermal probabilities from equation 2.57. We discuss the spectral distribution in SPDC , where this change of basis is performed.

2.1.3 Jarzynski Fluctuation Theorem

In thermodynamics, the extraction of work is one of the most crucial tasks, as it is applied to create thermal machines and devices that work with thermodynamic cycles. When we change the parameters infinitely slowly from a point A to B along a path γ, the total work we can perform on the system is equal to the Helmholtz free energy difference ΔF. However, when the parameters are changed in a finite rate along γ, the work is dependent on initial conditions, and in average, it will exceed ΔF:

$$\langle \mathcal{W} \rangle \geq \Delta F, \tag{2.43}$$

where $\Delta F = F - F_0$ is the variation of the free energy, which has the following definition:

$$F = U - TS, \tag{2.44}$$

with U being the internal energy, T the temperature, and S the entropy of the system.

The development of the thermodynamic theory occurred for macroscopic systems in thermal equilibrium. However, as technologies advance, systems become smaller in the limit where the fluctuations of the system start to become relevant, to the point that thermodynamic quantities, for example, work $\mathcal{W}$, can be treated as random variables. In this case, we can describe the variables by a probability distribution $P(\mathcal{W})$, from which one obtains the probability of extraction of a given amount of work $\mathcal{W}$ per cycle of the process.

As the variables become random, it is necessary to work with stochastic theories to account for fluctuations in these variables. In this context, the development of fluctuation relations allows us to obtain information from a system out of equilibrium. The basic assumptions of these fluctuation relations are that the system's initial state is thermal and the principle of micro-reversibility. The fluctuation relation we will use is the Jarzynski [14] relation:

$$\left\langle e^{-\beta \mathcal{W}} \right\rangle = e^{-\beta \Delta F}, \tag{2.45}$$

with $\beta = 1/k_b T$. Then we can write the left-hand side of the relation concerning its probabilities as:

$$\left\langle e^{-\beta \mathcal{W}} \right\rangle = \int d\mathcal{W} P(\mathcal{W}) e^{-\beta \mathcal{W}}. \tag{2.46}$$

The first development of this fluctuation relation was in the context of classical mechanics. However, several works extending it for the quantum systems are available [15, 49, 50].

Applying Jensen's inequality [58] to the equation 2.45, we recover the second law of thermodynamics for the average work $\langle \mathcal{W} \rangle$:

$$\langle \mathcal{W} \rangle \geq \Delta F. \tag{2.47}$$

In this case, individual violations of the equation 2.43 could occur, however equation 2.47 is always valid, due to the central limit theorem, fluctuations vanish as we approach the thermodynamic limit.

In the case of quantum systems it is necessary to perform the protocol of two projective measurements on energy eigenstates in the system to obtain the work in a process:

$$\mathcal{W} = \mathcal{E}_f - \mathcal{E}_i. \tag{2.48}$$

In our research group, the work of Araújo *et al.* [20] measured the work distribution in the two-measurement protocol using a photonic system. More details will be given in section 2.2.3.

2.2 THERMODYNAMICS EXPERIMENTS WITH OPTICAL SYSTEMS

This section introduces experiments with optical setups for quantum thermodynamics. Even though photons are non massive particles and do not interact directly with each other, they can be used as the thermodynamic fluid in some processes and they can be very useful for emulating other classical or quantum physical systems. Moreover, the experimental control over the degrees of freedom of light can be very high, in contrast with massive particles like ions and neutral atoms that require a greater experimental effort.

2.2.1 Single-qubit thermometry

In thermodynamics, the temperature is defined only for systems in equilibrium and in contact with a thermal bath. The usual method for measuring temperature without affecting the system and not changing its equilibrium is to use thermometers. However, as systems get smaller and smaller, thermometers need to adapt to the dimensions of the system. Otherwise, the external agent could modify the equilibrium conditions. In this line of work Jevtic *et al* [59] proposed a theoretical model using a single qubit to distinguish between two temperatures of a bosonic bath. Mancino *et al* [60] were the first to experimentally implement this type of system.

They implemented an experimental simulation of the interaction between a qubit and a thermal bath in a linear optical apparatus. In this case, the goal is to measure the thermal bath temperature, distinguishing between a "cold" (T_1) and a "hot" (T_2) temperature. When the qubit is isolated from the thermal bath, T_0 is the excited state, and T_1 is the ground state, and T_2 is the energy difference between both levels.

With a quantum channel, it is possible to simulate the presence of the qubit in the thermal bath implementing the excitation (decay) of the ground (excited) state. The quantum channel representing such an interaction is the generalized amplitude damping (GAD), described by two pairs of Kraus operators. The first pair is E_0 and E_1, are related to the qubit decay ($|0\rangle \rightarrow |1\rangle$) due to the "cold" bath (T_1). The second pair, E_2 and E_3, on the other hand, describe the situation when the qubit is excited to the $|0\rangle$ state due to the action of the "hot" bath (T_2), i.e., they describe the inverse process of E_0 and E_1 operators. Knowing the four Kraus operators, it is possible to reconstruct the system's density matrix and thus reconstruct the entire process.

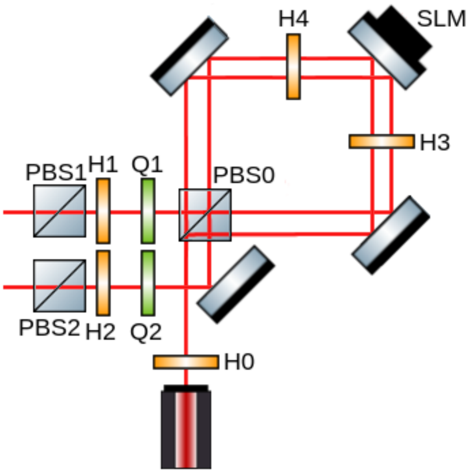

Figure 4 – Experimental setup for the implementation of GAD. The figure was taken from the reference [19].

The experimental setup is shown in figure 4. It consists of a Sagnac like interferometer [61], in which an SLM (spatial light modulator) replace one of the mirrors, to create holograms using phase modulation. In the interferometer the fundamental state $|1\rangle$ (excited $|0\rangle$) is represented by the vertical polarization state $|V\rangle$ (horizontal $|H\rangle$).

The preparation of the thermometer consists of three possible initial states (qubit): (i) the thermometer is on the ground state ($|V\rangle$) and the reservoir will heat it; (ii) the thermometer is on the excited state ($|H\rangle$) and the reservoir will cool it; (iii) the third state ($|+\rangle = (|V\rangle + |H\rangle)/\sqrt{2}$) is the superposition between the hot and cold states. The idea of the experiment is to send to the interferometer the three initial states and then analyze the polarization states at the output of the interferometer using process tomography. By the population difference in the outputs, it is possible to determine if the thermal bath was cold (T_1) or hot (T_2).

For short interaction times, the results obtained came very close to the theoretical predictions. It was possible to conclude that the three initial states are equally suitable for the task and the superposition state had no gain over the other two in this context. The conclusion was that polarization qubits could emulate thermometers in these thermal baths.

2.2.2 Photonic Maxwell's Demon

The so-called Maxwell's demon is a thought experiment proposed by James Clerk Maxwell to test the limits of the second law of thermodynamics. The experiment consists of a box with a division that separates it into two parts, initially containing a particle gas on the left side. Imagine that in this wall, we have a "Demon," an external agent that can obtain some information from the system, acts conditionally to this information. The information known to the demon is the energy of the particles. Imagine that it controls a door in this wall and opens the door for the hot particles to the right side, but blocks the cold particles (closing the door) to leave the hot particles on the right side of the box and the cold ones on the left side. Figure 5 shows the action of the demon performing this separation.

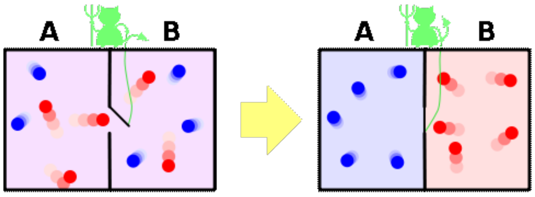

Figure 5 – Pictorial representation of Maxwell's demon. The picture was taken from the public repository "Wikimedia Commons". [62].

After separating all particles concerning their temperature, the demon reduces the system's entropy without performing any work, something that would violate the second law of thermodynamics. After various reinterpretations nowadays, the Maxwell's Demon is considered a system that obtains information with measurements, and with these results, it feeds the system by applying specific controls (feed-forward) to extract work.

Vidrighin's *et al.* [35] works use the information of the presence or not of a thermal beam to perform a proof of principle that it is possible to implement a photonic Maxwell's demon. Figure 6 shows the experimental setup, in which the beams splitters (BS) divide each of the two uncorrelated pseudo-thermal light beams into two paths. The BS's have high transmission, which means almost the whole beam is transmitted. The transmitted beam passes through the BS to be detected by a photodiode, and a photon counter detects the reflected (low reflectivity arm) beam.

The photodiodes convert light into electric current and in the setup they are inversely polarized between each other and connected to a capacitor. On average, the capacitor's charge will always be zero as we have approximately the same number of photons arriving at each photodiode. However, thermal light has a bunching effect, and since the reflection probability of a photon by BS is low, when a photon arrives at one of the detectors, we can conclude that there is a high probability that there are other photons at the transmission port towards the photodiode. The goal is to use the detection's information to switch the polarization of the capacitor to take advantage of all the current generated by the photodiodes and thus charge it efficiently and then use the energy to perforn another task.

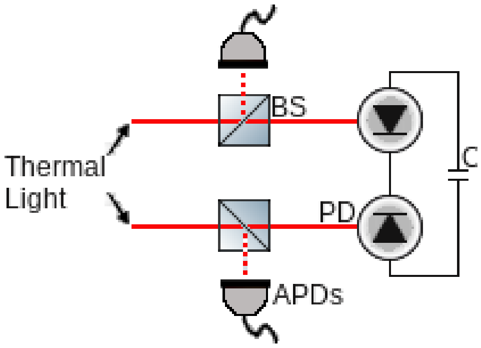

Figure 6 – Experimental setup for the proof of principle of a photonic Maxwell's Demon by Vidrighin *et al.*.

The authors measured only the difference in the photodiodes intensities conditioned to the information of the detection events in each detector at Demon's arm. As the feed-forward itself was not applied, this experiment is proof of principle that this photonic Maxwell's Demon is feasible. However, in chapter 4 we are going to present our results where we implement a photonic Maxwell's Demon with active feed-forward. We also study how quantum correlations may affect the Demon's efficiency in comparison with classical thermal baths.

2.2.3 Work Distribution for Optical Vortices Using the Two-Measurement Protocol

Section 2.1.3 briefly discusses some experimental realizations that can measure the work and reconstruct the work distribution of quantum systems. Among these mentioned realizations, the one of most interesting is the experiment performed by Araújo *et al.* [20]. In this section, we will discuss this work in more detail.

For the work calculation according to the equation 2.48, it is necessary to perform two projective measurements in energy eigenstates, a prerequisite for using Jarzynski's fluctuation-dissipation relation 2.45 in the quantum regime. However, in this system, it is not possible to perform these measurements directly. A workaround for this problem is the analogy between the paraxial Helmholtz equation (eq. 2.7) and the Schrödinger equation in two dimensions, considering a quantum harmonic oscillator [18]. In this analogy, we can realize the following relationships:

$$\begin{aligned} \psi(x,y,t) &\rightarrow A(x,y,z) \\ t &\rightarrow z. \end{aligned} \tag{2.49}$$

The 2D wave function ($\psi(x,y,t)$) propagates in time, whereas the solutions of the paraxial Helmholtz equation (eq. 2.7) propagate as an $A(x,y,z)$ envelope along the z axis. The paraxial wave equation with the index of refraction is:

$$\frac{i}{k}\frac{\partial A(x,y,z)}{\partial z} = \left(-\frac{1}{k^2}\nabla_\perp^2 + n(x,y)\right) A(x,y,z). \tag{2.50}$$

To hold the analogy we need to include the potential in the 2D Schröedinger's equation:

$$i\hbar\frac{\partial\psi(x,y,t)}{\partial t} = \left(-\hbar^2\nabla_\perp^2 + V(x,y)\right)\psi(x,y,t). \tag{2.51}$$

Comparing equations 2.50 and 2.51 in the analogy we can relate the index of refraction $n(x,y)$ and the potential $V(x,y)$. Considering the 2D quantum harmonic oscillator that has the following potential:

$$V(x,y) = \frac{m}{2}\omega^2(x^2+y^2), \tag{2.52}$$

where m is the mass of the oscillator and ω is the frequency of oscillation. Under the proper conditions for the index of refraction, the $LG_{p\ell}$ modes can emulate the 2D quantum harmonic oscillator. Their eigenvalues are:

$$\epsilon_{\ell p} = (|\ell| + 2p + 1)\hbar\omega. \tag{2.53}$$

If we consider only the family of modes with $p = 0$, the eigenvalues become:

$$\epsilon_\ell = (|\ell| + 1)\hbar\omega. \tag{2.54}$$

The eigenenergy for the 2D quantum harmonic oscillator and LG modes have the same form. Since LG modes have angular momentum, when we measure its ℓ is equivalent to measure the energy for the same energetic level (ϵ_ℓ) at the harmonic oscillator. If we restrict ourselves to processes that change only the angular momentum of the beam, we obtain the following work:

$$\mathcal{W}_{\ell\ell'} = (|\ell'| - |\ell|)\hbar\omega, \tag{2.55}$$

where ℓ is the initial and ℓ' the final state.

With this definition, we can calculate the probability distribution:

$$P(\mathcal{W}) = \sum_{\ell\ell'}\delta(\mathcal{W} - \mathcal{W}_{\ell\ell'})p_{\ell\ell'}. \tag{2.56}$$

where $p_{\ell\ell'} = p_\ell p_{\ell'|\ell}$ is the probability of observing the transition $\ell \to \ell'$, $p_{\ell'|\ell}$ is the probability of observing ℓ' given that the initial state was ℓ and p_ℓ are the thermal probabilities according to:

$$p_\ell = e^{-\beta(|\ell|+1)\hbar\omega}e^{\beta\hbar\omega}\tanh\frac{\beta\hbar\omega}{2}. \tag{2.57}$$

The LG modes accept negative values for ℓ , but the harmonic oscillator does not. However, it is possible to avoid this problem, as the probabilities and the eigenvalues depend only on the ℓ modulus, then the eigenenergies have the same value. The degeneracy of the system, except for $\ell = 0$, was taken into account to obtain the thermal probabilities.

The setup for performing the study of the two-measurement protocol is according to figure 7. The SLM1 creates a phase hologram that imprints the desired OAM to the laser beam. As we prepare the initial ℓ, the eigenenergy is known. It can be considered as the first measurement of the protocol.

At SLM2, a new phase hologram is generated to introduces transitions between energy levels to perform work on the system. A device called "mode-sorter" [63] performs the second measurement of the protocol. The mode-sorter performs the spatial separation of modes by ℓ, i.e., each region of the image can be associated with a specific value of OAM. A CCD camera records the image that by the peaks position can give us information of which components of OAM are present.

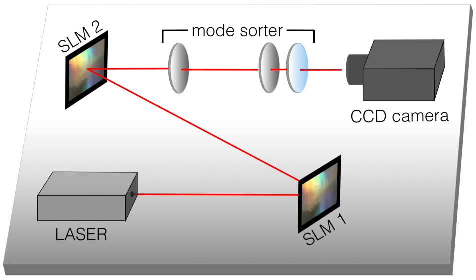

Figure 7 – At this experimental setup, the SLM1 prepares the state with a desired ℓ, being the first measurement. The SLM2 introduces the transitions between the eigenenergies ($\ell \rightarrow \ell'$). The mode-sorter and the camera perform the final measurement, allowing us to calculated the work. The figure is from reference [19].

With the first (state preparation) and the second (mode-sorter) OAM measurements, it is possible to reconstruct the work distribution using an optical system. In this same work, they implement an experiment like a photonic Maxwell's Demon, in which the "available" information was about the sign (negative or positive) of OAM, then performing conditional operations on ℓ being positive or negative.

2.3 REMOTE STATE PREPARATION OF THERMAL STATES IN ORBITAL ANGULAR MOMENTUM WITH ENTANGLED PHOTONS

This section is divided into two main parts. The first is concerned with the spectral distribution in the SPDC (sec. 2.3.1), which will be of utmost importance for the interpretation of the thermal state distributions in OAM presented in the results section (sec. 2.3.2). In the results section, we introduce the concept of remote state preparation of thermal states in OAM. In the following subsections results regarding atmospheric turbulence (sec. 2.3.2.0.1), Fresnel lens (sec. 2.3.2.0.2) and variation of the detector aperture in the signal beam (sec. 2.3.2.0.3) are presented.

2.3.1 Spectral Distribution in Spontaneous Parametric Down-Conversion

In the 2.1.2 section, we discussed some properties of parametric down-conversion in the transverse spatial degrees of freedom, such as conservation of OAM [11]. Because of the entanglement in these degrees of freedom, J. P. Torres *et al.* [48], analyzed the states of twin photons concerning $LG_{p\ell}$ modes and obtained the quantum spiral bandwidth.

They start the analysis, with a wave function for the parametric down-conversion similar to the one in equation 2.19:

$$|\psi\rangle = \int d\boldsymbol{q_s} \int d\boldsymbol{q_i} \Phi(q_s, q_i) a_s^\dagger(q_s) a_i^\dagger(q_i) |0, 0\rangle . \tag{2.58}$$

The decomposition of the quantum state $|\psi\rangle$ on the basis of the eigenstates of the orbital angular momentum operator, the $LG_{p\ell}$ modes, was performed according to:

$$|\psi\rangle = \sum_{\ell_s p_s} \sum_{\ell_i p_i} C_{p_s,p_s}^{\ell_i,\ell_s} |\ell_s, p_s; \ell_i, p_i\rangle \tag{2.59}$$

and the coeficients of the expansion $C_{p_s,p_s}^{\ell_i,\ell_s}$ are:

$$C_{p_s,p_s}^{\ell_i,\ell_s} = \int d\boldsymbol{q_s} \int d\boldsymbol{q_i} \Phi(q_s, q_i) \left[LG_{p_s\ell_s}(q_s)\right]^* \left[LG_{p_i\ell_i}(q_i)\right]^* . \tag{2.60}$$

With these coefficients we determine the weights $P_{p_s,p_i}^{\ell_s,\ell_i} = \left|C_{p_s,p_i}^{\ell_s,\ell_i}\right|^2$ of the superposition of the $LG_{p\ell}$ modes in the wave function $|\psi\rangle$, which give us the joint detection probabilities of one photon of the signal mode (ℓ_s, p_s) and another photon of the idler mode (ℓ_i, p_i). Figure 8 shows the calculated probabilities for the case where the pump beam is Gaussian, hence $\ell_s + \ell_i = 0$ [48]. They used three configurations for the pump beam diameter in their calculations. By analyzing these results, it is possible to observe that the larger the diameter of the pump beam, the wider the spiral spectral distribution becomes. A critical aspect of our application is that the decay of the coefficients follows an exponential decay. This result is important in the preparation of the thermal state.

We will associate these exponential distributions to single-photon thermal states for the OAM degree of freedom. For this, we can rely on the natural form of the OAM distribution for photon pairs.

2.3.2 Experimental results for the remote state preparation of thermal states

There are several possible strategies for thermal state preparation in optical systems, depending on the degree of freedom of interest. The references [35, 64] implemented pseudo-thermal states from a laser with the technique know as Arecchi wheel [65–67]. The beam is incident on a ground glass disk that rotates at a certain speed. The propagation of light through the spinning disk produces a speckle pattern,

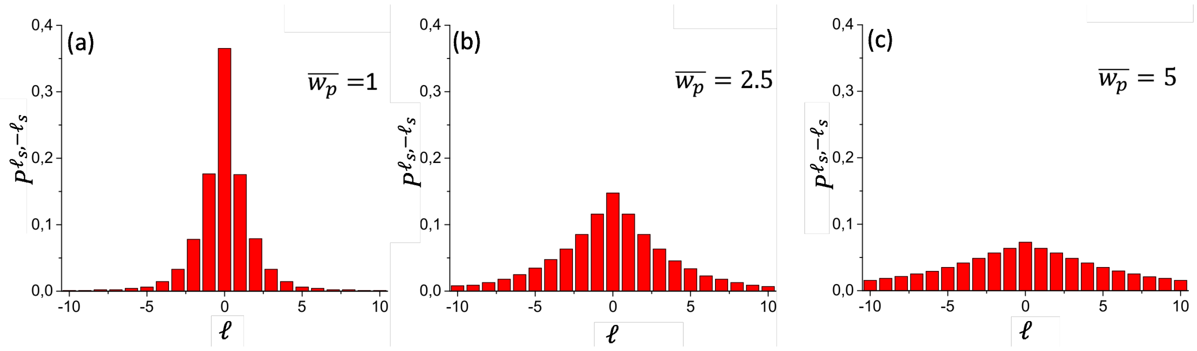

Figure 8 – Figures **(a)**, **(b)** and **(c)** show the theoretical probabilities [48] $P_{0.0}^{\ell_s,-\ell_i}$ when the pump beam is Gaussian, hence $\ell_s + \ell_i = 0$. Thus the weights are $P^{\ell_s,-\ell_s}$. Probability distributions were obtained for different values of $\overline{w_p} = w_p/\sqrt{\lambda L}$, where w_p and λ are the width and wavelength of the pump beam and L is the crystal thickness.

where the light collected within this pattern has a photon statistic similar to that of a natural thermal source, where its second-order correlation $g^2(\tau) \to 2$. However, it is a mono frequency beam opposite the usual thermal light with a wide frequency range. The advantage of employing a pseudo-thermal source from a laser is that the intensity is much higher.

In our work, we wish to prepare thermal states involving the OAM. For this purpose, we use the setup presented in figure 9, in which a laser of λ = 405 nm is incident on a nonlinear crystal (BBO - type I) and generates two beams with λ = 810 nm, the signal and idler. The signal passes through a lens with a focal length equal to 25 *mm* and is detected by an SPCM (single-photon counting module). On the other hand, the idler beam passes through a similar lens and goes through an SLM, then coupled to a single-mode optical fiber detected by the second SPCM. Each SPCM generates an electronic pulse for every detected photon. The electronic circuit implemented by an FPGA (Field Programmable Gate Array) receives the pulses to checks the time interval between the arrival of the pulses in the signal and idler beam detectors. When they arrive inside the window of 5*ns*, it is a coincidence count, i.e., meaning they are twin photons. The single-mode fiber, present in the path of the idler beam, couples only modes with no orbital angular momentum, which means just $LG_{0,0}$. So it is used in conjunction with the SLM to perform the measurements of the orbital angular momentum values.

For our measurements, we use the fact that the single-mode optical fiber can couple only Gaussian modes ($LG_{0,0}$), by doing that, we use the SLM to increase or decrease the OAM by an arbitrary value by applying the desired hologram of phase. For example, if the photon generated by the crystal has angular momentum $\ell = 2$, we need to generate a mask on the SLM that applies $\ell = -2$ (a mask that reduces the OAM of the incident beam by two units), reducing its OAM to zero, and then it can be coupled

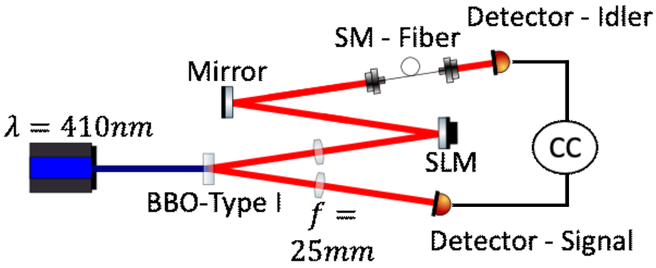

Figure 9 – The experimental setup used for the remote state preparation of thermal states. We detect the signal beam with the detector completely open, which means we do not discriminate any value of OAM. It is equivalent to perform the partial trace at the system, making the idler a thermal distribution naturally. To confirm it, we use an SLM to scan the OAM distribution applying the $-\ell$ operation to make the total $\ell = 0$ and then couples it into a single-mode optical fiber to be detected in coincidences.

into the fiber, allowing detection in coincidences. In order to measure the whole thermal distribution, we scan ℓ from -10 to 10, recording the coincidence counts for every "$-\ell$" applied. The SLM can also be used to apply quantum processes such as turbulence or a Fresnel lens. Both types of masks have been applied to thermal states to study the effects of these processes.

To produce the thermal state remotely, we used the entanglement of the twin photons produced by the SPDC relative to the OAM. Detecting the signal photon, with it utterly open before any process or measurement on the idler beam, is equivalent to performing the partial trace on this subsystem. When measuring the idler at OAM basis in coincidences with the signal, we obtained a thermal distribution according to figure 10.

The thermal distribution calculated in the reference [48], figure 8 has perfect symmetry concerning the values of ℓ, which we expect since the probabilities of the thermal distribution (eq. 2.57) depend only on the modulus of ℓ. However, the result obtained in our measurements is not 100% symmetric, having small variations in the rate of coincidences for measurements of the same $|\ell|$. This variation is due to experimental errors in the measurement process, mainly the center of the hologram's for orbital angular momentum raising or decreasing.

As we want to check if our distributions are thermal, we fitted the experimental data with a tentative function given by:

$$p_\ell = ne^{-b(x+1)}, \tag{2.61}$$

where $x = |\ell|$. Comparing with equation 2.57 leads to the following identifications:

$$\begin{aligned} n =& e^{\beta\hbar\omega} \tanh \frac{\beta\hbar\omega}{2} \\ b =& \beta\hbar\omega. \end{aligned} \tag{2.62}$$

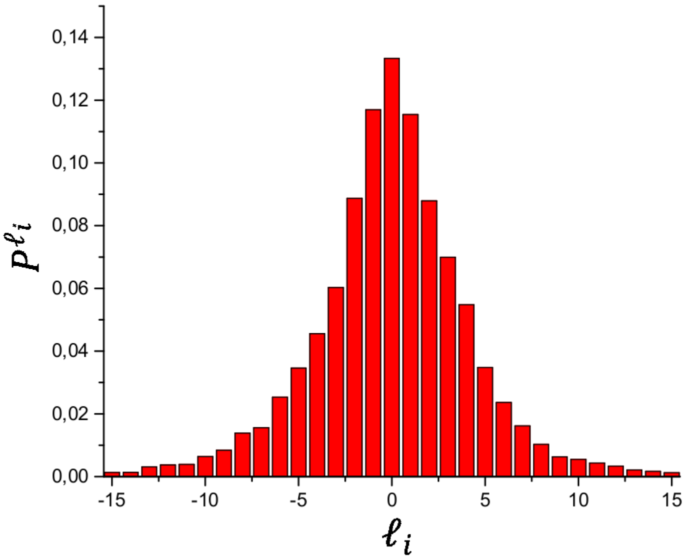

Figure 10 – Thermal distribution measured according to the experimental setup in figure 9. We perform the measurements using an SLM and single-mode optical fiber in coincidences where we record the coincidence rates to reconstruct the experimental probabilities P^{ℓ_i}.

From parameter b we can find an effective temperature for our system:

$$T = \frac{\hbar\omega}{k_b b}. \tag{2.63}$$

In the context of thermal distribution, the higher the temperature, the wider the distribution becomes, as the higher energy levels (or those with larger ℓ) become more populated. In this case, according to the equation 2.63, the smaller the b parameter of the fit, the higher the system's temperature.

The weights on the expansion in equation 2.60 [48], depends on the crystal length and the pump beam width w_p. The square modulus of the coefficients is directly related to equation 2.61, from which we can calculate the parameters of the distribution.

We also analyze the average energy of each distribution according to:

$$\langle E \rangle = \sum_{\ell} p(\ell)\epsilon_{\ell}, \tag{2.64}$$

with $p(\ell)$ being the thermal probabilities and $\epsilon(\ell)$ being the energy of the ℓ-th energy level.

The results obtained will be separated into three subsections, production of thermal states and consequent application of the following processes: (i) turbulence, (ii) Fresnel lens, and (iii) variation of the detector aperture of the signal beam. We obtain all results according to the setup of the figure 9. However, in each subsection, it will be explained what differentiates each type of measurement performed. The error bars where omitted in all experimental plots as the statistics is the Poissonian and the errors bars are the standard deviation of the coincidence counting rate, ie, the square root.

2.3.2.0.1 Turbulence

Using orbital angular momentum to encode information has advantages and disadvantages over polarization qubits. The most significant advantage is that the orbital angular momentum has infinite possible ℓ values, allowing coding information more efficiently. However, several studies have shown that atmospheric turbulence degrades the transversal modes, consequently degrading the information coded in these modes [68–70]. H. Ibrahim *et al.* [70] already showed the degradation of the wavefront with orbital angular momentum under turbulent processes. However, the aspects of how a thermal distribution behaves under these conditions are still an open subject. So, let us then analyze the effect of turbulence on the thermal states of OAM from a thermodynamic point of view.

Our goal here is to check how turbulence would alter the thermal distribution and consequently the average energy of the system. Consider the experimental apparatus in figure 9. We know that the detection of a signal photon performs the remote preparation of a thermal state in the idler beam. To evaluate the effect of the propagation of the idler through a turbulent medium, we can apply a phase mask before the SLM used in the OAM measurement method. Several recipes show how to create a phase mask that reproduces Komolgorov turbulence with controlled Fried parameter [71–73]. Furthermore, B. Rodenburg *et. al* [69] have shown that the turbulence mask can be applied in superposition with the OAM masks for lifting and lowering it is ℓ with the same SLM. In this way, we can perform two tasks in the same SLM. The turbulence used initially had no noticeable effect on the distribution. This effect is likely a consequence of the large difference between the length scales of the modulation and the beam size, leaving the final hologram (turbulence + orbital angular momentum) almost intact. To increase the effectiveness of the Turbulence, we modulate a phase mask where we repeat the previous one in a grid where each mask had 1% of the original size. Figure 11 **(a)** shows a measured distribution without the turbulence mask applied. Figure 11 **(b)** shows the resulting distribution when the turbulence mask is applied. From the data, we then calculate the average energy for the initial thermal state $\langle E\rangle = 3.89\hbar\nu$, and for the state after applying the turbulent process $\langle E\rangle = 3.93\hbar\nu$.

For this modulation, we have not yet obtained any significant effects. We attribute this to the fact that the mask has a small modulation relative to the beam diameter. We then made new measurements by changing the size of the turbulence mask to 5% of the original size instead of the 1% used in the previous measurements.

We show the measurements with the second turbulence mask in figure 12 **(b)**. The distribution obtained after turbulence still has a shape very close to an exponential.

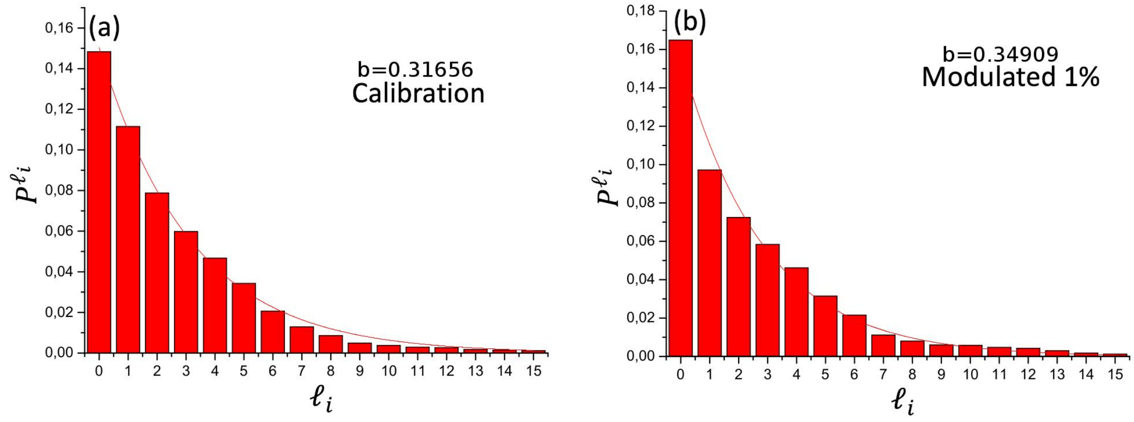

Figure 11 – Measurements of thermal distributions where **(a)** have no turbulence, as we wish to calibrate the system. Figure **(b)** is with turbulence, where the mask is composed of a grid where each element is a copy with 1% of the original size.

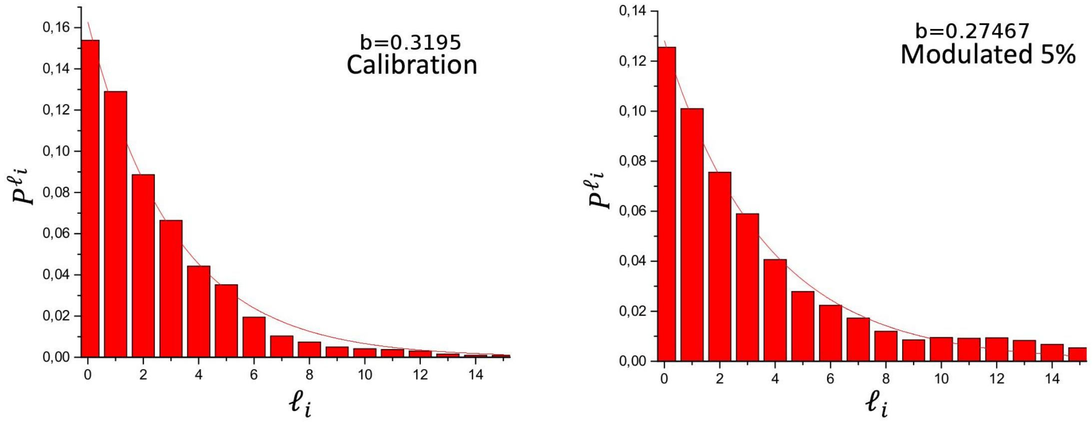

Figure 12 – Measurements of thermal distributions where **(a)** have no turbulence, as we wish to calibrate the system. Figure **(b)** is with turbulence, where the mask is composed of a grid where each element is a copy with 5% of the original size.

However, we can see that the modes with higher OAM have become slightly more populated. Assuming that it is still possible to fit the distribution as a thermal distribution, we can compare the values of b. In the absence of turbulence $b = 0.33195$ and with turbulence $b = 0.27467$. In this case, we can relate this b variation to a temperature increase in the distribution. The mean energy also had an appreciable change, as the calibration curve had $\langle E \rangle = 3.66\hbar\nu$ and the distribution after turbulence had it is mean energy increased to $\langle E \rangle = 4.79\hbar\nu$. The increase in temperature and mean energy by the turbulent process is consistent with the expectation that this type of process increases the system's disorder.

2.3.2.0.2 Fresnel Lens

Our OAM measurement procedure includes the coupling of a light beam to a single-mode optical fiber that couples only Gaussian modes, whose waist, i.e., the family of modes, is determined by the optical elements that we choose for the task. Here, we employ a commercial system with a factory pre-aligned aspherical lens in our setup, which couples Gaussian modes with a waist of about 2mm. We plan the whole setup to fit these requirements.

In this measurement scheme, if we change the characteristics of the incident OAM modes, we will measure the coverage of each mode of the incident family with the modes defined by the measurement system, i.e., we will measure one element of the decomposition of the new family of modes. For this reason, we tested another process, implementing lens at the system, as it will changes the structure of the modes and can be seen as a squeezing [19] type operation.

We applied Fresnel lenses through the same SLM that we implement the OAM measurement scheme to the turbulence process, avoiding the need for complicated realignments of the system every time we change the lens, as it would be for a physical optical element. We used focal lengths of 1 and 1.5 *m*. We chose these values as the distance between the SLM, and the fiber coupler is approximate $\approx 1.27m$. Thus, we have one situation where the focal length is smaller (1 *m*) and another where it is larger (1.5 *m*) than the distance between the SLM and the coupler.

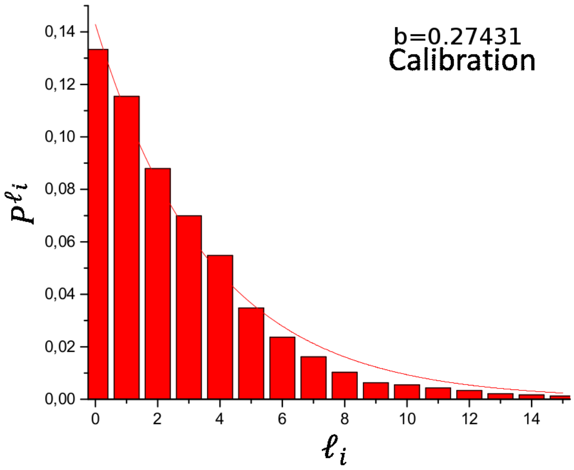

Figure 13 – The results for the calibration curve before the Fresnel Lens measurements.

The calibration curve (with no process) is shown in figure 13. The fit parameter b of the thermal distribution without process ($b_{term} \simeq 0.27$) is smaller than the values obtained with the Fresnel lens of $1m$ ($b_1 \simeq 0.49$) and $1.5m$ ($b_{1.5} \simeq 0.39$). Since the distributions obtained by applying the process are still in the form of thermal distribution,

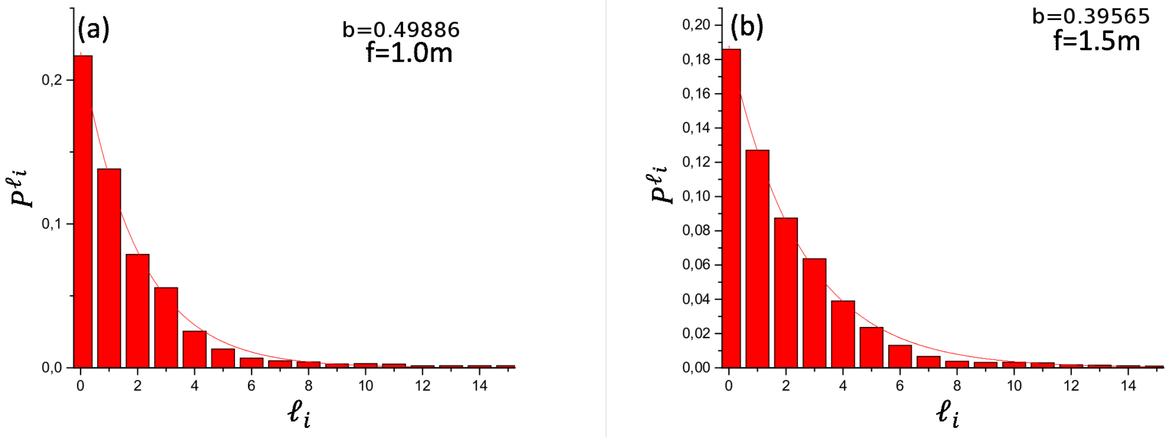

Figure 14 – Measurements for the process using Fresnel lenses. Figure **(a)** represents the situation where the focus is smaller ($1m$) than the distance between the SLM and the fiber coupler. Figure **(b)** represents the situation where the focus is larger ($1.5m$) comparing this distance. The measurements were performed according to the setup in figure 9.

a possible interpretation would be cooling. Corroborating this interpretation is the fact that the average energies also decrease:

- $\langle E_{termo} \rangle = 4.21\hbar\nu$
- $\langle E_1 \rangle = 3.22\hbar\nu$
- $\langle E_{1.5} \rangle = 3.52\hbar\nu$.

Observing the results, we can conclude that this implementation will reduce the temperature of the distributions. However, even being a simple way of implementation, its utility and control are not helpful. A more effective manner of controlling it would be changing the beam waist of the pump, even if the realignment of the whole system is complicated. Despite if the objective of change the temperature of beam distribution is not accomplished, we can still interpret the meaning of changing the family of modes in terms of thermodynamics. Using the analogy of paraxial wave equation and the Schrödinger's equation, as described in section 2.2.3, this change of family of modes can be related to a change of the potential of 2D harmonic oscillator [19].

2.3.2.0.3 Variation of the detector aperture in the signal beam

In the measurements performed so far, the signal beam detector remained completely open. It was used only to announce the presence of a photon in the idler beam. Leaving the detector completely open in this case is equivalent to performing the trace over all the orbital angular momentum states of this subsystem. However, if we close it, we start to select which values of OAM can pass through the aperture, meaning that we perform the partial trace over it.

The goal of the measurements described in this section is to verify if we can use the detector aperture as a parameter to control the idler photon's state. Figure 15 shows the results of measurements of the OAM distribution in the idler beam when the signal detector is fully open (calibration) **(a)**, with 0.58*mm* **(b)**, 1*mm* **(c)** and 1.5*mm* **(d)** apertures.

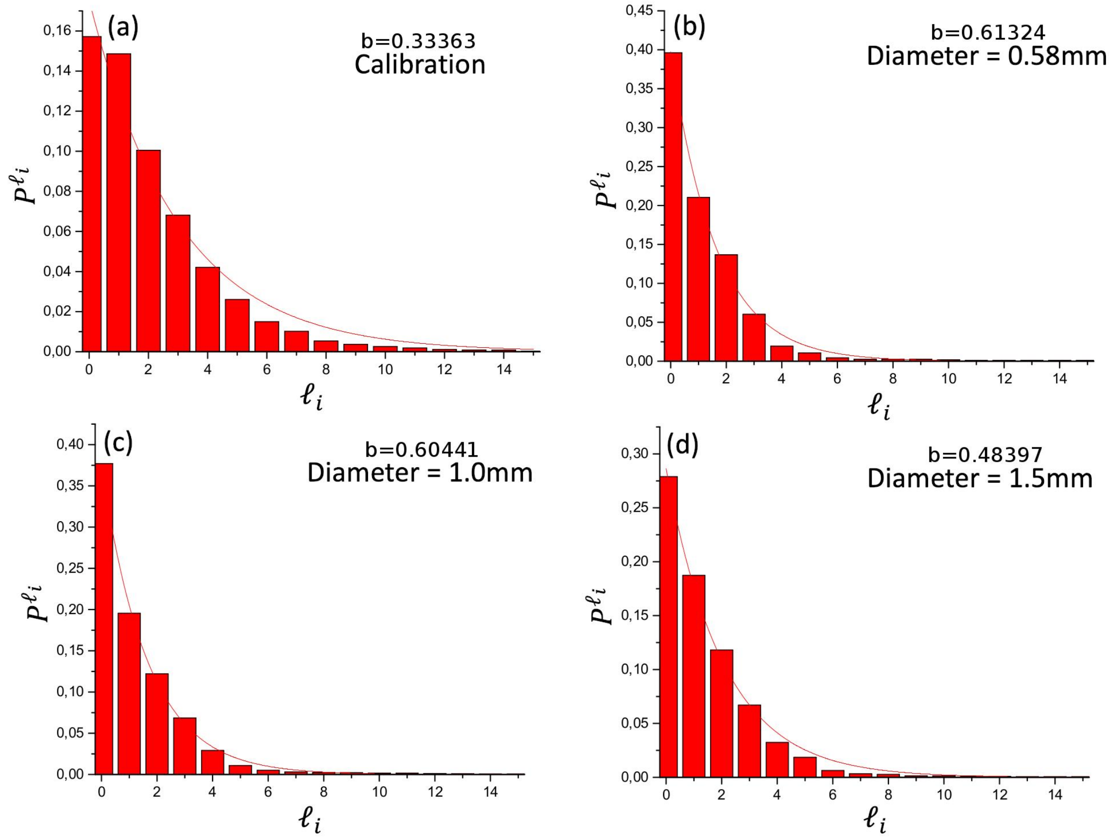

Figure 15 – Figure **(a)** represent the calibration measurement. Figures **(b)** to **(d)** are the situations where we vary the detectors aperture, where **(b)** is 0.58*mm*, **(c)** is 1*mm* and **(d)** is 1.5*mm*.

	Calibration	0.58 *mm*	1 *mm*	1.5 *mm*
b	0,333 ± 0,026	0,613 ± 0,021	0,604 ± 0,015	0,484 ± 0,017

Table 1 – Evolution of the curve fitting parameter according to the detector opening in the signal beam. It is possible to observe that as the aperture decrease, we select just smaller values of OAM, cooling the distributions, as the temperature is the inverse of *b*.

The results indicate that the distributions still follow an exponential decay law and indicate that we can still interpret them as thermal distributions. By analyzing *b* at 1, we can see that, as we decrease the aperture size, *b* grows, meaning that the temperature of each distribution tends to decrease. This behavior is in line with the expectation that a smaller diameter aperture will exclude modes with larger OAM.

We are now performing a partial trace of the signal by selecting some modes according to their sizes. The distributions are still thermal, making this method an exciting choice to decrease the temperature and, consequently, the average energy's distribution for the desired applications.

2.4 CONCLUSIONS

This work demonstrates that it is possible to implement remote preparation of thermal states in OAM using the quantum spiral bandwidth that comes naturally from spontaneous parametric down-conversion. We show how to control the distribution's temperature by changing the beam diameter and the detector's aperture at the signal beam. We demonstrate that a Fresnel lens at the SLM is not a suitable tool for temperature control even with its easy application. We studied how turbulence affects the thermal distribution, making it a hotter distribution.

The remote preparation of a thermal state is relevant as it aids in preparing systems that can study quantum thermodynamics out of equilibrium using Jarzynski fluctuation relations (eq. 2.45), as they require the initial state of the system to be thermal. As parametric down-conversion allows creating these distributions in the single-photon regime, it can be applied in a range of applications in photonic systems. Since they are relatively well-controlled and their manipulation is not as complicated as other systems, such as neutrons, atoms, and ions, they require complicated apparatus to trap and control them.

This field is being a vital line of research at GIQSUL (Grupo de informação quântica do Sul do Brasil - Southern Quantum Information Group), where in the last years Araújo *et al.* published the Work Distribution for Optical Vortices Using the Two-Measurement Protocol [20] (which was described in section 2.2.3), a review of quantum thermodynamics with linear optics by G. L. Zanin *et al.* [19] and, an experimental study of the generalized Jarzynski fluctuation relation using entangled photons by P.H. Souto Ribeiro *et al.* [21].

3 FIBER-BASED PHOTONIC FEED-FORWARD

In the 2000s, Knill, Laflamme, and Milburn (KLM) [74, 75] showed that it is possible to implement quantum computation with linear optics, nowadays know as Linear optical quantum computing (LOQC), by using only beam splitters, phase shifters, single-photon sources and photo-detectors, optical elements that are widely available for more straightforward implementation. This proposal eliminated the need for non-linear coupling between photons. However, for a universal quantum computing protocol, it needs to be able to perform all quantum gates, and the CNOT gate in this proposal is non-deterministic, having a probability of success of 1/16 [76]. An alternative proposal is the 'one-way' [77–79] or 'measurement-based' quantum computation (MBQC) [80], where this scheme uses entangled states to create the "cluster-states" [81, 82], in which allows the implementation of any unitary quantum logic operation.The interest and applications of LOQC by the community is significant as it can be implemented in an extensive range of applications as quantum network [83], quantum teleportation [36, 84, 85], remote state preparation [86], quantum error correction [87], improving photon sources [88, 89], quantum metrology [90], quantum data compression [91], experiments that require an outcome of an earlier measurement to apply conditioned a quantum operation [92–94].

The usual approach for MBQC and feed-forward is by the use of Pockels cells [36–39], which are devices that act as waveplates that you can control it by applying the appropriate electric field, i.e., voltage. However, the calibration is quite complicated, and usually, it requires high voltages (kV) to operate, besides the fact that we need three Pockels cells to transform an initial state in polarization to any other desired one inside the Bloch sphere, making the calibration and control even more complicated.

In order to solve this problem, we developed a method using ultrafast optical (electro-optic) switches (UFOS) in a fiber-based proposal that applies to the existing telecom network. The UFOS are wave-guide components with two inputs/outputs in optical fibers conditioned on a triggering signal, can switch between parallel and crossed input/output paths, allowing us to route the photons in a multi-path setup for implementing different unitary operations using standard and stable optics as waveplates. It allows us, for example, to implement a linear cluster where the state will be prepared conditioned to the heralded signal.

To characterize our fiber-based feed-forward technique, we choose the remote state preparation of a single-photon using polarization as a degree of freedom. We perform the remote state preparation using a maximally entangled state in polarization, i.e., a Bell state, as the initial state, and the idler is projected onto a given polarization state. This projection prepares the state of the signal remotely. However, we are on a two-dimensional basis, meaning that we have two possibilities of projection, the desired one and an orthogonal one, consequently the same two options for the remote state. As a result, the remote state preparation is a probabilistic process leading to fidelities of 50% concerning the target state. Furthermore, we route the wrong photons to be corrected with our method, allowing us to arrive at fidelities higher than 90% when we do not correct the imperfections of the entangled state generation, i.e., when we compare with the theoretical Bell state. When we calculate the fidelities using the two-photon state that we generate experimentally, we obtain an average of $(99 \pm 1)\%$ of fidelities.

In this chapter in section 3.1, we describe the theory behind the Bell states generation, the theory of remote state preparation, a complete description of the real and complex families of states, and the relative unitary transformation used in the correction procedure, the theoretical and experimental method for partial projection of the two-photon state, and a description of the UFOS as they are the core of the technique. In section 3.2 we present the experimental results. In section 3.3 we present the conclusions of our work. All the results that we present here are published in G. Zanin *et. al* [95].

3.1 FUNDAMENTAL CONCEPTS

This section discuss some fundamental aspects of SPDC using polarization as a degree of freedom. We discuss the theory between our feed-forward protocol, the theoretical description of every family of states, and it is relative unitary operation for state correction. We describe the methodology that we use to project our theoretical and experimental states to calculate the fidelities to certify the quality of the states we produce.

3.1.1 Spontaneous Parametric Down Conversion using polarization as Degree of Freedom

In Chapter 2, we describe the SPDC focusing on the transverse degrees of freedom. However, now we choose polarization as the degree of freedom and develop the theory of SPDC for the maximally entangled states, know as a Bell states. In our development of the theory, we follow the same procedure as [96].

To our description, we will assume that the pump field is quantized and we are at the nondegenerate case. In this regime, we can write the interaction Hamiltonian ($\hat{H}_I$) of our system:

$$\hat{H}_I \approx \chi^2 \hat{a}_p \hat{a}_s^\dagger \hat{a}_i^\dagger + h.c., \tag{3.1}$$

where χ^2 is the second-order nonlinear susceptibility, $\hat{a}_p$ is the annihilator operator for the pump and $\hat{a}_s^\dagger$ ($\hat{a}_i^\dagger$) is the creator operator for the signal (idler) and the *h.c.* is the hermitian conjugate. We will focus on the case when the signal and idler are initially at a vacuum state $|0\rangle$. In this situation, the signal and idler photons are created when the pump annihilates a photon:

$$|1\rangle_p |0\rangle_s |0\rangle_i \to \hat{a}_p \hat{a}_s^\dagger \hat{a}_i^\dagger |1\rangle_p |0\rangle_s |0\rangle_i = |0\rangle_p |1\rangle_s |1\rangle_i . \tag{3.2}$$

This process is spontaneous and the signal and idler photons are created at the same time, this is why they are commonly know as twin-photons.

Because of the energy conservation we have:

$$\omega_p = \omega_s + \omega_i \tag{3.3}$$

and the momentum conservation:

$$\boldsymbol{k}_p = \boldsymbol{k}_s + \boldsymbol{k}_i. \tag{3.4}$$

These equations are known as "phase matching" conditions, and they occur inside nonlinear media where the non-linear coefficient χ^2 is big enough to not be negligible, like the BBO (Barium Borate) crystal. There exist three types of crystal: (i) type-0, where the pair have the same polarization as the pump, (ii) type-I, where the pair have orthogonal polarization concerning the pump and (iii) type-II, the pair have orthogonal polarization between each other. Here in our description, we work with a type-2 crystal.

The BBO crystal is a birefringent media, which means that the refractive index depends on the polarization of the light. The usual nomenclature for these refractive indexes is the ordinary (o) and the extraordinary (e). For type-II, every refractive index produces a different cone of light. Figure 16 **(a)** shows a diagram that represent this emission. In this case, each cone is related to one polarization, i.e., horizontal and vertical ones.

If we choose to filter the intersection region, as represented by the small circles at the intersections in Figure 16 **(b)**, we are at one regime where we have no knowledge from which cone the photon came from, it prevents us from having previous knowledge about the polarization of each photon. It is a crucial part of the alignment as our goal is to obtain a Bell state. Otherwise, we would be in a situation where we have an entangled pair of photons where the signal and idler have fixed polarization. At the intersection point, the interaction Hamiltonian ($\hat{H}_I$) becomes:

$$\hat{H}_I = \hbar\eta \left(\hat{a}_{Vs}^\dagger \hat{a}_{Hi}^\dagger + \hat{a}_{Hs}^\dagger \hat{a}_{Vi}^\dagger \right) + h.c., \tag{3.5}$$

where $\hat{a}_{Xy}^\dagger$ is the creator operator for the X (horizontal/vertical) polarization and for the y (signal/idler) beam. In this Hamiltonian, we implement the parametric approximation. It consists of a situation where the SPDC process has a low probability, so we can consider the pump beam classical, and the fact that it is depletion can be ignored. In the parametric approximation, we take $\eta \propto \chi^2 \epsilon_p$, where ϵ_p is the classical coherent field of the pump.

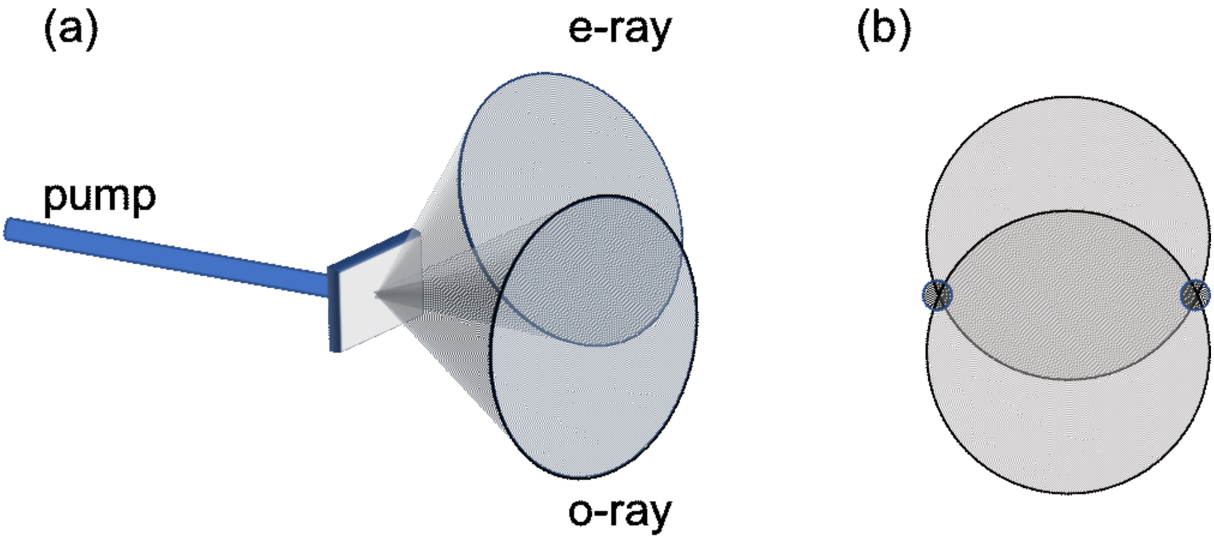

Figure 16 – Figure **(a)** represent the cones of light emitted by a type-II crystal. Figure **(b)** is a perpendicular representation of the cone where the signal and idler photons are chosen to be at the intersection.

As mentioned before, we focus our attention on the situation where the signal and idler initial state is the vacuum:

$$|\Psi_0\rangle = |0\rangle_{Vs}|0\rangle_{Hs}|0\rangle_{Vi}|0\rangle_{Hi}. \tag{3.6}$$

The evolution of this state is:

$$|\Psi(t)\rangle = \exp\left\{\frac{-i\hat{H}_I t}{\hbar}\right\}|\Psi_0\rangle. \tag{3.7}$$

The interaction Hamiltonian from equation 3.5 have no temporal dependence. In this case, we can perform the Taylor expansion of the exponential:

$$|\Psi(t)\rangle \approx \left[1 - \frac{-i\hat{H}_I t}{\hbar} + \frac{1}{2}\left(\frac{-i\hat{H}_I t}{\hbar}\right)^2 + \cdots\right]|\Psi_0\rangle \tag{3.8}$$

This expansion is necessary to perform the calculation of how this Hamiltonian operates into $|\Psi\rangle_0$.

We will do the calculation of every order separately using the following notation:

$$\begin{aligned} |0\rangle_s &= |0\rangle_{Vs}|0\rangle_{Hs} \\ |V\rangle_s &= |1\rangle_{Vs}|0\rangle_{Hs} \\ |H\rangle_s &= |0\rangle_{Vs}|1\rangle_{Hs}, \end{aligned} \tag{3.9}$$

and $\mu = t\eta$. The first therm is just the vacuum state $|\Psi_0\rangle$. The first order is:

$$\frac{-i\hat{H}_I t}{\hbar}|\Psi_0\rangle = -i\mu\left(|V\rangle_s|H\rangle_i + |H\rangle_s|V\rangle_i\right). \tag{3.10}$$

The therms related to the *h.c* part of equation 3.5 are zero. The second term of the expansion is:

$$\begin{aligned}\frac{1}{2}\left(\frac{-i\hat{H}_I t}{\hbar}\right)^2 |\Psi_0\rangle &= -\frac{1}{2}\frac{\mu\hat{H}_I t}{\hbar}\left(|V\rangle_s |H\rangle_i + |H\rangle_s |V\rangle_i\right) \\ &= \frac{-\mu^2}{2}\left(|2V\rangle_s |2H\rangle_i + |2H\rangle_s |2V\rangle_i + 2\,|V\rangle_s |H\rangle_s |V\rangle_i |H\rangle_i + |0\rangle_s |0\rangle_i\right) \\ &= \frac{-\mu^2}{2}\,|0\rangle_s |0\rangle_i\,. \end{aligned} \tag{3.11}$$

Here we drop all terms with orders higher than μ^2 except the vacuum therm that represents the situation where the photon is created and annihilated again by the media, creating a higher-order process. This part came by the *h.c.* part of equation 3.5. However, it is a process with a low probability.

Substituting equations 3.10 and 3.11 into equation 3.8 we obtain:

$$|\Psi(t)\rangle = \left(1-\frac{\mu^2}{2}\right)|0\rangle_s |0\rangle_i - i\mu\left(|V\rangle_s |H\rangle_i + |H\rangle_s |V\rangle_i\right). \tag{3.12}$$

By analyzing equation 3.12, we can see that the first therm represents the situation where the signal and idler are still at a vacuum state. The second term is the important one, as it represents the state that came by SPDC for a type-II crystal where we are working at the intersection points of the cones. Normalizing this therm, we then obtain one of the Bell states that are maximally entangled:

$$\left|\Psi^+\right\rangle = \frac{1}{\sqrt{2}}\left(|V\rangle_s |H\rangle_i + |H\rangle_s |V\rangle_i\right). \tag{3.13}$$

The four bell states are:

$$\left|\Psi^\pm\right\rangle = \frac{1}{\sqrt{2}}\left(|V\rangle_s |H\rangle_i \pm |H\rangle_s |V\rangle_i\right), \tag{3.14}$$

and

$$\left|\Phi^\pm\right\rangle = \frac{1}{\sqrt{2}}\left(|H\rangle_s |H\rangle_i \pm |V\rangle_s |V\rangle_i\right). \tag{3.15}$$

This Type-II source is capable of produce all four Bell states by using additional wave plates. To go from a $|\Psi\rangle$ to a $|\Phi\rangle$ state, we can set a half waveplate at 45° at one of the arms. By doing it we transform the photons from $|H\rangle$ ($|V\rangle$) to $|V\rangle$ ($|H\rangle$). Using a quarter waveplate, we can set the relative phase at the pump and tune the $\pm$ signal at equations 3.14 and 3.15. It is also possible to produce these states using two type-I crystals by adjusting the relative configuration between both crystals (their ordinary axis need to be at 90°) and by using additional wave plates.

3.1.2 Remote state preparation

This work aims to produce a post-selection-free remote state preparation in the single-photon regime. Our task is to produce a single-photon state at the signal. For this purpose, we project the idler into a polarization state to remotely produce the signal's state. However, as our degree of freedom has two dimensions, we have two possibilities of states for the idler, and consequently, two for the signal. It means if we do not post-select, our results are right 50% of the time. This section describes the procedure for the state correction to have all photons at the desired state.

When we perform a projective measurement in polarization at the idler we have these two possible states:

$$|\Psi\rangle_i = \alpha\,|H\rangle_i + \beta\,|V\rangle_i \tag{3.16}$$

or

$$\left|\Psi^{\perp}\right\rangle_i = \alpha\,|V\rangle_i - \beta^*\,|H\rangle_i\,, \tag{3.17}$$

where:

$$\begin{aligned}\alpha &= \cos\frac{\theta}{2}\\ \beta &= \sin\frac{\theta}{2}e^{i\phi}.\end{aligned} \tag{3.18}$$

To obtain these states, we project one of the sides of the bi-photon state into another polarization state using a half waveplate (HWP) and a quarter waveplate (QWP), and we split the projections into the states $|\Psi\rangle$ and $\left|\Psi^{\perp}\right\rangle$ using a polarization beam-splitter (PBS), where they are related to the vertical and horizontal ports respectively. Although we chose the initial state of our system to be a singlet Bell state Ψ^{-}, because of the entanglement, when we project the idler into one polarization state, we remotely prepare the signal state as:

$$|\Psi\rangle_s = \left\langle\Psi^{\perp}\right|_i |\Psi^{-}\rangle = \alpha\,|H\rangle_s + \beta\,|V\rangle_s \tag{3.19}$$

or

$$\left|\Psi^{\perp}\right\rangle_s = \langle\Psi|_i\,|\Psi^{-}\rangle = \alpha\,|V\rangle_s - \beta^*\,|H\rangle_s \tag{3.20}$$

As our initial state is a $|\Psi^{-}\rangle$, by projecting the idler into a know polarization state and detecting it, we know the signal state without the need to measure it. With the knowledge of the actual state, we can decide to do nothing if we already have the correct state, mathematically represented by the identity operation $U_A = \mathbb{1}$, or we correct the state by implementing a unitary operation U_B. By doing that, we guarantee that our photons are always at the state $|\Psi\rangle_s$:

$$\text{if}\begin{cases}|\Psi\rangle_i = \left|\Psi^{\perp}\right\rangle_i \rightarrow \mathbb{1}\,|\Psi\rangle_s = |\Psi\rangle_s\,,\\ |\Psi\rangle_i = |\Psi\rangle_i \rightarrow U_B\left|\Psi^{\perp}\right\rangle_s = |\Psi\rangle_s\,.\end{cases} \tag{3.21}$$

It is essential to mention that there is no universal operation U_B that would correct any unknown state [97]. Because of this reason, we chose two families of states to work with. The first family is the one that we call "real projection", where we focus on states at the meridian plane (HDVA) of the Bloch Sphere. The second one is the "complex projection", where the states are at the sphere's equatorial plane (DRAL) plane. We provide better details of every family, and it is respective U_B in the following subsections.

3.1.2.1 Real projection - meridian plane

We create the "real states" using an HWP and removing the QWP at the idler projection station. With these configurations of waveplates, we obtain the following states:

$$|\Psi\rangle_i = \cos\frac{\theta}{2}|H\rangle_i + \sin\frac{\theta}{2}|V\rangle_i. \tag{3.22}$$

and

$$\left|\Psi^\perp\right\rangle_i = \cos\frac{\theta}{2}|V\rangle_i - \sin\frac{\theta}{2}|H\rangle_i. \tag{3.23}$$

The θ here is the angle of the projection. However, we can relate the angle of the state θ with the angle the HWP θ' as:

$$\theta = 4\theta', \tag{3.24}$$

by setting the HWP from 0° to 90°, we perform a complete round at the Bloch sphere at the HDVR plane.

We need find the U_B that transforms the equation 3.22 into equation 3.23 $\left(|\Psi\rangle = U_B\left|\Psi^\perp\right\rangle\right)$. First we need to do the following transformation $|H\rangle \Leftrightarrow |V\rangle$ at $\left|\Psi^\perp\right\rangle$, it can be done by implementing σ_x, as:

$$\left|\Psi^\perp\right\rangle = \cos\frac{\theta}{2}|H\rangle - \sin\frac{\theta}{2}|V\rangle. \tag{3.25}$$

We still have a wrong sign for the $|V\rangle$ state. The way of changing it without changing $|H\rangle$ is implementing σ_z, then we have:

$$\sigma_z\sigma_x\left|\Psi^\perp\right\rangle = \cos\frac{\theta}{2}|H\rangle + \sin\frac{\theta}{2}|V\rangle = |\Psi\rangle. \tag{3.26}$$

For the real states we found the U_B that *fix* the orthogonal state. We can write U_B as:

$$\sigma_z\sigma_x = \begin{bmatrix}1 & 0\\ 0 & -1\end{bmatrix}\begin{bmatrix}0 & 1\\ 1 & 0\end{bmatrix} = \begin{bmatrix}0 & 1\\ -1 & 0\end{bmatrix} = i\sigma_y. \tag{3.27}$$

We then obtain $U_B = i\sigma_y$. With a QWP, HWP, and another QWP, it is possible to implement a unitary operation that transforms one state to another arbitrary point inside the Bloch sphere. In the experimental section, we provide details about the experimental implementation of this unitary operation.

3.1.2.2 Complex projection - equatorial plane

For the complex states at the equatorial plane of the Bloch sphere, we have $\theta = 90°$. With α and β from equation 3.18 we have the following states:

$$|\Psi\rangle_i = \frac{1}{\sqrt{2}}\left[|H\rangle_i + e^{i\phi}\,|V\rangle_i\right] \tag{3.28}$$

and

$$\left|\Psi^{\perp}\right\rangle_i = \frac{1}{\sqrt{2}}\left[|V\rangle_i - e^{-i\phi}\,|H\rangle_i\right]. \tag{3.29}$$

We can prepare these states by setting the QWP at 45° and, vary the HWP from 22.5° to 90°, where we perform a complete round at the DRAL plane. Here we can relate the angle for the HWP θ' and ϕ as:

$$\phi = 4(\theta' - 22.5°) \tag{3.30}$$

The algorithm to correct the state is similar to the one for the real projections. However, we need to take care that now we have a phase on $|V\rangle$. First we implement a σ_X to $|H\rangle \Leftrightarrow |V\rangle$:

$$\sigma_X\left|\Psi^{\perp}\right\rangle = \frac{1}{\sqrt{2}}\left[|H\rangle - e^{-i\phi}\,|V\rangle\right]. \tag{3.31}$$

Here we have two problems now: (i) the negative sign of $|V\rangle$ and, (ii) the relative phase is with a opposite signal in relation to $|\Psi\rangle$. In order to solve both problems we implement σ_Y:

$$\sigma_Y\sigma_X\left|\Psi^{\perp}\right\rangle = \frac{i}{\sqrt{2}}\left[|V\rangle + e^{-i\phi}\,|V\rangle\right]. \tag{3.32}$$

Now we have a global phase $i = e^{\frac{\pi}{2}}$ and the phase at $|H\rangle$, still with the opposite sign. For our work, a global phase is not a problem, so we can isolate the $e^{-i\phi}$ at $|H\rangle$. We also multiplied both sides by $-i$, then we obtain:

$$i\sigma_Y\sigma_X\left|\Psi^{\perp}\right\rangle = -\frac{e^{-i\phi}}{\sqrt{2}}\left[|H\rangle + e^{+i\phi}\,|V\rangle\right] = e^{-i(\phi-\pi)}\,|\Psi\rangle. \tag{3.33}$$

We wrote the negative signal in a polar form to sum with the previous phase, and then we found the global phase $e^{-i(\phi-\pi)}$. We can write the product of $\sigma_Y\sigma_X$ as:

$$i\sigma_Y\sigma_X = i\begin{bmatrix}0 & -i\\ i & 0\end{bmatrix}\begin{bmatrix}0 & 1\\ 1 & 0\end{bmatrix} = \begin{bmatrix}1 & 0\\ 0 & -1\end{bmatrix} = \sigma_Z. \tag{3.34}$$

We then obtain $U_B = \sigma_Z$ as the unitary operation that corrects the perpendicular states at the equator line of the Bloch sphere.

3.1.3 Projecting a two-photon state

This section describes the algorithm we used to predict the single-photon state, considering that the initial state is a theoretical Bell or a two-photon experimental state. First, nevertheless, we need to write the density matrix of our state:

$$\rho^{-} = |\Psi^{-}\rangle\langle\Psi^{-}| = \begin{bmatrix} 0 & 0 & 0 & 0 \\ 0 & 0.5 & -0.5 & 0 \\ 0 & -0.5 & 0.5 & 0 \\ 0 & 0 & 0 & 0 \end{bmatrix}. \tag{3.35}$$

Using the Jones formalism, we can write the operator that rotates our initial state at the idler project station:

$$Rot_i = HWP(\theta')QWP(\phi), \tag{3.36}$$

where the matrix that represents an HWP that is rotated θ° from the horizontal axis is:

$$HWP(\theta) = \begin{bmatrix} cos^2(\theta) - sin^2(\theta) & 2cos(\theta)sin(\theta) \\ 2cos(\theta)sin(\theta) & sin^2(\theta) - cos^2(\theta) \end{bmatrix} \tag{3.37}$$

and for the QWP we have:

$$QWP(\theta) = \begin{bmatrix} cos^2(\theta) + isin^2(\theta) & (1-i)cos(\theta)sin(\theta) \\ (1-i)cos(\theta)sin(\theta) & sin^2(\theta) + icos^2(\theta) \end{bmatrix}. \tag{3.38}$$

Here we omit the phases that the waveplates create as they do not disturb our system. The projection operators are for a single-photon state, so we need to increase its rank as:

$$Rot_{2D} = \mathbb{1} \otimes Rot_i. \tag{3.39}$$

This procedure is necessary for all-optical elements in the Jones formalism. We will use $2D$ as a notation when we increase the matrix operator's rank.

We perform the density matrix projection as:

$$\rho_{rot} = Rot_{2D}\,\rho\,Rot^{\dagger}_{2D}. \tag{3.40}$$

Now we need to split the polarization components as in a PBS. It can be done mathematically by using the H and V polarizers for a single photon state as:

$$PolH = \begin{bmatrix} 1 & 0 \\ 0 & 0 \end{bmatrix}; \qquad PolV = \begin{bmatrix} 0 & 0 \\ 0 & 1 \end{bmatrix}. \tag{3.41}$$

We use ρ^H as notation for the state remotely prepared at the signal when the idler leaves the horizontal output at the PBS, and ρ^V if it leaves the vertical output. To perform this calculation, we need first project ρ_{proj} at $PolH_{2D}$ and $PolV_{2D}$ to splits its polarization components as:

$$\rho^X = Tr_{idler}\left(\rho_{rot}\, PolX_{2D}\right), \tag{3.42}$$

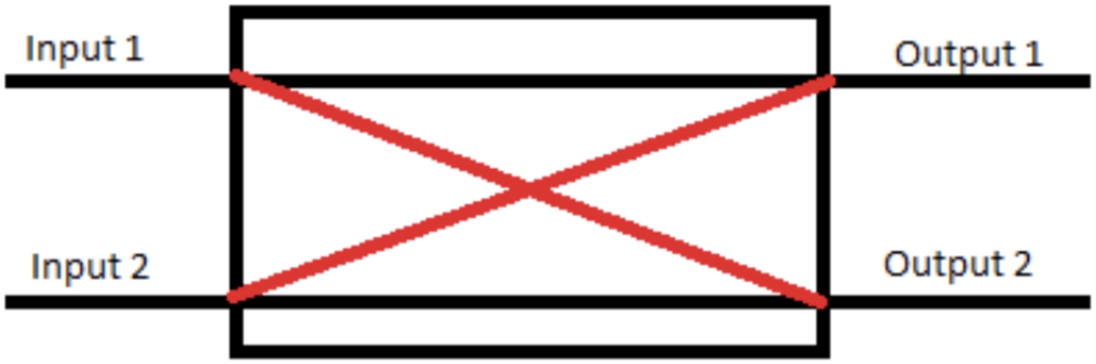

Figure 17 – In this figure, we show a schematic version of the UFOS operation. It has two inputs(1/2) and outputs (1/2), and at the ground state configuration, it operates, in what we call bar-state, where the photons are sent to the respective output (1 → 1). When we send a pulse to the UFOS, it switches and goes to the cross-state where we have the input/outputs crossed (1 → 2), i.e., the photons that arrive from one leave on two and vice-versa.

where X is $H\backslash V$ and Tr_{idler} is the partial trace over the idler subsystem. The resulting state is a single-photon state for the signal. Therefore we need to normalize both single-photons density matrices as:

$$\rho^X_{norm} = \frac{\rho^X}{Tr(\rho^X)}. \tag{3.43}$$

We can now relate the $H\backslash V$ clicks at the idler projective station as $|\Psi\rangle_i \backslash \left|\Psi^{\perp}\right\rangle_i$. Comparing it to equation 3.21 we can see that when the detector at the V output clicks we already have the right state at the signal side (ρ^V_{norm}), meaning it need no corrections. However, if we have an H click we need to implement U_B to correct ρ^H, as:

$$\rho^H_{corrected} = U_B\, \rho^H_{norm}\, U^\dagger_B. \tag{3.44}$$

The final state at the signal arm is the sum of both components as:

$$\rho_{final} = \frac{1}{2}\left(\rho^H_{corrected} + \rho^V_{norm}\right). \tag{3.45}$$

3.1.4 Ultrafast Optical switches

In this section, we describe the functioning of the Ultrafast optical switches (UFOS). This device is the core of our feed-forward technique that allows us to efficiently rout the photons through the path that implement the desired unitary transformation. They are a wave-guide device that has two inputs/outputs of mono-mode optical fibers and, depending on the voltage applied it can cross the paths as shown in Figure 17.

The device we choose is the 2x2 in-fiber ultrafast optical switches from the BATi 2x2 Nanona switch, developed for $\lambda = 1550\ nm$. It can operate with a maximum

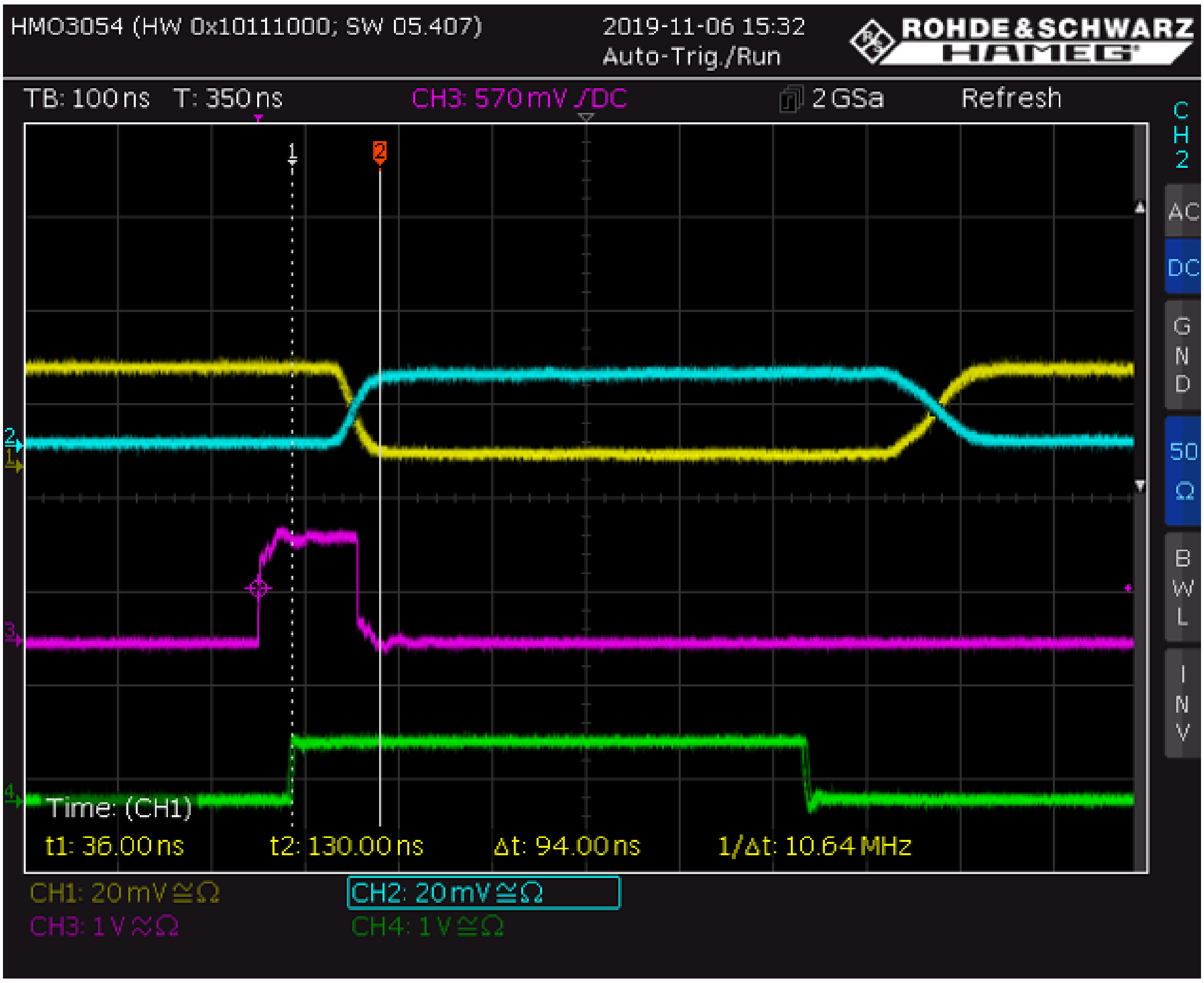
HMO3054 (HW 0x10111000; SW 05.407)
2019-11-06 15:32
Auto-Trig./Run
TB: 100 ns T: 350 ns
CH3: 570 mV /DC
2 GSa
Refresh
Time: (CH1)
t1: 36.00 ns
t2: 130.00 ns
Δt: 94.00 ns
1/Δt: 10.64 MHz
CH1: 20 mV ≅Ω
CH2: 20 mV ≅Ω
CH3: 1 V ≈Ω
CH4: 1 V ≅Ω

Figure 18 – Here we show one of the tests made to characterize the UFOS functioning. We couple a $\lambda = 1550$ *nm* laser into Input 1 (yellow curve), where we detect the light at one photodiode on input 1. It means we are maintaining the UFOS at bar-state. Then a single-photon detector clicks, generating a pulse that is the purple curve. The FPGA (field-programmable gate array) reads the pulse, and then it generates a TTL pulse (green curve) sent to UFOS to switch to the cross-state. The whole light is now at the blue curve at the cross-state, the signal from a photodiode in output 2.

repetition rate of 1 *MHz* and has a response time of approximately ≈ 60 *ns*, and across-channel of 20 *dB* for polarization. However, it has unbalanced losses that are approximately ≈ 1.3 *dB*. This unbalanced loss appears from the fact that the fiber-splices and fiber coupling at the waveguide. We perform this characterization with classical light and photodiodes.

Figure 18 demonstrates a tests with classical beam. However, they operate well in the single-photon regime. The limitations that we found are that they are not developed to have intense beams at the two inputs simultaneously, and the 1 *MHZ* repetition rate is a limitation for higher statistics. They have shown to be suitable to our or purposes, that is, the remote state preparation of the single-photon level, presented in this chapter, and the photonic Maxwell's Demon that we describe in chapter 4.

3.2 EXPERIMENTAL RESULTS

This section describes the experimental methodology for the remote state preparation at the single-photon level using the UFOS. When we project to any desired basis, we have the projection we want and an orthogonal one, as we have a bi-dimensional system. To archive this goal, we have two possibilities available: first, post-select the events we want, ignoring the others, losing a big part of our photons with this option. The second one is to correct the *wrong states* using the method described theoretically at section 3.1.2. We choose the second option, where we implement it using the setup from Figure 19.

Here we produced our initial state $|\Psi^{-}\rangle$, as in figure 19 (b), using a ppKPT Sagnac source with polarization as a degree of freedom. For this type of source, we send a laser beam with λ = 775 *nm* through the polarization Sagnac interferometer, where the initial polarization of the pump is at 45°. The beam is focused, and a PBS splits the polarization components of the pump, where the horizontal component (clock-wise) transmits and passes through the type-II ppKPT crystal. It produces a pair of photons in a colinear regime, and we rotate the polarization of the pair in 90°, then the PBS divides the photons through a deterministic path in polarization. The pump's vertical component (anticlockwise) is rotated into a horizontal polarization before it shines the crystal. However, we do not rotate the polarization of the pairs of photons. By rotating the polarization of the pairs in one direction of the interferometer and not in the other creates the pairs as $|HV\rangle \pm |VH\rangle$ and makes them indistinguishable. The pump will always hit the crystal with a horizontal component and leave the interferometer in the upper output of the PBS, and then a dichroic mirror reflects it is wavelength but leaves the photons at 1550 pass. The pump is a CW laser where we use it with an average power of $\approx$ 80 *mw*. After the PBS, we filter the single-photons with bandpass filters with a full width half maximum bandwidth of 3.2 *nm*. We then couple the photons into single-mode optical fibers (SMF28). This configuration generates around 85 *kHz* singles with a 17 *kHz* coincidence rate, being approximately 20% of efficiency.

We send the pair of photons to the setup as in Figure 19 (a). First, the idler goes to the projective measurement station (orange box) to remotely prepare the signal's state, where we implement the projection collimating the photons in free-space inside a Thorlabs fiber u-beach, where we chose the projections by using a QWP and an HWP to them split $|\Psi\rangle_i$ and $\left|\Psi^{\perp}\right\rangle_i$ at the PBS. We couple the photons again at the single-mode fibers to be detected by two superconducting nanowire single-photon detectors (SNSPD) from PhotonSpot Inc, where they have $\approx$ 90% efficiency and 50 *ns* deadtime for λ =1550 *nm*. The pulses produced by the SNSPD are then sent to a commercial time tagging module (TTM) from UQDevices to record the single

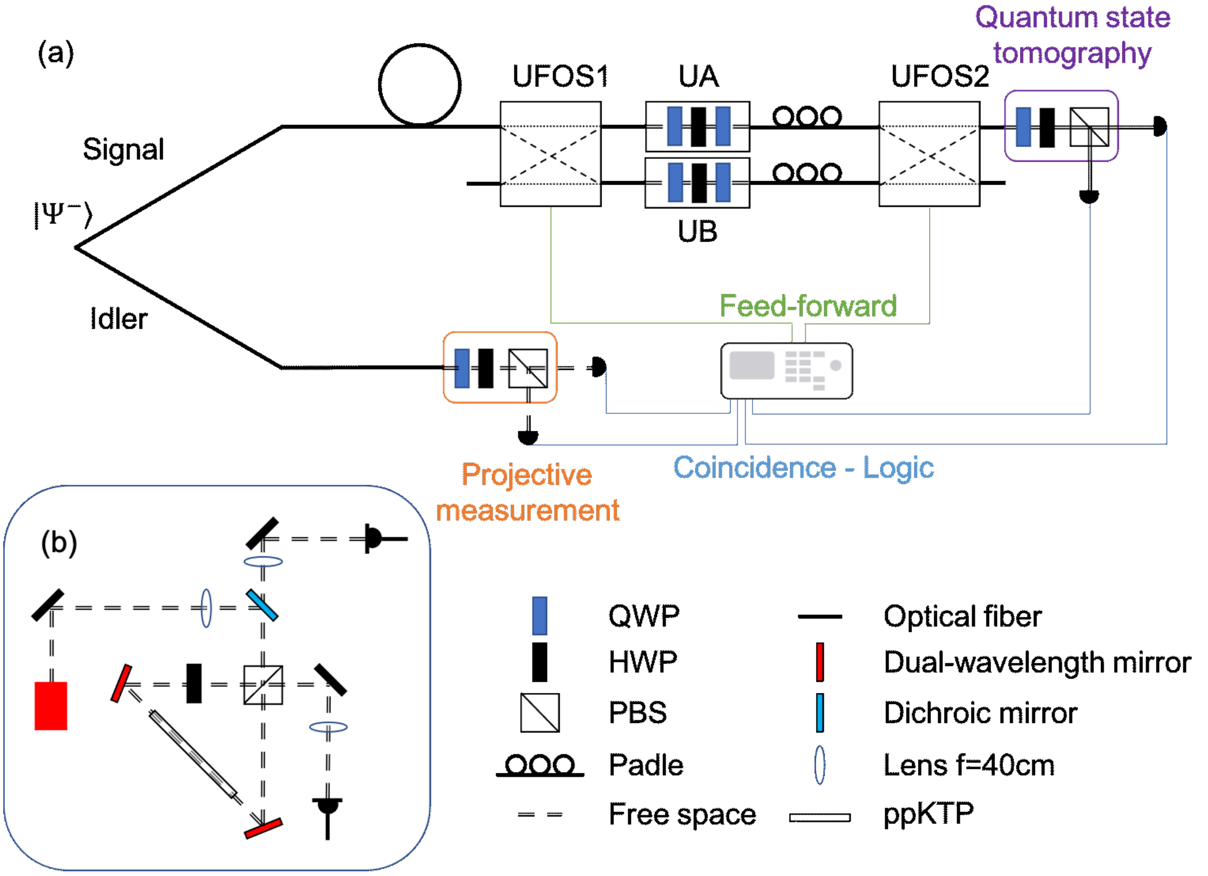

Figure 19 – Figure (a) shows the setup for the remote state preparation at the single-photon level using the UFOS. We prepare a $|\Psi^-\rangle$ state in (b), then we sent the idler through the projective measurement station (orange box), where using a QWP and an HWP, we project it into the desired state. The coincidence logic receives the signals from the photons detected at $|H\rangle$ or $|V\rangle$ output of the PBS, conditioned to who clicks the coincidence-logic send the signal for the UFOS to route the photons through path A or B, depending on if it needs or not to be corrected. The signal photons pass through a delay line, and then the UFOS1 route it to U_A or U_B, UFOS2 routes the photons to the quantum state tomography (purple box), where we measure the single-photon density matrix to verify if all photons are arriving at the same state. In (b) we use a laser with $\lambda = 775$ *nm* through a ppKPT Sagnac source [98] to produce the $|\Psi^-\rangle$ state at $\lambda = 1550$ *nm*.

pulses and analyze the coincidence counts. As a result, we record around 50 *kHz* singles at the projective measurement station and 30 *kHz* singles at the quantum state tomography with approximately 3 *kHz* coincidence rate. This decay of the numbers is mainly because of the losses present at the two switches, the u-benches for the unitary operations and the u-bench for the projective and quantum state tomography station.

Here the clicks at the detector in the vertical output of the projective measurement station (idler) mean that we already prepared the signal photons at the desired state $|\Psi\rangle_S$, as the theory in section 3.1.2, and the unitary operation U_A that we implement is identity $\mathbb{1}$. However, if we have a click at the horizontal output, it means that the state of the signal needs to be corrected using U_B. The TTM is the device that implements the logic to deterministic decide when the state of the signal needs to be corrected or not. However, for this operation, we need to delay the signal photons to guarantee that the UFOS are ready every time that the photon from the signal beams arrives. The delay line we used is with 162 *m* of optical fibers. The physical delay is bigger than we need, but we can easily delay the pulse to control the UFOS electronically. It helps us to be more precise when we synchronize the whole experiment.

Here we need to be able to choose between the unitary operation U_A or U_B conditioned to the prepared state. There are two usual ways of doing it, or we can use Pockels cells [36–39, 79] to implement the operations leaving the path fixed. On the other hand, we take another path to implement our feedforward scheme, leaving the unitary operations U_A and U_B fixed and routing the photons to the correct one. We take this path as our system is fiber-based with SMF28 fibers allowing this technique can be applied to the existent telecom infrastructure. However, we use a free-space component in our setup for the unitary's transformation implementation inside the u-bench system. We choose it by its stability, which creates losses around 0.7 *dB*, smaller than those present at the UFOS $\approx$ 1.3 *dB*. Using two UFOS, we implement this re-routing logic, where the photons arrive and leave at the correct input/output independently of the state of the idler. If the signal is at the right state (V click), we leave the UFOS at bar-state, and the photon passes through the upper path where we implement $U_A = \mathbb{1}$ by removing the waveplates and then sent to the quantum state tomography. However, if the H detector clicks, the TTM sends a TTL pulse (square pulse of 5V high) of 700 *ns* to the UFOS1 and 2 to switch then to the cross-state. The UFOS1 sends the photon to U_B, where it is corrected, and UFOS2 returns the photon to the quantum state tomography. By implementing the correct U_B, by our detection scheme, it is not possible to know if the signal state was initially at $|\Psi\rangle_s$ or $\left|\Psi^{\perp}\right\rangle_s$. This is the core of our fiber-based technique to implement the feedforward for the single-photon state preparation.

Figure 20 illustrates how the protocol works reconstructing the single-photon density matrix [99] of the signal state. Initially the idler state is measured in the $(|H\rangle \pm |V\rangle)/\sqrt{2}$ basis. All plots from figure 20 illustrates the same projected state. However, for (a) and (d), we post-select the results with the clicks at the horizontal output of the PBS at the projection state, for (b) and (e) we post-select with the reflected port at the PBS and, (c) and (f) is the complete single-photon tomography. For the results without feed-forward (a) to (c), we can see that at (a) (H - click for the idler) the signal state collapses to $(|H\rangle - |V\rangle)/\sqrt{2}$ and at (b) (V - click for the idler) it collapses to $(|H\rangle + |V\rangle)/\sqrt{2}$. As we perform no feed-forward, the result at (c) is when we consider both contributions, result in a mixed state. However, with feed-forward active, we can see that we have the same state, besides experimental imperfections for the corrected state (d), (e), and the complete state at (f).

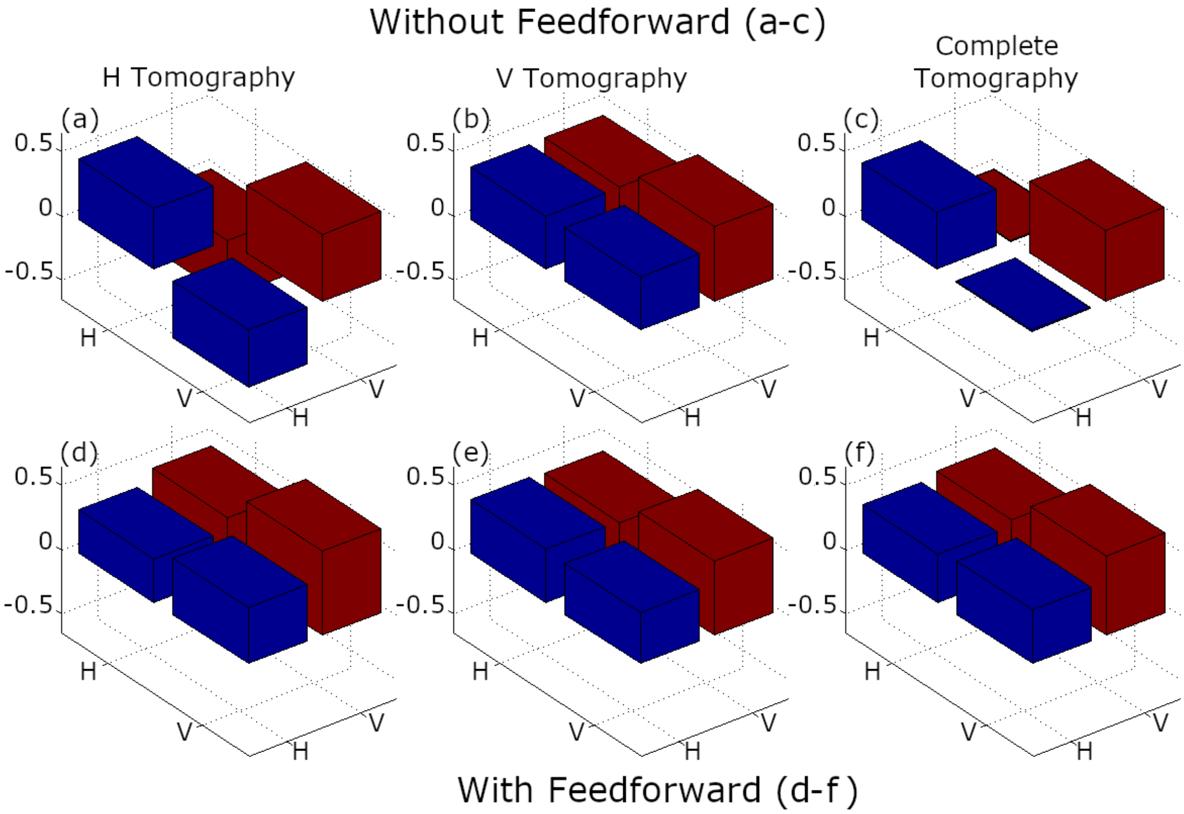

Figure 20 – Here we have the real part of the single-photon density matrices without (a) to (c) and with (d) - (f) feed-forward. The imaginary part was omitted as it is close to zero for all cases. H (V) tomography is the case when we post-select the coincidences at the projective measurement station. Complete tomography is when no post-selection is performed.

To perform the data analysis of all experimental results, we first reconstruct the two-photon density matrix as [99], where we perform all combinations of measurements (36) between the two photons on a linear, diagonal and circular basis. For the single-photon density matrix reconstitution, we also perform the measurements in these three bases. The table 2 shows the angles of the QWP and HWP for all measurement sets, and it is combinations.

We then project the $|\Psi^{-}\rangle$ state using the method of section 3.1.3 to obtain the single-photon state that we measure at the end. We then calculate the fidelity of the theoretical and the experimental state to evaluate how similar our state is to the desired one. The definition of the fidelity between two arbitrary density matrices ρ and σ is [100] :

$$F(\rho\sigma) \equiv Tr\sqrt{\sqrt{\rho}\sigma\sqrt{\rho}}. \tag{3.46}$$

One important property of the fidelity is that it is symmetric.

We first compare the results of both families of states with the measurements when no feed-forward is applied, as in figure 20 (c), as discussed before, if we implement no feed-forward, we have a mixed state, then we found an average fidelity of (49 ±

Single-Photon Measurement Set	Two-Photon State Tomography	
	QST	PM
(1) 0°_{HWP}, 0°_{QWP}	(1) 0°_{HWP}, 0°_{QWP}	0°_{HWP}, 0°_{QWP}
(2) 0°_{HWP}, 45°_{QWP}	(2) 0°_{HWP}, 0°_{QWP}	22.5°_{HWP}, 45°_{QWP}
(3) 22.5°_{HWP}, 45°_{QWP}	(3) 0°_{HWP}, 0°_{QWP}	0°_{HWP}, 45°_{QWP}
	(4) 22.5°_{HWP}, 45°_{QWP}	0°_{HWP}, 45°_{QWP}
	(5) 22.5°_{HWP}, 45°_{QWP}	22.5°_{HWP}, 45°_{QWP}
	(6) 22.5°_{HWP}, 45°_{QWP}	0°_{HWP}, 45°_{QWP}
	(7) 0°_{HWP}, 45°_{QWP}	0°_{HWP}, 0°_{QWP}
	(8) 0°_{HWP}, 45°_{QWP}	22.5°_{HWP}, 45°_{QWP}
	(9) 0°_{HWP}, 45°_{QWP}	0°_{HWP}, 45°_{QWP}

Table 2 – Set of waveplate angles used to perform the single-photon and two-photon quantum state tomography. Here PM means projective measurement and station and QST quantum state tomography station.

2)% for both measurements. We then calculated the fidelities of the theoretical and experimental states obtaining an average fidelity of (91 ± 1)% and (92 ± 1)% for the real and complex states, respectively. These fidelities came from the fact that the fidelities of our two-photon state and the $|\Psi^{-}\rangle$ is around (92 ± 1)% and its purity it is (89 ± 2)%, this error came by the fact that the polarization compensation was complicated for this setup as we have several paths and specific points where we need to have the polarization corrected, making the final two-photon state, not a "perfect" Bell state.

However, our main objective is to characterize our fiber-based feed-forward technique using the UFOS to see if it is suitable for the task and not create a perfect Bell state. For this reason, we projected the experimental two-photons density matrices into the states, as in section 3.1.3, to predict the projected state. With this prediction, we calculate the fidelity of this state compared to the single-photon experimental states with our feed-forward protocol. By doing that, we remove the errors relate to state generation. As a result, we increased our fidelities to (99.0 ± 1)% for both measurement sets.

In the following two subsections, we present the results for the two families of states described in section 3.1.2. Then, in section 3.2.1 we show the results for the real states, where the states are at the meridian of the Bloch sphere, and in section 3.2.2 we present the results for the complex states, the ones at the equator line of the Bloch sphere.

3.2.1 Results for the Real projection

Here we present the results for the projection under real states, the meridian of the Bloch sphere, where we have the following states:

$$\begin{aligned} |\Psi\rangle_i &= \cos\frac{\theta}{2}\,|H\rangle + \sin\frac{\theta}{2}\,|V\rangle \\ \left|\Psi^{\perp}\right\rangle_i &= \cos\frac{\theta}{2}\,|V\rangle - \sin\frac{\theta}{2}\,|H\rangle . \end{aligned} \tag{3.47}$$

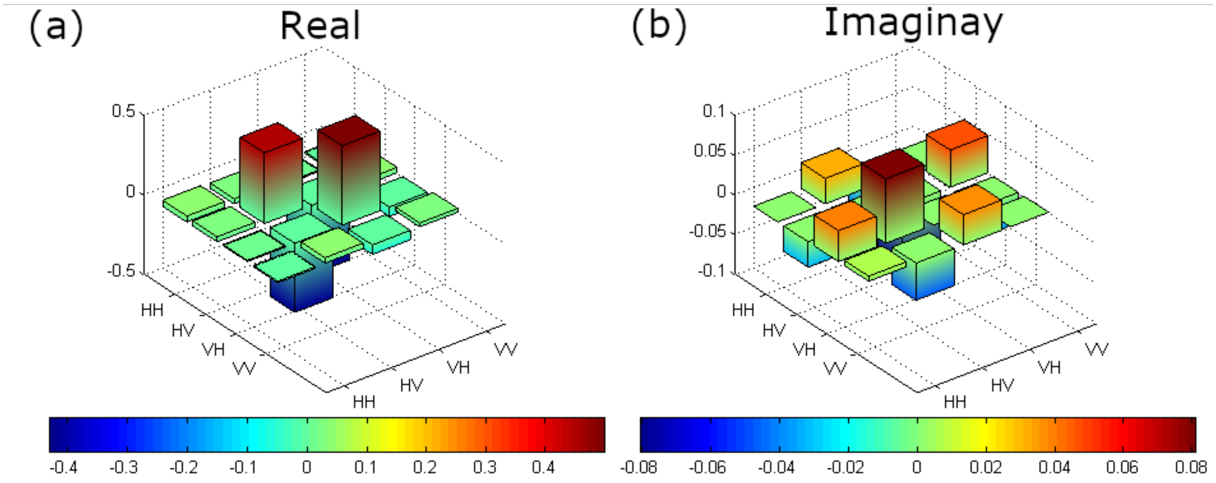

Figure 21 – In (a) we have the real part of the density matrix of equation 3.49 , and in (b) is the imaginary part.

Experimentally we obtain these states by removing the QWP and varying the HWP from 0° to 90° at the projective measurement station. Here is essential to note that as the projection is the product of a QWP and an HWP, just setting the QWP as 0° has a different effect as removing it. The unitary operation is $U_B = i\sigma_y$, where we implement it with the following waveplate angles:

$$i\sigma_y = QWP(90°)HWP(45°)QWP(0°) = e^{i\frac{\pi}{4}}\begin{bmatrix} i & 0 \\ 0 & 1 \end{bmatrix} e^{-i\frac{\pi}{2}}\begin{bmatrix} 0 & 1 \\ 1 & 0 \end{bmatrix} e^{i\frac{\pi}{4}}\begin{bmatrix} 1 & 0 \\ 0 & i \end{bmatrix} = \begin{bmatrix} 0 & -1 \\ 1 & 0 \end{bmatrix}, \tag{3.48}$$

where the fast axis of the waveplates is at H.

The measurements of both sets were performed on different days. Because of that, the polarization compensation needs to be done again. For this measurement set, the two-photons density matrix is:

$$\rho_{real} = \begin{bmatrix} 0.037+0.000i & 0.031+0.032i & 0.007-0.039i & -0.009-0.006i \\ 0.031-0.032i & 0.442+0.000i & -0.432-0.081i & 0.034+0.047i \\ 0.007+0.039i & -0.432+0.081i & 0.497+0.000i & -0.059-0.038i \\ -0.009+0.006i & 0.034-0.047i & -0.059+0.038i & 0.024+0.000i \end{bmatrix} \tag{3.49}$$

This is the density matrix that we use for the predictions in this measurement set. This density matrix is plotted at Figure 21, where (a) represent it's real, and (b) imaginary components. We can see that the imaginary part is considerably smaller than the real one. If we have a perfect bell state, all imaginary components would be zero. As we mentioned before, this state has a fidelity of (91 ± 1)%, and its purity is (89 ± 2)%.

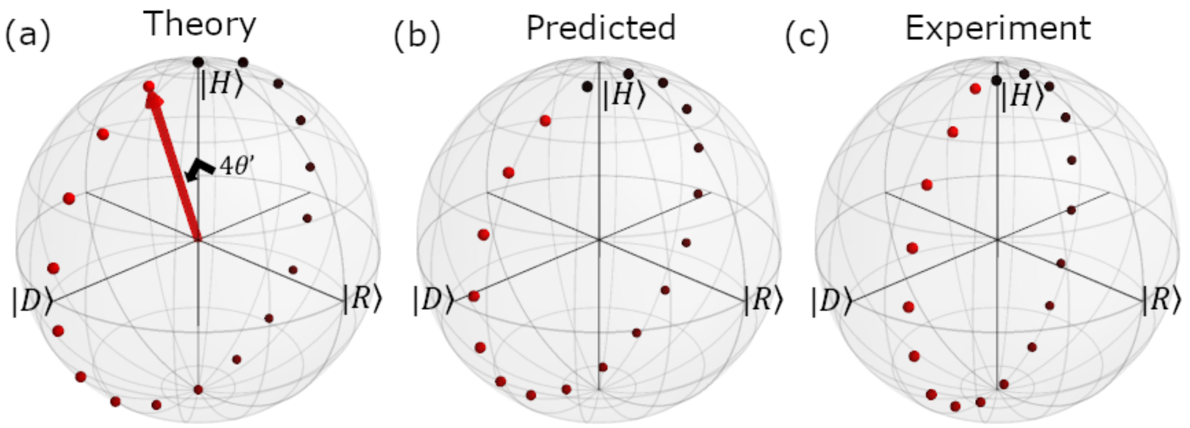

Figure 22 – Here we have the Theory (a), predicted (b) and, experiment (c) single-photon states at the Bloch sphere. Theory means the theoretical state predicted by the $|\Psi^{-}\rangle$ state, predicted is the state that we expect to have after measuring the actual two-photon state we produce and, experiment is the experimental points for this measurement set. For this family states, the relation between the angle of the waveplates θ' and the angle of the states θ at the sphere is $\theta = 4\theta'$.

From now on, we use the following notation, *Theory* for the theoretical states from $|\Psi^{-}\rangle$, *Predicted* that are the states projected from the two-photon experimental density matrices and *Experiment* that is the experimental data after the feed-forward protocol. In figure 22 we have our states in the Bloch sphere, where (a) is the theory, (b) is the predicted states, and (c) is the experiment. We can observe that they have a quite good agreement.

In figure 23, we show the fidelities where we vary θ' from 0° to 90° in steps of 5°. We first reconstruct the experimental density matrix of each measurement to calculate the relative fidelities then. First, we start with the measurements with no feed-forward, as is the case of figure 20 (c). Comparing the experimental states with the theoretical predictions we show in figure 23 (a) that we have in average (49 ± 2)%. These low fidelities happen as we apply no feed-forward to the single-photon states, making it a mixed state. We repeat the measurements now with the protocol On. In this case, we then obtain the fidelities of 23 (b), wherein average we have (91 ± 1)%. This fidelity average shows that our state is in good agreement with the theoretical predictions, but they do not consider the experimental errors in preparing the initial state, which can be explained by the fidelity of our initial state (92 ± 1)%. Figure 23 (c) now takes into account these errors as we are now comparing the results with the two-photon experimental state. In this situation, we increase the average fidelities to (99.0 ± 1)%, a big improvement, showing that our technique produces the highest fidelities to our knowledge on the data of our work publication [95].

The straight lines in figure 23 (b) (green line) and (c) (blue line) are simulations, where we include 1% polarization loss, which is consistent with the UFOS specifications

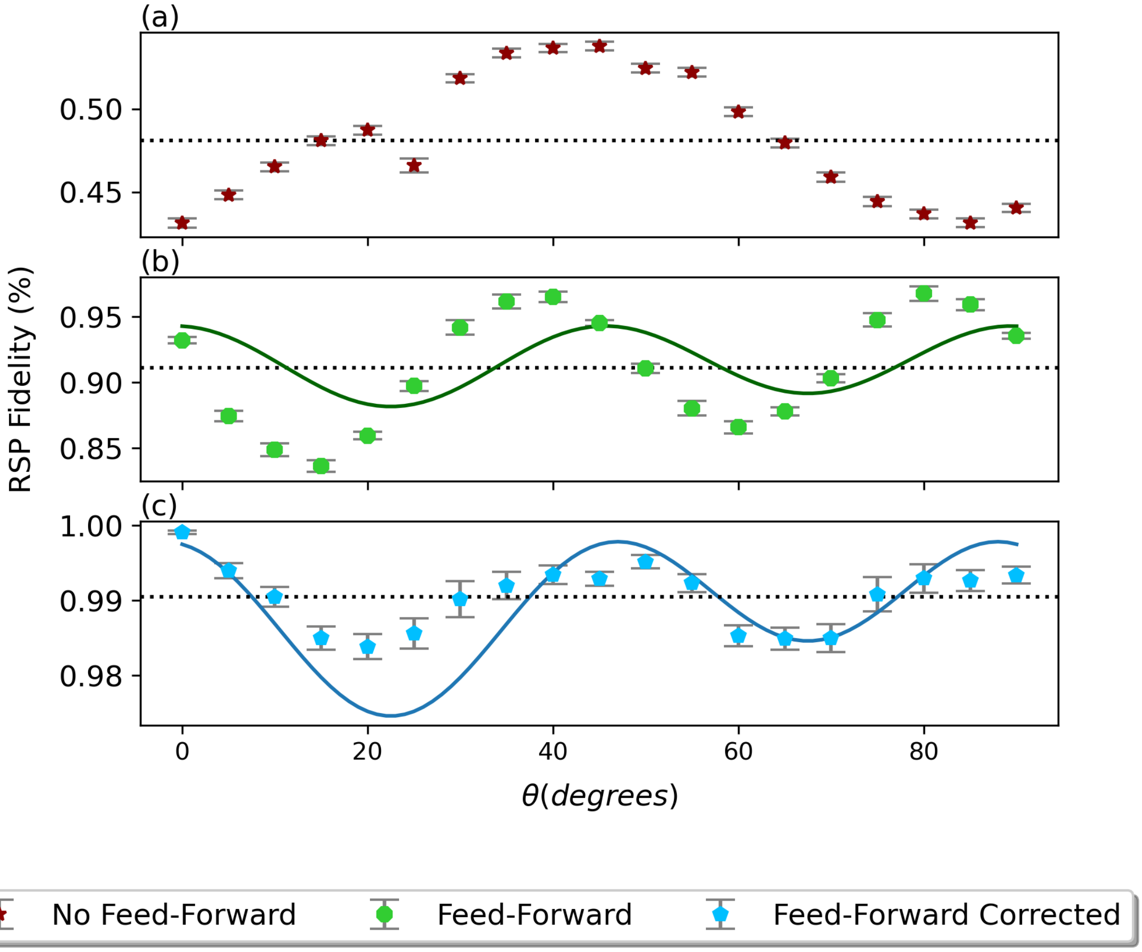

Figure 23 – Here we show the fidelities for no feed-forward (a), fidelities where the feed-forward protocol is on with the theoretical states (b), and the last one is the fidelities between the predicted and the experimental states (c).

(< 0.2 *dB*). We also include a residual birefringence of 0.5 rad related to polarization compensation. We consider the purity of 0.89 for our Bell state. It was sufficient to show the oscillations that we found in our experimental data. The error bars are generated by a Monte Carlo simulation that starts with the experimental data and considers uncertainties of 0.5° in waveplate setting plus adding Poissinian fluctuations from 40, 000 counts.

3.2.2 Results for the Complex projection

Here we present the results for the projection under complex states, the equatorial line of the Bloch sphere. These states have the following form:

$$\begin{aligned} |\Psi\rangle_i &= \frac{1}{\sqrt{2}}\left[|H\rangle + e^{i\phi}|V\rangle\right] \\ \left|\Psi^{\perp}\right\rangle_i &= \frac{1}{\sqrt{2}}\left[|V\rangle - e^{-i\phi}|H\rangle\right]. \end{aligned} \tag{3.50}$$

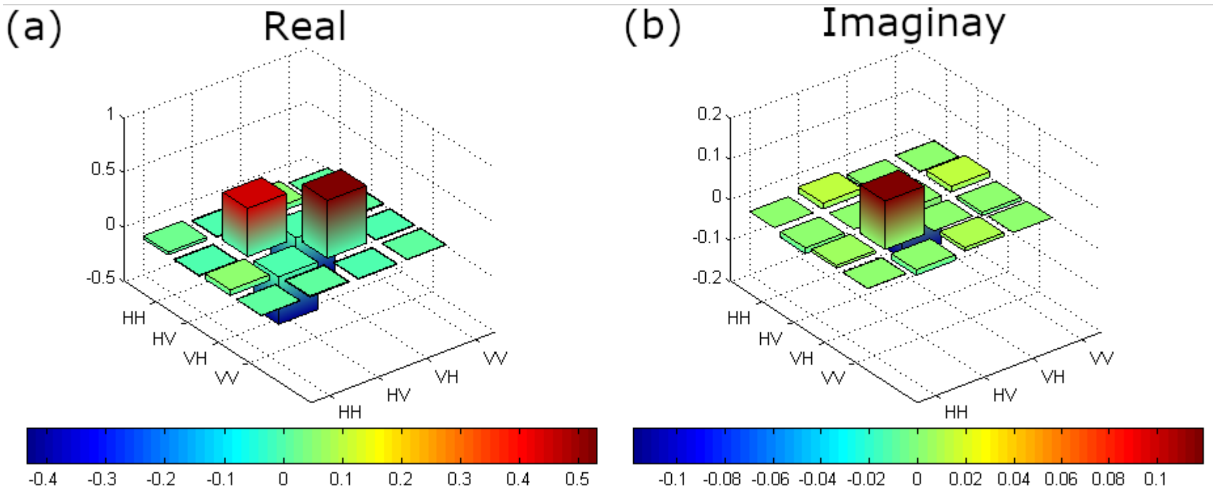

Figure 24 – In (a) we have the real part of the density matrix of equation 3.52 , and in (b) is the imaginary part.

To experimentally create these states, we leave the QWP at 45° and varying the HWP from 22.5° to 112.5° at the projective measurement station. The unitary operation is $U_B = \sigma_Z$, where we implement it with the following waveplate angles:

$$\sigma_Z = QWP(90°)HWP(0°)QWP(0°) = e^{i\frac{\pi}{4}}\begin{bmatrix} i & 0 \\ 0 & 1 \end{bmatrix} e^{-i\frac{\pi}{2}}\begin{bmatrix} 1 & 0 \\ 0 & -1 \end{bmatrix} e^{i\frac{\pi}{4}}\begin{bmatrix} 1 & 0 \\ 0 & i \end{bmatrix} = \begin{bmatrix} 1 & 0 \\ 0 & -1 \end{bmatrix}, \tag{3.51}$$

where the fast axis of the waveplates is at H.

As we perform the measurement sets on different days, we did a new polarization compensation in our system. By doing that we have a new two-photon density matrix as in equation 3.52 which is plotted at figure 24. It has a fidelity of $(92 \pm 1)\%$ and the purity of $(89 \pm 2)\%$. This slightly higher fidelity can be explained by comparing the two density matrices and the plots, as for a perfect Bell state, we have no imaginary components, and for this state they are smaller.

$$\rho_{complex} = \begin{bmatrix} 0.027+0.000i & -0.008+0.014i & 0.051-0.007i & 0.003+0.001i \\ -0.008-0.014i & 0.441+0.000i & -0.434-0.118i & 0.011+0.014i \\ 0.051+0.007i & -0.434+0.118i & 0.528+0.000i & -0.007-0.009i \\ 0.003-0.001i & 0.011-0.014i & -0.007+0.009i & 0.005+0.000i \end{bmatrix} \tag{3.52}$$

The protocol here is the same. We first reconstruct the experimental density matrix, and then we project the theoretical and two-photon (predicted states into the

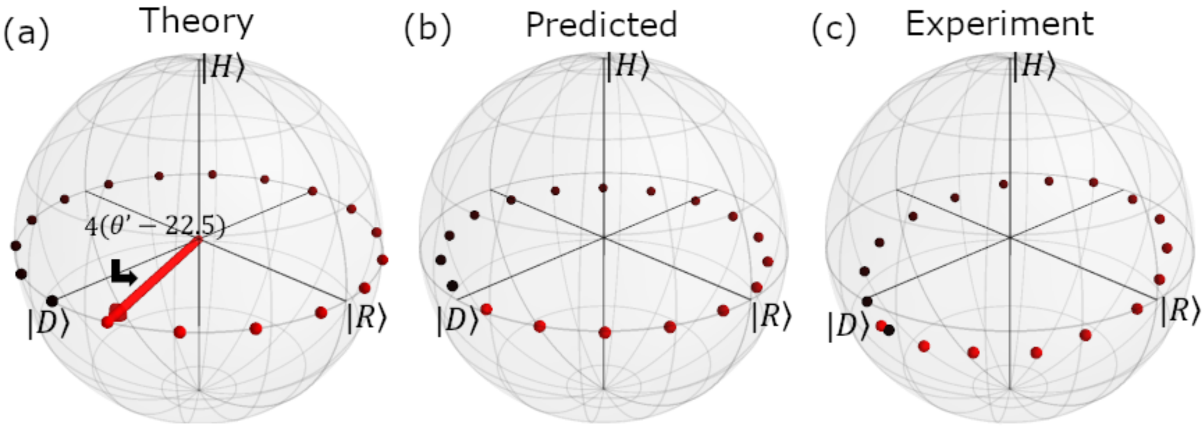

Figure 25 – Here we have the Theory (a), predicted (b) and, experiment (c) single-photon states at the Bloch sphere. For this family states, the relation between the angle of the waveplates θ' and the angle of the states ϕ at the sphere is $\phi = 4(\theta' - 22.5°)$.

complex states. All these states are in figure 25 where (a) is the theoretical, (b) predicted, and (c) experimental states at the Bloch sphere. Every point (HWP angle) has the same color for its representation in all figures.

We calculated the fidelity of our experimental states with no feed-forward, the results in figure 26 (a), where we find an average fidelity of $(51 \pm 1)\%$. This value is consistent with the expected 50% for the protocol without feed-forward. With the feed-forward on, the results in figure 26 (b), we find an average fidelity of $(92 \pm 1)\%$. Here the fidelity with the theoretical state is slightly higher. This improvement can be because the polarization compensation could be slightly better for this set. However, when we calculate the fidelity between the projected and experimental state, we again find an average fidelity of $(99 \pm 1)\%$. The straight curves are simulations in the same way as for real states, but for these states, we need to consider a smaller residual birefringence of 0.25. It supports the idea that for this measurement set, we have a slightly better polarization compensation. The error bars are predicted in the same way as the real family of states.

3.3 CONCLUSIONS

This fiber-based feed-forward approach using UFOS shows to be a promising technique for single-photon remote state preparation. The main advantage of this technique is the use of just passive polarization optics, and everything is compatible with the telecom technology that is applied around the world for classical communication. Another advantage of our proposal is, as the full implementation uses just commercial devices and standard optics, this technique is not expensive and can be easily implemented outside the research laboratory. We also have shown that our feed-forward operation introduces errors around 1%, being the state-of-the-art for single-photon

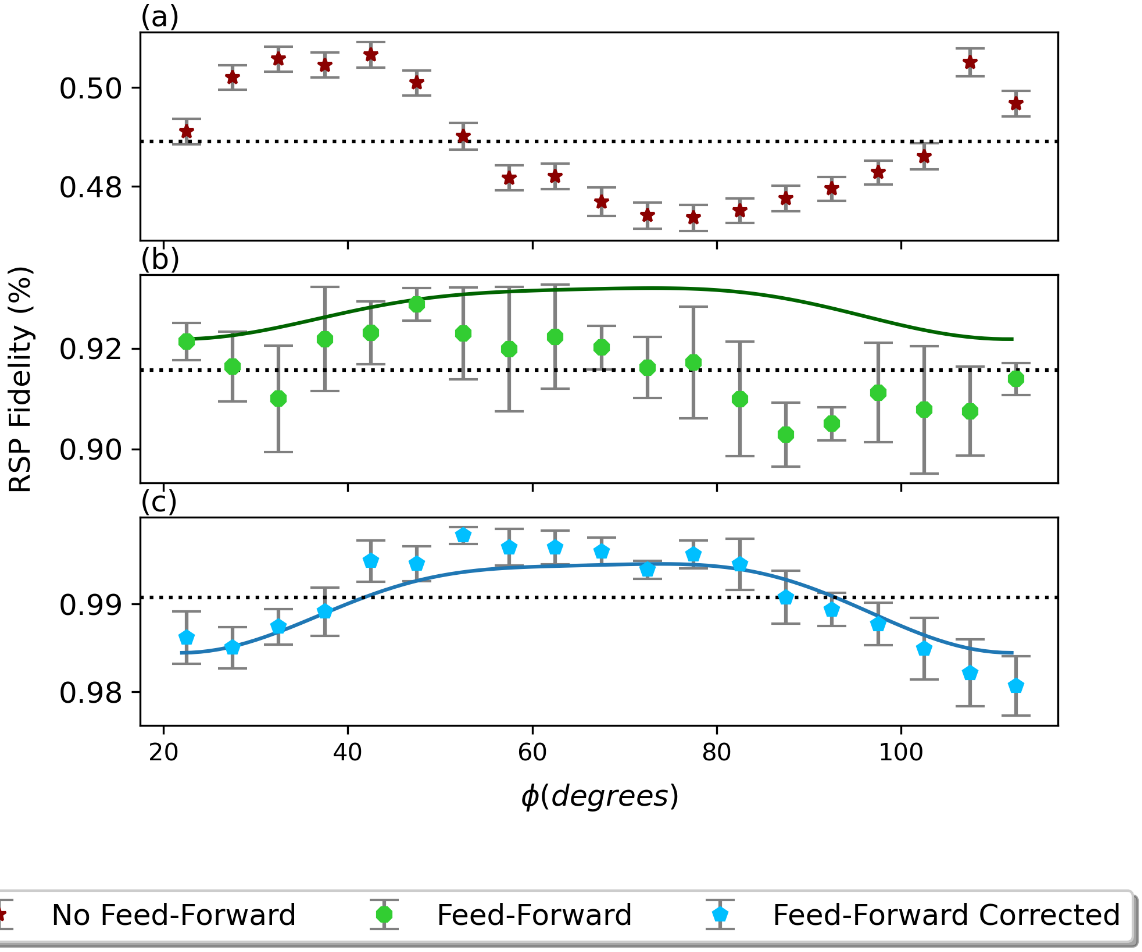

Figure 26 – Here we show the fidelities for no feed-forward (a), fidelities where the feed-forward protocol is on with the theoretical states (b), and the last one is the fidelities between the predicted and the experimental states (c).

remote state preparation using polarization as a degree of freedom.

Even with these promising results, our technique could be improved if we implement faster switches [101] that also have losses below 1 *dB*, which could allow us to go to higher statistics of photons. We could reduce the errors by motorized polarization optics that could increase the precision in setting the waveplate angles for the state preparation, unitary operations, and measurements.

Our method applies to various experiments such as measurement-based quantum computation [94], quantum foundations experiments [102–104], neuromorphic computing [105], photonic simulations in quantum information [106], photon counting [107], and a quantum internet protocol [83]. Another possible application is to implement an indefinite causal order [108] experiment with the UFOS, which is currently being implemented at the University of Vienna in Philip's Walther group. This implementation can be done by connecting the output 2 of UFOS2 at the input2 of UFOS 1, by controlling the UFOS separately we could select which unitary transformation is performed first. Here the main advantage is that the UFOS could allow scaling the experiment in an easier way comparing the free-space interferometer [108].

We obtained these results during the period I was a visitor Ph.D. student (Sandwich) at Philip Walther group, and the results are published in Optics Express [95].

4 PHOTONIC MAXWELL'S DEMON WITH ENHANCED BATHS

Since the first mention of the thought experiment, by J. C. Maxwell [22], to test the limits of the second law of thermodynamics and the nomination as "Maxwell's Demon" by J. Thompson [109], it attracted the interest of the scientific community as it could be the first situation where the validity of the second law was in check. As a result, L. Szilard [110] proposed a pressure Demon to show that the Demon cannot operate outside the limitations of the second law. However, Szilard identified the pillars that constitute what we now know as Maxwell's Demon, measurement, information, and memory. Dealing with binary decisions, he also established the first notion of what we know as a bit today, creating the first connection between information theory and physics.

Nowadays, Maxwell's Demon experiments are related to the amount of information obtained that can be converted into work using feed-forward. For example, in this line of thinking, T. Sagawa and M. Ueda [111] created a modified version of the second law of thermodynamics, including feed-forward, where it shows the maximum work "W" that can be extracted given the information "I" obtained by the Demon:

$$\langle W \rangle \geq \Delta F - k_B T \langle I \rangle , \tag{4.1}$$

where ΔF is the free energy of the system.

Several approaches of Maxwell's Demon experiments were implemented [23–34]. However, we focus on the implementations with light as it is easy to produce different statistics and implement them using the same setup. In the CW regime Araújo *et al.* [20], conducted a study of quantum thermodynamics using optical vortices, where they implemented a Maxwell's Demon, as described in details in section 2.2.3. M. D. Vidrighin *et al.* [35] did a proof-of-principle of an implementation of a photonic Maxwell's Demon experiment, where they send two thermal beams at the same temperature to two photodiodes at opposite polarities which are connected to a capacitor. If the beams are at the same temperature, they will charge and discharge the capacitor creating a zero net charge. However, because thermal-light has bunching statistics, they set two beam-splitters with low reflectivity that provides the information of which beam has more photons for the Demon. With this knowledge, they propose a feed-forward protocol, where they would flip the capacitor to be at the configuration where it is charging, creating a positive voltage that could be stored as energy in a battery and used to implement work in the system later. Despite that, the feed-forward (capacitor flipping) is replaced by a logical operation where they measured the capacitor charge conditionally to the Demon's information (APD outputs). They have shown by data processing the possibility of implementing (proof of principle) a photonic Maxwell's Demon.

Here in this thesis, we present the next step, implementing a photonic Maxwell's Demon with active feed-forward at the single-photon regime using ultra-fast optical switches (UFOS) in a fiber-based setup, where we measured the difference at the photon number between both beams with and without the Demon's information. In this study, we were able to vary several parameters as the expected photon number $\langle n \rangle$, the reflectivity of the directional couplers meaning the different amount of information for the Demon, where we could try explore the parameters for the most efficient Demon in our regime of study. Furthermore, this setup also allows us to implement other photon-number correlations rather than the usual uncorrelated thermal bath, as in the theoretical study by A. Shu *et al.* [112] where they compare the usual Demon with split thermal beam, correlated thermal bath, and anti-correlated thermal bath to determine which would be the most efficient optical Demon.

In the thermal baths with correlations, the Demon's information provides more trustable knowledge about the system comparing thermal states. This fact came from the correlations in the photon number between both paths, as with a perfect state, the Demon's information can tell how many photons we have and make it easier to decide when to switch. It also happens because we work at a low photon regime where the terms with more than two photons are rare enough to be negligible. This extra information also increases the Demon's efficiency as we need fewer photons for a more significant effect.

The results presented here are submitted for publication and are under review. We included the draft in the arXiv [113], under the reference arXiv:2107.09686.

We divide the chapter as follows. The first section describes the analogy between the optical Demon and the usual particles in a box. This section develops the theory in the low photon number that describes our experimental data. We then show the experimental implementation of every thermal bath. In the section results, we provide more experimental details about the measurement sets and the final results of this study. In the last section, we present our conclusions.

4.0.1 Theory

In the original proposal, Maxwell's Demon experiment consists of a box full of particles, where we simplify it by considering they are hot or cold. The box has a wall with a door that divides them. In this door, there is a Demon that knows the temperature of the particles. With this knowledge, the Demon could split the particles leaving the hot ones on one side and the cold ones on another, and by doing that, he could use this temperature difference to extract work. However, in the way the thought experiment is proposed, the Demon expends no energy to obtain the information and sort the particles, so he reduces the system's entropy with no energetic cost. It would be a violation of the 2nd law of thermodynamics. This thought experiment is represented in

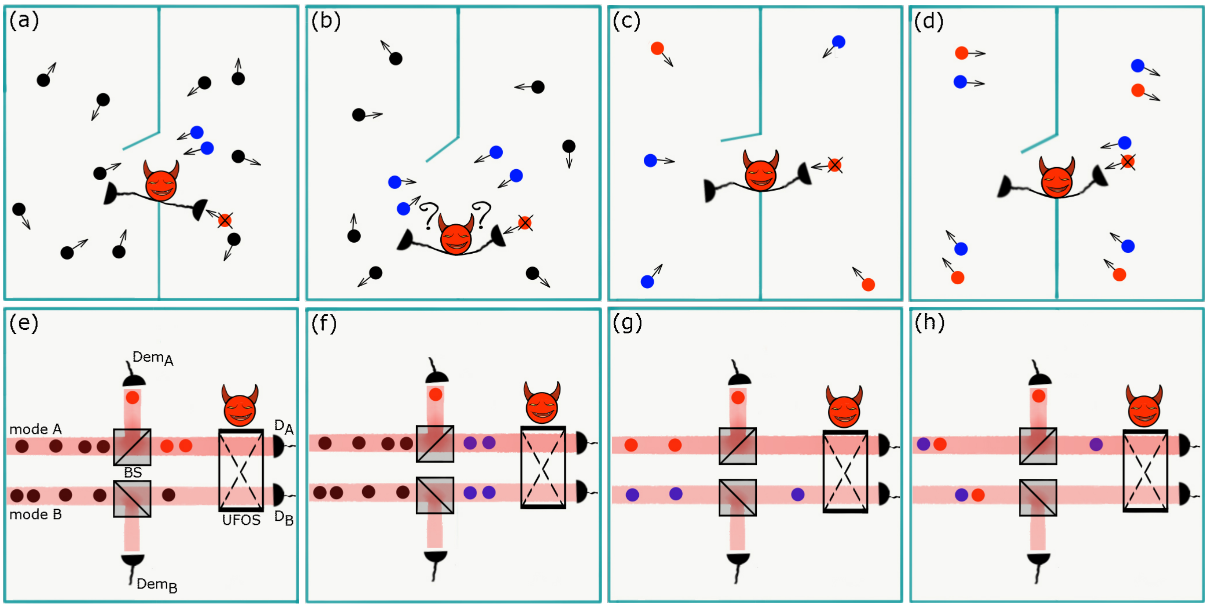

Figure 27 – In this figure, we present the analogy between Maxwell's thought experiment (a) to (d) and its relative photonic version (e) to (h). The lower box is the photonic version for every thermal bath, and the box above represents the particle version of the same bath. In (e), we have two uncorrelated thermal baths, in (f) a split thermal bath, in (g) correlated thermal bath, and in (h) anti-correlated thermal bath. The analogy between the photonic and particle version for every thermal bath is explained in the text.

figure 27 (a). The photonic version, figure 27 (e), consists of two uncorrelated thermal beams where the information for the Demon is provided from a photon subtraction of the modes and the fact that thermal beams have a bunching effect. With the information of his detectors (Dem_A or Dem_B), he decides to switch the direction of the modes ("open the door") to create an imbalance in the particle number between both modes. We can use this imbalance to extract work. In this case, the hot particle is related to the mode with instantaneously higher photon number and the cold one with the lower one.

In the Split thermal bath, we have a thermal state divided into a beam-splitter. It creates correlations in the photon number in both beams, even if the resulting state is still thermal. For the particle case, in figure 27 (b), we perform the following analogy as the Demon's action is useless because the correlations that the split thermal baths share is the same as controlling the door in a wall that has a hole where the particles can pass freely. In (f), the photonic analogy shows that the Demon's action in any of the modes provides the same photon number in both sides [114].

In Figure 27 (c) and (d) it's the situation where the thermal baths have correlations. In both cases, a hot particle is correlated with a cold one. In (c), when the Demon detects a hot (cold) particle going in the direction of the door, he automatically obtains the knowledge that from the other side, a cold (hot) one is coming from the opposite direction. The analogy in (g) represents that the fact if the Demon detects a photon in Dem_A (Dem_B) it signalizes the presence of a photon in the other mode. For the anti-correlated thermal bath (d), the particles, hot and cold, travel in pairs, so if the Demon detects a hot (cold) particle, he knows that the cold (hot) one is going in the same direction. The analogy in (h) is that the Demon's detectors provide information of another particle in the same mode as the relative Demon clicked before. In both cases, by the information about one photon (particle), the Demon has complete information about the bath, making it easier to decide when it switches (open the door) properly.

4.0.1.1 Thermal light

It is well known that thermal light has a bunching behavior, meaning that the photons propagate in groups. We can use this fact to signalize the presence of a thermal beam. To implement it, we can use a beam-splitter in both paths, and its reflectivity a priory it needs to be small. We implement it by setting a single-photon detector to obtain the information of photons in the reflected arm that we refer to as the Demon's information. By comparing the Demon's information in both arms, we can implement the feed-forward to the system, selecting the mode to send to the primary detector using the UFOS. As pointed by M. D. Vidrighin *et al.* [35], flip the capacitor or leave it fixed and flip the modes is equivalent. We choose the second one by implementing it with the UFOS, in a similar way to the single-photon remote state preparation in chapter 3. However, in this work, we focus on measuring the photon number difference between the detectors in path A (D_A) and B (D_B). Here we choose D_A to be the detector where we send the mode with a higher photon number. It means that when the protocol is active, we will have $\Delta N_{AB} = N_A - N_B > 0$.

Another way to see how this idea work is to look at how a photon subtraction in a thermal beam works. To perform this analysis, we start with the density matrix of a thermal state, a mono-frequency state with a frequency ω, on the photon number basis we have:

$$\rho_t = \left(1 - e^{\beta\hbar\omega}\right) \sum_{n=0}^{\infty} |n\rangle \langle n| , \tag{4.2}$$

where β is the inverse of the temperature ($1/k_bT$), the expected photon number $\langle n\rangle$ for the state thermal state is:

$$\langle n\rangle = \frac{1}{exp(\beta\hbar\omega) - 1}. \tag{4.3}$$

We can imagine the situation where we extract a single photon per thermal beam. For this purposes, we use the "one-count" operator, from which we obtain the following state:

$$\rho_{sub} = \frac{a\rho_t a^\dagger}{tr(a\rho_t a^\dagger)} = \frac{a\rho_t a^\dagger}{\langle n\rangle}, \tag{4.4}$$

where a ($a^\dagger$) is the annihilation (creation) operator. After the subtraction, the expected photon number $\langle n_{sub} \rangle$ is:

$$\langle n_{sub} \rangle = \frac{2}{exp(\beta \hbar \omega) - 1} = 2 \langle n \rangle . \tag{4.5}$$

It means the expected photon number is double the initial one after extracting a photon from a thermal beam. It's a counter-intuitive result [115]. We know which beam has more photons by using this information, making it possible to send this mode to the desired detector. For example, if the Demon knows that we have a photon in Dem_A and no photon in Dem_B, he knows that we have $2 \langle n \rangle$ photons in A and $\langle n \rangle$ in B creating a difference in the photon number as $\Delta N_{AB} = \langle n \rangle$. When the Demon detects the opposite situation, the UFOS will switch the modes A and B. In this situation, we flip the photons from mode A and B as $N_A \iff N_B$, meaning that we have $\Delta N_{AB} = \langle n \rangle$. The last case is when we have no clicks or simultaneous clicks between Dem_A and Dem_B, we have on average the same photon number in each beam, meaning a $\Delta N_{AB} = 0$.

For our results, we work in two different regimes. First, we focus on two uncorrelated thermal beams at the same temperature in a higher photon number. This is the regime in which use to show that we have a working photonic Maxwell's Demon. The second regime is the low photon number that we choose a region where we compare uncorrelated, split, correlated, and anti-correlated thermal baths in a similar regime. We need to work on this regime as we produce correlated thermal baths using SPDC and anti-correlated thermal baths by producing NOON states with SPDC states as input, and these states naturally have a low photon number given it is short coherence time ($\approx$ 2 ps). Experimentally we would need high intensities to increase the probability of creating states with more than two photons, which is negligible in our experimental conditions. In the following sub-sections, we describe the theory at the low photon number regime. The theory is consistent with the setup from figure 28. A collaborator developed this theory, and as it is crucial for the data analysis, this text has included it.

4.0.1.1.1 Uncorrelated Thermal Baths

In this sub-section we develop the theory for the low photon number. For this task, first we rewrite the thermal state as:

$$\rho_T = \sum_{n=0}^{\infty} P_n \left| n \right\rangle \left\langle n \right| , \tag{4.6}$$

where

$$P(n) = \frac{\langle n \rangle^n}{(1 + \langle n \rangle)^{n+1}} . \tag{4.7}$$

We can then obtain the probability of detecting m photons by Dem_A and n photons at detector D_A as [116]:

$$P(n,m) = \frac{(n+m)!}{n!m!}\frac{\langle n\rangle^{n+m}}{(1+\langle n\rangle)^{n+m+1}}R^{2n}(1-R^2)^m, \tag{4.8}$$

where R is the reflection amplitude of the beam-splitter, we wrote this in terms of R as it is a parameter to quantify the amount of information available for the Demon.

Here the information for the Demon is provided by inserting a beam splitter in both modes. With the photons detected in the reflected arm, the Demon can decide how to operate. After the beam-splitter, we obtain the following state for mode A:

$$\begin{aligned}\sigma_A = \; & P(0,0)\,|0,0\rangle\langle 0,0|_{\mathrm{Dem}_A,A} + P(1,0)\,|0,1\rangle\langle 0,1|_{\mathrm{Dem}_A,A} + \\ & P(0,1)\,|1,0\rangle\langle 1,0|_{\mathrm{Dem}_A,A} + P(1,1)\,|1,1\rangle\langle 1,1|_{\mathrm{Dem}_A,A} + \dots,\end{aligned} \tag{4.9}$$

where we have cut the terms of higher orders as $P(2,0) << P(1,0)$ in our regime. Here σ_A is the state for the path A. However, the complete state is $\sigma_A \otimes \sigma_B$:

$$\begin{aligned}\sigma_A\otimes\sigma_B = \; & P(0,0)^2\,|0,0,0,0\rangle\langle 0,0,0,0| + P(0,0)P(1,0)\,|0,1,0,0\rangle\langle 0,1,0,0| \\ + \; & P(0,0)P(0,1)\,|0,0,0,1\rangle\langle 0,0,0,1| + P(0,0)P(1,1)\,|0,1,0,1\rangle\langle 0,1,0,1| \\ + \; & P(0,0)P(1,0)\,|1,0,0,0\rangle\langle 1,0,0,0| + P(1,0)^2\,|1,1,0,0\rangle\langle 1,1,0,0| \\ + \; & P(1,0)P(0,1)\,|1,0,0,1\rangle\langle 1,0,0,1| + P(1,0)P(1,1)\,|1,1,0,1\rangle\langle 1,1,0,1| \\ + \; & P(0,1)P(0,0)\,|0,0,1,0\rangle\langle 0,0,1,0| + P(0,1)P(1,0)\,|0,1,1,0\rangle\langle 0,1,1,0| \\ + \; & P(0,1)^2\,|0,0,1,1\rangle\langle 0,0,1,1| + P(0,1)P(1,1)\,|0,1,1,1\rangle\langle 0,1,1,1| \\ + \; & P(1,1)P(0,0)\,|1,0,1,0\rangle\langle 1,0,1,0| + P(1,1)P(1,0)\,|1,1,1,0\rangle\langle 1,1,1,0| \\ + \; & P(1,1)P(0,1)\,|1,0,1,1\rangle\langle 1,0,1,1| + P(1,1)^2\,|1,1,1,1\rangle\langle 1,1,1,1|\,.\end{aligned} \tag{4.10}$$

We re-arranged the terms to use the following notation $|i,j,k,l,m\rangle_{D_A,D_B,Dem_A,Dem_B}$, where we omit the indices for the sake of notation. When the Demon extracts a photon in a thermal state, its expected photon number doubles, meaning that with the knowledge of which Demon's detectors (Dem_A or Dem_B) clicked, we know which is the mode with a higher photon number. By this knowledge, we conclude that if we choose the detector A (D_A) to be the central detector, the switch needs to operate when Dem_B clicks, and then swap the modes as:

$$|m,n,0,1\rangle \rightarrow |n,m,0,1\rangle\,. \tag{4.11}$$

It is essential to mention that since our detectors do not have photon number resolution, we cant distinguish the situations with more than one photon in the same Demon's arm. By implementing the Demon's feed-forward in equation 4.10, we arrive at the final state that describes our system:

$$\begin{aligned}
\rho_{\text{out}} &= P^2(0,0)\left|0000\right\rangle\left\langle 0000\right| + P(0,0)P(0,1)\left|0001\right\rangle\left\langle 0001\right| \\
&+ P(0,0)P(1,0)\left|0100\right\rangle\left\langle 0100\right| + P(0,0)P(1,1)\left|1001\right\rangle\left\langle 1001\right| \\
&+ P(0,1)P(0,0)\left|0010\right\rangle\left\langle 0010\right| + P^2(0,1)\left|0011\right\rangle\left\langle 0011\right| \\
&+ P(0,1)P(1,0)\left|0110\right\rangle\left\langle 0110\right| + P(0,1)P(1,1)\left|0111\right\rangle\left\langle 0111\right| \\
&+ P(1,0)P(0,0)\left|1000\right\rangle\left\langle 1000\right| + P(1,0)P(0,1)\left|0101\right\rangle\left\langle 0101\right| \\
&+ P^2(1,0)\left|1100\right\rangle\left\langle 1100\right| + P(0,1)P(1,1)\left|1101\right\rangle\left\langle 1101\right| \\
&+ P(1,1)P(0,0)\left|1010\right\rangle\left\langle 1010\right| + P(1,1)P(0,1)\left|1011\right\rangle\left\langle 1011\right| \\
&+ P(1,1)P(1,0)\left|1110\right\rangle\left\langle 1110\right| + P^2(1,1)\left|1111\right\rangle\left\langle 1111\right|
\end{aligned} \tag{4.12}$$

In the experimental configuration, we are not able to run it in a single shot. So, let us assume that we run our experiment Γ times, we have the Demon's power as $\Delta N = \Gamma(P_A - P_B)$, where P_A and P_B are probabilities of detecting a photon in its respective modes. Using equation 4.12 we can find P_A and P_B:

$$\begin{aligned}
P_A = \; & 2P(0,0)P(1,1) + 2P(1,0)P(1,1) + P(0,0)P(1,0) + \\
& P(0,1)P(1,1) + P^2(1,0) + P^2(1,1)
\end{aligned} \tag{4.13}$$

$$\begin{aligned}
P_B = \; & P(0,0)P(1,0) + 2P(1,0)P(0,1) + 2P(1,0)P(1,1) + \\
& P(0,1)P(1,1) + P^2(1,0) + P^2(1,1).
\end{aligned} \tag{4.14}$$

From which we obtain ΔN:

$$\begin{aligned}
\Delta N &= (2P(0,0)P(1,1) - 2P(0,1)P(1,0))\Gamma \\
&= \frac{2\left\langle n\right\rangle^2}{(1-\left\langle n\right\rangle)^4} R^2(1-R^2)\Gamma.
\end{aligned} \tag{4.15}$$

The figure of merit that we develop for our work is to normalize ΔN by the total singles rates as $\Delta N/N$ because it is impossible to create precisely the same experimental conditions for all other baths that we discuss during this thesis. We desire to make a fair comparison between all photon statistics. So, we need to normalize by the total photon number in A or B, as they are equal. It allows us to compare all statistics in the same way. In this case, we normalize the Demon's power by the respective total photon number in one of the modes. In the low photon regime, we have a probability P(1) (from equation 4.7) to detect a photon in mode A. After Γ rounds of the experiment, we have:

$$N = \Gamma \frac{\left\langle n\right\rangle}{(1+\left\langle n\right\rangle)}. \tag{4.16}$$

We can then obtain:

$$\frac{\Delta N}{N} = \frac{2\left\langle n\right\rangle}{(1-\left\langle n\right\rangle)^2} R^2(1-R^2), \tag{4.17}$$

where its effects depend on the expected photon number $\langle n \rangle$ of the input beam and the Demon's information, given by the reflectivity R of the beam-splitter, this expression is valid only at the low photon regime.

4.0.1.1.2 Split Thermal Bath

The procedure for a Split thermal bath is essentially the same as Uncorrelated. However, our initial state is a single uncorrelated thermal state in a balanced beam-splitter, where it essentially divides the beam. Thus, the state in modes A and B is:

$$\rho_{\text{split}} = \sum_{n,m=0}^{\infty} P(n,m) \left| n,m \right\rangle \left\langle n,m \right|_{A,B}, \tag{4.18}$$

where $P(n,m)$ is the probability defined in equation 4.8, with $R = 1/\sqrt{2}$.

Considering the terms up to two-photon we obtain:

$$\begin{aligned} \rho_{\text{split}} &\approx P(0,0) \left|0,0\right\rangle \left\langle 0,0\right|_{A,B} + P(0,1) \left|0,1\right\rangle \left\langle 0,1\right|_{A,B} \\ &+ P(1,0) \left|1,0\right\rangle \left\langle 1,0\right|_{A,B} + P(2,0) \left|2,0\right\rangle \left\langle 2,0\right|_{A,B} \\ &+ P(0,2) \left|0,2\right\rangle \left\langle 0,2\right|_{A,B} + P(1,1) \left|1,1\right\rangle \left\langle 1,1\right|_{A,B}, \end{aligned} \tag{4.19}$$

where we already considered the fact that for $R = 1/\sqrt{2}$ $P(n,m)$ is symmetric. We need to add the beam-splitter transformation. Let us perform the analysis term by term as:

$$\begin{aligned} \left|0,1\right\rangle \left\langle 0,1\right|_{A,B} &\rightarrow (1-R^2) \left|0100\right\rangle \left\langle 0100\right|_{A,B,\text{Dem}_A,\text{Dem}_B} \\ &\quad +R^2 \left|0001\right\rangle \left\langle 0001\right|_{A,B,\text{Dem}_A,\text{Dem}_B} \\ \left|1,0\right\rangle \left\langle 1,0\right|_{A,B} &\rightarrow (1-R^2) \left|1000\right\rangle \left\langle 1000\right|_{A,B,\text{Dem}_A,\text{Dem}_B} \\ &\quad +R^2 \left|0010\right\rangle \left\langle 0010\right|_{A,B,\text{Dem}_A,\text{Dem}_B} \\ \left|1,1\right\rangle \left\langle 1,1\right|_{A,B} &\rightarrow (1-R^2)^2 \left|1100\right\rangle \left\langle 1100\right|_{A,B,\text{Dem}_A,\text{Dem}_B} \\ &\quad +R^2(1-R^2) \left|1001\right\rangle \left\langle 1001\right|_{A,B,\text{Dem}_A,\text{Dem}_B} \\ &\quad +R^2(1-R^2) \left|0110\right\rangle \left\langle 0110\right|_{A,B,\text{Dem}_A,\text{Dem}_B} \\ &\quad +R^4 \left|0011\right\rangle \left\langle 0011\right|_{A,B,\text{Dem}_A,\text{Dem}_B} \\ \left|0,2\right\rangle \left\langle 0,2\right|_{A,B} &\rightarrow (1-R^2)^2 \left|0200\right\rangle \left\langle 0200\right|_{A,B,\text{Dem}_A,\text{Dem}_B} \\ &\quad +2R^2(1-R^2) \left|0101\right\rangle \left\langle 0101\right|_{A,B,\text{Dem}_A,\text{Dem}_B} \\ &\quad +R^4 \left|0002\right\rangle \left\langle 0002\right|_{A,B,\text{Dem}_A,\text{Dem}_B} \\ \left|2,0\right\rangle \left\langle 2,0\right|_{A,B} &\rightarrow (1-R^2)^2 \left|2000\right\rangle \left\langle 2000\right|_{A,B,\text{Dem}_A,\text{Dem}_B} \\ &\quad +2R^2(1-R^2) \left|1010\right\rangle \left\langle 1010\right|_{A,B,\text{Dem}_A,\text{Dem}_B} \\ &\quad +R^4 \left|0020\right\rangle \left\langle 0020\right|_{A,B,\text{Dem}_A,\text{Dem}_B}. \end{aligned} \tag{4.20}$$

The notation is simplified, omitting the labels. We can then apply the feed-forward as in equation 4.11 and obtain the final state:

$$\begin{aligned}
\rho_{\text{out}} &= P(0,0)\,|0000\rangle\langle 0000| + P(0,1)\Big[(1-R^2)(|0100\rangle\langle 0100| + |1000\rangle\langle 1000|) \\
&+ R^2(|0001\rangle\langle 0001| + |0010\rangle\langle 0010|)\Big] + P(1,1)\Big[(1-R^2)^2\,|1100\rangle\langle 1100| \\
&+ R^2(1-R^2)(|0101\rangle\langle 0101| + |0110\rangle\langle 0110|) + R^4\,|0011\rangle\langle 0011|\Big] \\
&+ P(0,2)\Big[(1-R^2)^2(|2000\rangle\langle 2000| + |0200\rangle\langle 0200|) \\
&+ R^4(|0020\rangle\langle 0020| + |0002\rangle\langle 0002|) \\
&+ 2R^2(1-R^2)(|1010\rangle\langle 1010| + |1001\rangle\langle 1001|)\Big]. \qquad (4.21)
\end{aligned}$$

The probabilities P_A and P_B are:

$$\begin{aligned}
P_A &= P(0,1)(1-R^2) + P(1,1)(1-R^2)^2 \qquad (4.22)\\
&\quad + P(0,2)(1-R^2)^2 + 4P(0,2)R^2(1-R^2) \\
P_B &= P(0,1)(1-R^2) + P(1,1)(1-R^2)^2 \\
&\quad + P(0,2)(1-R^2)^2 + 2P(1,1)R^2(1-R^2),
\end{aligned}$$

from which we obtain ΔN:

$$\Delta N = \Gamma(P_A - P_B) = 2\Gamma R^2(1-R^2)(2P(0,2) - P(1,1)) = 0.$$

Hence,

$$\frac{\Delta N}{N} = 0 \qquad (4.23)$$

for all reflectivities. It is important to mention that in ref [112] they have shown that it is zero even for higher $\langle n\rangle$. This configuration is similar to the one where Katamadze *et al.* [114] used to show that the effect known as "quantum vampire", is in reality, a classical effect based on photon-number correlations. In their setup, they produce A thermal beam and send it to a balanced beam-splitter. Then, they extract a photon from one of the arms, and by Homodyne detection, reconstruct the photon number distributions from each arm separately. By doing that, they conclude that the resulting state was the same for the arm that they have extracted a photon and the untouched one. In our case, we can also explain that because both beams have photon-number correlations, extract a photon does not provide any valuable information for the Demon to feed the system and extract work, meaning that we have the same photon number in both arms of the experiment even if we extract a photon or not. It means that if the Demon acts, he switches beams with the same photon number all the time.

4.0.1.2 Thermal Baths with Correlations

In this section, We discuss the theory for the thermal baths with correlations. In this case, we need quantum states to produce the thermal baths. However, the correlations that we explore in the experiment are classical ones. With this in mind, we want to investigate if these correlations can provide better information helping the Demon to make better decisions about when he needs to switch. We explore thermal baths with correlations that we implement using an SPDC state and thermal baths with anti-correlations that we can implement using a two-photon NOON state. We focus on developing the figure of merit $\Delta N/N$ for our states in the following subsections. However, here we have an extra ingredient to take into account, the classical correlations. We then develop a second figure of merit where we normalize the Demon's effect by the correlations of the baths $\Delta N/C$. It is essential to mention that for SPDC when doing the partial trace in one of the photons, the other it is in a thermal state [117, 118]. For the NOON state, a theoretical approach [112] used a state where it is a perfect NOON state for every desired N-Photons, and by doing the partial trace, it is thermal. However, experimentally we are not able to perform the same state. Our state is close and results in a superposition of a two-photon NOON state [119, 120], where we generate it by a Hong-Ou-Mandel (HOM) interference between the photons from the SPDC.

4.0.1.2.1 Correlated Thermal Bath

The general state for the SPDC is:

$$|\psi\rangle = \frac{1}{\cosh s}\sum_{n=0}^{\infty}(\tanh s)^n\,|n,n\rangle_{A,B}\,, \tag{4.24}$$

as we are in the low photon regime, we are only considering the terms up to two-photon, as:

$$|\psi\rangle \approx \frac{1}{1-\frac{s^2}{2}}\,|0,0\rangle_{A,B} + \frac{s}{1-\frac{s^2}{2}}\,|1,1\rangle_{A,B}\,, \tag{4.25}$$

where s is the squeezing parameter. However, at equation 4.25 we are considering a perfect source where we have just the pairs. Here we need to consider the losses that degrade the correlations. The losses are related to the source efficiency, optical fibers coupling, and everything that can affect our system. We can model the loss as a beam-splitter where the lost photons are "reflected" outside our experiment. We implement the following transformation:

$$|1\rangle_A \rightarrow \epsilon\,|1,0\rangle_{A,l_A} + \sqrt{1-\epsilon^2}\,|0,1\rangle_{A,l_A}\,. \tag{4.26}$$

It means that the photon has a probability ϵ^2 to remain in the desired mode. Considering that the error is symmetric for modes A and B, we obtain the following state:

$$\begin{aligned}|\psi\rangle \;\approx\;& \frac{1+s(1-\epsilon^2)}{1-\frac{s^2}{2}}\,|0,0,0,0\rangle_{A,B,l_A,l_B} + \frac{s\epsilon\sqrt{1-\epsilon^2}}{1-\frac{s^2}{2}}(|1,0,0,1\rangle_{A,B,l_A,l_B}\\ &+|0,1,1,0\rangle_{A,B,l_A,l_B}) + \frac{s\epsilon^2}{1-\frac{s^2}{2}}\,|1,1,0,0\rangle_{A,B,l_A,l_B}\,.\end{aligned} \tag{4.27}$$

We need to apply the Demon's beam-splitter as $|1,0\rangle \rightarrow= \sqrt{1-R^2}\,|1,0\rangle_{A,Dem_A} + R\,|0,1\rangle_{A,Dem_A}$ for modes A and B, respectively. We then obtain:

$$\begin{aligned}
|\psi\rangle \approx\ & \frac{1+s(1-\epsilon^2)}{1-\frac{s^2}{2}}\,|0,0,0,0,0,0\rangle \\
& + \frac{s\epsilon\sqrt{1-\epsilon^2}}{1-\frac{s^2}{2}} R\,(|0,0,1,0,0,1\rangle + |0,0,0,1,1,0\rangle) \\
& + \frac{s\epsilon\sqrt{1-\epsilon^2}}{1-\frac{s^2}{2}} \sqrt{1-R^2}\,(|1,0,0,0,0,1\rangle + |0,1,0,0,1,0\rangle) \\
& + \frac{s\epsilon^2}{1-\frac{s^2}{2}} R\sqrt{1-R^2}\,(|0,1,1,0,0,0\rangle + |1,0,0,1,0,0\rangle) \\
& + \frac{s\epsilon^2}{1-\frac{s^2}{2}} \Big((1-R^2)\,|1,1,0,0,0,0\rangle + R^2\,|0,0,1,1,0,0\rangle\Big), \qquad (4.28)
\end{aligned}$$

We are using the following notation $|i,j,k,l,m,n\rangle_{A,B,Dem_A,Dem_B,l_A,l_B}$ that we are not showing to simplify the visualization. The next step is to implement the Demon's feed-forward, which is different comparing the thermal states without correlations. If we analyze the equation 4.28, we can see that when the Demon Dem_A or Dem_B clicks, it provide the information that the other mode has a photon. This is the power of using the correlations, just detecting the photon from one mode allows the Demon to acquire a complete knowledge of both modes allowing him to feed the system with the right decision. The algorithm for a correlated thermal bath is the following:

$$|i,j,1,0,0,0\rangle \rightarrow |j,i,1,0,0,0\rangle\,. \qquad (4.29)$$

We then obtain the final state for correlated thermal baths:

$$\begin{aligned}
|\psi\rangle \approx\ & \Bigg(\frac{1+s(1-\epsilon^2)}{1-\frac{s^2}{2}}\,|0,0,0,0,0,0\rangle + \qquad (4.30) \\
& \frac{s\epsilon\sqrt{1-\epsilon^2}}{1-\frac{s^2}{2}} R\,(|0,0,1,0,0,1\rangle + |0,0,0,1,1,0\rangle) + \\
& \frac{s\epsilon\sqrt{1-\epsilon^2}}{1-\frac{s^2}{2}} \sqrt{1-R^2}\,(|1,0,0,0,0,1\rangle + |0,1,0,0,1,0\rangle) + \\
& \frac{s\epsilon^2}{1-\frac{s^2}{2}} R\sqrt{1-R^2}\,(|1,0,1,0,0,0\rangle + |1,0,0,1,0,0\rangle) + \\
& \frac{s\epsilon^2}{1-\frac{s^2}{2}} \Big((1-R^2)\,|1,1,0,0,0,0\rangle + R^2\,|0,0,1,1,0,0\rangle\Big)\Bigg).
\end{aligned}$$

We are able now to calculate the probabilities for the detectors D_A and D_B to click as:

$$\begin{aligned}
P_A &= \frac{s^2}{(1-\frac{s^2}{2})^2}\Big(\epsilon^2(1-\epsilon^2)(1-R^2)+\epsilon^4(1-R^2)^2+ \\
&\quad 2\epsilon^4R^2(1-R^2)\Big) \\
P_B &= \frac{s^2}{(1-\frac{s^2}{2})^2}\Big(\epsilon^2(1-\epsilon^2)(1-R^2)+\epsilon^4(1-R^2)^2\Big).
\end{aligned} \tag{4.31}$$

From which we can calculate ΔN:

$$\Delta N = \Gamma(P_A - P_B) = \Gamma\frac{s^2}{(1-\frac{s^2}{2})^2}2\epsilon^4R^2(1-R^2). \tag{4.32}$$

Here we can calculate N, as the chance of detector A or B to click after Γ repetitions of the experiment, and the coincidence rate as $C = \Gamma P_{AB}$, from equation 4.27. We have then:

$$\begin{aligned}
N &= \Gamma P_A = \Gamma\frac{s^2}{(1-\frac{s^2}{2})^2}\epsilon^2 \\
C &= \Gamma P_{AB} = \Gamma\frac{s^2}{(1-\frac{s^2}{2})^2}\epsilon^4.
\end{aligned} \tag{4.33}$$

With equations 4.32 and 4.33 we can calculate the figure of merits of our comparison. First is the ΔN normalized by the singles rate, which considers the total photon number, efficiency of the source, and every other experimental error that reduces the number of pairs. However, it is a good way to compare uncorrelated and split thermal baths as they do not have this correlation. The second figure of merit is related to the classical correlations that are an extra ingredient here. In this regime, we can normalize ΔN by the coincidence rate quantifying the correlations, even if they are classical. We obtain then:

$$\frac{\Delta N}{N} = 2\epsilon^2R^2(1-R^2), \tag{4.34}$$

and

$$\frac{\Delta N}{C} = 2R^2(1-R^2). \tag{4.35}$$

Here there are two important points that we need to pay attention to. First, in the low photon number, the Demon's effect for correlated thermal baths have no dependence on the expected photon number $\langle n\rangle$, differently from thermal states. It depends just on how much information is available for the Demon by setting the reflectivity rate. The second important point is that when we normalize by the correlations, the therm that represents the efficiency of the source and errors is not present anymore. Just by comparing equations 4.34 and 4.35 we can conclude that the correlations provide a higher effect for the Demon's action, as $0 \leq \epsilon \leq 1$, and $\Delta N/C$ is the case for just perfect pairs, with $\epsilon^2 = 1$ in $\Delta N/N$.

4.0.1.2.2 Anti-correlated Thermal Bath

This section develops the figure of merit $\Delta N/N$ and $\Delta N/C$ for thermal baths with anti-correlations. The way of producing such thermal baths is by using a two-photon NOON state. These states are produced by a HOM interference using an SPDC state as input. The resulting state for two-photon is:

$$|\psi\rangle \;=\; \frac{1}{1-\frac{s^2}{2}}\,|0,0\rangle_{A,B}+\frac{s}{1-\frac{s^2}{2}}\left(\frac{v}{\sqrt{2}}(|2,0\rangle_{A,B}+|0,2\rangle_{A,B})+\sqrt{1-v^2}\,|1,1\rangle_{A,B}\right), \tag{4.36}$$

where s the squeezing parameter and ν^2 is the visibility of the source that modulates the probability of the photon pairs bunch to a NOON state. The protocol is similar to the previous one, where we need first to modulate the losses at the source as:

$$\begin{aligned}|1,0\rangle \;&\rightarrow\; \epsilon\,|1,0\rangle_{A,l_A}+\sqrt{1-\epsilon^2}\,|0,1\rangle_{A,l_A}\\ |2,0\rangle \;&\rightarrow\; \epsilon^2\,|2,0\rangle_{A,l_A}+\sqrt{2}\epsilon\sqrt{1-\epsilon^2}\,|1,1\rangle_{A,l_A}+(1-\epsilon^2)\,|0,2\rangle_{A,l_A}\,.\end{aligned} \tag{4.37}$$

The resulting state is:

$$\begin{aligned}|\psi\rangle \;=\;& \frac{1}{1-\frac{s^2}{2}}\,|0,0,0,0\rangle+\frac{s}{1-\frac{s^2}{2}}\left\{\frac{\nu}{\sqrt{2}}\left[\epsilon^2(|2,0,0,0\rangle+|0,2,0,0\rangle)\right.\right.\\ &\left.+\sqrt{2}\epsilon\sqrt{(1-\epsilon^2}(|1,0,1,0\rangle+|0,1,0,1\rangle)+(1-\epsilon^2)(|0,0,2,0\rangle+|0,0,0,2\rangle)\right]\\ &+\sqrt{1-\nu^2}\left[\epsilon^2\,|1,1,0,0\rangle+\epsilon\sqrt{1-\epsilon^2}(|0,1,1,0\rangle+|1,0,0,1\rangle)\right.\\ &\left.\left.+(1-\epsilon^2)\,|0,0,1,1\rangle\right]\right\},\end{aligned} \tag{4.38}$$

where the notation is $|i,j,k,l\rangle_{A,B,l_A,l_B}$. The Demon's Beam splitter is applied according to:

$$\begin{aligned}|1,0\rangle \;&\rightarrow\; \sqrt{1-R^2}\,|1,0\rangle_{A,Dem_A}+R\,|0,1\rangle_{A,Dem_A}\\ |2,0\rangle \;&\rightarrow\; (1-R^2)\,|2,0\rangle_{A,Dem_A}+\sqrt{2}R(1-R^2)\,|1,1\rangle_{A,Dem_A}+R^2\,|0,2\rangle_{A,Dem_A}\,.\end{aligned} \tag{4.39}$$

The state after the beam-splitter action is:

$$
\begin{aligned}
|\psi\rangle \;=\; & \frac{1}{1-\frac{s^2}{2}}\,|0,0,0,0,0,0\rangle \\
& + \frac{s}{1-\frac{s^2}{2}}\left\{\frac{\nu}{\sqrt{2}}\left[\epsilon^2\left((1-R^2)(|2,0,0,0,0,0\rangle+|0,2,0,0,0,0\rangle)\right.\right.\right. \\
& +\sqrt{2}R\sqrt{1-R^2}(|1,0,1,0,0,0\rangle+|0,1,0,1,0,0\rangle) \\
& \left. + R^2(|0,0,2,0,0,0\rangle+|0,0,0,2,0,0\rangle)\right) \\
& +\sqrt{2}\epsilon\sqrt{1-\epsilon^2}\left(\sqrt{1-R^2}(|1,0,0,0,1,0\rangle+|0,1,0,0,0,1\rangle)\right. \\
& \left. +R(|0,0,1,0,1,0\rangle+|0,0,0,1,0,1\rangle)\right) \\
& \left. + \epsilon\sqrt{1-\epsilon^2}(|0,0,0,0,2,0\rangle+|0,0,0,0,0,2\rangle)\right] \\
& +\sqrt{1-\nu^2}\left[\epsilon^2\left((1-R^2)\,|1,1,0,0,0,0\rangle+R^2\,|0,0,1,1,0,0\rangle\right.\right. \\
& \left. + \sqrt{R}\sqrt{1-R^2}(|1,0,0,1,0,0\rangle+|0,1,1,0,0,0\rangle)\right) \\
& +\epsilon\sqrt{1-\epsilon^2}\left(\sqrt{1-R^2}(|0,1,0,0,1,0\rangle+|1,0,0,0,0,1\rangle)\right. \\
& \left.\left.\left. +R(|0,0,0,1,1,0\rangle+|0,0,1,0,0,1\rangle)\right)+(1-\epsilon^2)\,|0,0,0,0,1,1\rangle\right]\right\}, \qquad (4.40)
\end{aligned}
$$

where $|i,j,k,l,m,n\rangle_{A,B,Dem_A,Dem_B,I_A,I_B}$.

The last step is to include the Demon's action. For the NOON state, the clicks on Dem_A and Dem_B provide a complete description of the photon number in both modes. However, a click in A (B) tells the Demon that the mode with more photons is A (B). In this case, the switch occurs when Dem_B clicks as:

$$
\begin{aligned}
|i,j,0,1,x,y\rangle &\rightarrow |j,i,0,1,x,y\rangle \\
|i,j,0,2,x,y\rangle &\rightarrow |j,i,0,2,x,y\rangle\,. \qquad (4.41)
\end{aligned}
$$

Here we include the terms where more than one photon is detected, as our detectors have no photon resolution. Thus, including the Demon's action, the final state for anti-correlated thermal baths is:

$$
\begin{aligned}
|\psi\rangle \;=\; & \frac{1}{1-\frac{s^2}{2}}\,|0,0,0,0,0,0\rangle \\
& +\frac{s}{1-\frac{s^2}{2}}\left\{\frac{\nu}{\sqrt{2}}\left[\epsilon^2\left((1-R^2)(|2,0,0,0,0,0\rangle+|0,2,0,0,0,0\rangle)\right.\right.\right. \\
& +\sqrt{2}R\sqrt{1-R^2}(|1,0,1,0,0,0\rangle+|1,0,0,1,0,0\rangle) \\
& \left.+\,R^2(|0,0,2,0,0,0\rangle+|0,0,0,2,0,0\rangle)\right) \\
& +\sqrt{2}\epsilon\sqrt{1-\epsilon^2}\left(\sqrt{1-R^2}(|1,0,0,0,1,0\rangle+|0,1,0,0,0,1\rangle)\right. \\
& \left.+R(|0,0,1,0,1,0\rangle+|0,0,0,1,0,1\rangle)\right) \\
& \left.+\,\epsilon\sqrt{1-\epsilon^2}(|0,0,0,0,2,0\rangle+|0,0,0,0,0,2\rangle)\right] \\
& +\sqrt{1-\nu^2}\left[\epsilon^2\left((1-R^2)\,|1,1,0,0,0,0\rangle+R^2\,|0,0,1,1,0,0\rangle\right.\right. \\
& \left.+\,\sqrt{R}\sqrt{1-R^2}(|0,1,0,1,0,0\rangle+|0,1,1,0,0,0\rangle)\right) \\
& +\epsilon\sqrt{1-\epsilon^2}\left(\sqrt{1-R^2}(|0,1,0,0,1,0\rangle+|1,0,0,0,0,1\rangle)\right. \\
& \left.\left.\left.+R(|0,0,0,1,1,0\rangle+|0,0,1,0,0,1\rangle)\right)+(1-\epsilon^2)\,|0,0,0,0,1,1\rangle\,\right]\right\}. \qquad (4.42)
\end{aligned}
$$

The resulting probabilities are:

$$
\begin{aligned}
P_A \;=\; & \frac{s^2}{(1-\frac{s^2}{2})^2}\left\{\frac{\nu^2}{2}\left[\epsilon^4(1-R^2)^2+4\epsilon^4R^2(1-R^2)+2\epsilon^2(1-\epsilon^2)(1-R^2)\right]\right. \\
& \left.+(1-\nu^2)\left[\epsilon^4(1-R^2)^2+\epsilon^2(1-\epsilon^2)(1-R^2)\right]\right\} \\
P_B \;=\; & \frac{s^2}{(1-\frac{s^2}{2})^2}\left\{\frac{\nu^2}{2}\left[\epsilon^4(1-R^2)^2+2\epsilon^2(1-\epsilon^2)(1-R^2)\right]\right. \\
& \left.+(1-\nu^2)\left[\epsilon^4(1-R^2)^2+2\epsilon^4R^2(1-R^2)+\epsilon^2(1-\epsilon^2)(1-R^2)\right]\right\}. \qquad (4.43)
\end{aligned}
$$

The difference in the photon number after Γ rounds of the experiment is:

$$
\Delta N=\Gamma(P_A-P_B)=\Gamma\frac{s^2}{(1-\frac{s^2}{2})^2}2(2\nu^2-1)\epsilon^4R^2(1-R^2). \qquad (4.44)
$$

With equations 4.44 and 4.33 we obtain the Demon's power normalized by the singles and coincidences as:

$$
\frac{\Delta N}{N}=2\epsilon^2(2v^2-1)R^2(1-R^2) \qquad (4.45)
$$

and

$$
\frac{\Delta N}{C}=2(2v^2-1)R^2(1-R^2). \qquad (4.46)
$$

In comparison with correlated-thermal baths, here we have the extra therm related to the visibility of the HOM interferometer. This term is related to the probability of the photons bunch at the beam-splitter. In a theoretical approach for higher $\langle n \rangle$ [112], the anti-correlated baths overpass the efficiency of the correlated ones. Nevertheless, here in our regime, with perfect visibility, they would have precisely the same efficiency. Another point is that our figure of merits depends just on the source efficiency, visibility of the source, and the reflectivity of the Demon, in the opposite way of uncorrelated thermal baths that has a dependence on the temperature ($\langle n \rangle$).

4.1 EXPERIMENTAL IMPLEMENTATION

In this section, we present the setup and the protocol of our photonic Maxwell's Demon. First, we describe the experimental implementation and the generation of each thermal bath. Then, in figure 28 (a) to (c), we show the sources that generate the baths, and in (d) is the setup for the protocol.

The protocol is the following: we first couple the thermal baths to single-mode optical fibers and connect them to one of the ports of the tunable directional couplers (TDC). The TDC is a device that acts as a beam-splitter where we can set the desired reflectivity. In each mode, one output of the TDC is connected to the fiber-delay that represents the central part of the setup, and the second one goes directly to the Demon's detectors, named Dem_A or Dem_B. The fiber delay is necessary as the electronics require some time between the Demon's click, the pulse generation, and the time for UFOS to switch, and here we set it as 162 m. It is more than necessary, but it makes it easier to synchronize everything as we can delay the pulse that controls the UFOS electronically. After the delay, the fibers from each mode are connected to the UFOS inputs and the outputs to the detectors D_A and D_B. All detectors that we use in this experiment are superconducting nanowire single-photon detectors (SNSPD) from PhotonSpot Inc, with a detection efficiency of $\approx 95\%$ for 1550 nm.

The TTM evaluates the logic of the Demon as in chapter 3. When the right Demon's detector click, we send the pulse for the switch. The logic in the TTM cannot discriminate if we are in the situation where both Demon's detectors click. Nevertheless, this case is negligible in our statistics, and this is not a problem as the temperatures are balanced for the switching configuration. However, the optimal switching time is related to the coherence time of the thermal beams, which is $\approx 5\mu s$, but by the technical limitations of our TTM we are limited at $2.5\mu s$. It means that we could be cutting our beam.

The UFOS have unbalanced losses between the input/outputs. To compensate for this problem, we perform three measurements in our protocol. In the first one, we force the switch to be constantly in the cross configuration. In this configuration we set the temperature of the beams making then balanced as possible to have ΔN_{cross} =

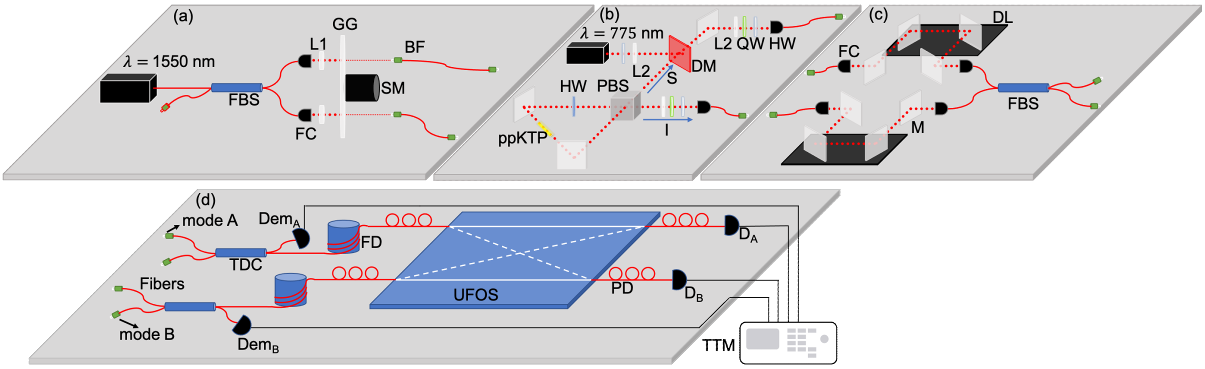

FBS - Fiber beam-splitter, L – Lens, GG – Ground glass, BF – Bare fiber, FC – Fiber-coupler
SM – Step motor , HW – Half-wave plate, QW – Quarter-wave plate, DM – Dicroic Mirror , M – Mirror
PBS – Polarizing beam splitter, ppKTP - Periodically Poled KTP, DL – Delay line, PD – Paddle
TDC – Tunable directional couplers, FD – Fiber delay, UFOS – Ultrafast optical switch, TTM – Time tag module

Figure 28 – Figures (a) to (c) are the setup to generate the thermal baths. In (a) we generate the uncorrelated thermal baths, where each thermal beam is produced on a different spot at the ground glass, (b) the correlated thermal baths using an SPDC source, and in (c) we produce the anti-correlated thermal baths by using an SPDC source (setup (b)) as input in a HOM interferometer to produce a NOON state. Figure (d) is the setup for the photonic Maxwell's Demon. Better details of the functioning of the setups are provided in the text.

$N_A - N_B \to 0$, where N_A (N_B) is the counts at D_A (D_B) in one second. We choose this configuration to set the temperature because the UFOS switches with the Demon's signal, preventing us from creating any imbalanced by wrong switching. Choosing this configuration to balance the temperatures prevents us from creating an imbalance when both Demon's detectors click simultaneously, as, in this situation, the photon number is balanced. We then turn the UFOS ON without sending any signal. In this case, the UFOS will remain in the bar configuration. This measurement $\Delta N_{bar} = N_A - N_B$ will help us to evaluate which is the natural unbalance in between the counts because of the asymmetric losses. The last measurement is with the feed-forward protocol on $\Delta N_{FF} = N_A - N_B$, from which we can calculate the unnormalized Demon's power as:

$$\Delta N_{exp} = \Delta N_{FF} - \Delta N_{bar}. \tag{4.47}$$

4.1.1 Uncorrelated Thermal Baths

The first studies with thermal sources with stronger intensities started in the 60's [121–123] where they shine different light sources at spinning ground glass, the technique became knows as the Arecchi wheel, to produce monochromatic beams with thermal statistics, know as pseudo-thermal light. This name was given as this beam is monochromatic, opposite to thermal radiation with a distribution over the frequencies. The methodology utilized to characterize the thermal beams is the Hanbury Brown and Twiss (HTB) interferometer [124] that allows the measurement of the second-order

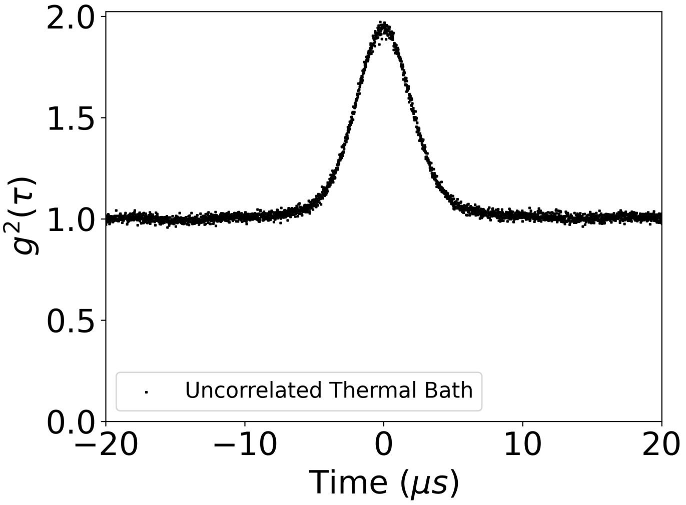

Figure 29 – Measurement of the $g^2(\tau)$ of our thermal light source with $g^2(0) \approx 1.95$ and a coherence time of of $\tau_c \approx 5.42$ μs.

correlation $g^2(\tau)$ of a light source. It consists of dividing the beam in two by a balanced beam-splitter and vary the path size in one of the beams to measure the correlations between them. For thermal light is know that $g^2(0) = 2$.

We wish to produce thermal light in our experiment with λ =1550 *nm*, as the UFOS are designed to work in this wavelength. For this purpose, we use the setup as in figure 28 (a) where we connect a CW laser to a fiber-based beam-splitter to divide the beam equally, where each output is collimated and focused at different spots in the ground glass by a 75 *mm* lens. The ground glass has 220 grit/size, and it rotates with 20 *Hz*. We then collect the light with two single-mode Sm-28 fibers at 225 *mm* of the disk. It is important to mention that we collect the thermal light directly at the fibers connectors without fiber couplers. It was important for a high $g^2(\tau)$. Using the HTB interferometer, we perform the measurements of the $g^2(\tau)$ as in figure 29. After several repetitions, we obtained a $g^2(0) \approx 1.95$ and by assuming a Gaussian thermal beam of a form:

$$g^2(\tau) = 1 + e^{-\pi(\frac{\tau}{\tau_c})^2} \tag{4.48}$$

we find a coherence time of $\tau_c \approx 5.42$ μs.

4.1.2 Split Thermal Baths

For split thermal baths, the procedure is even more straightforward. As the implementation of two uncorrelated thermal beams was already done, we can take one of the beams and connect it to a balanced fiber-based beam-splitter where each output is connected to one mode in the setup of figure 28 (d). We characterized this light source to verify if it loses the thermal characteristics after the beam is divided. Figure 30 shows that the beam still has a high $g^2(\tau)$, showing that the thermal statistics are not affected in the same way as the baths with correlations. Another reason to characterize this

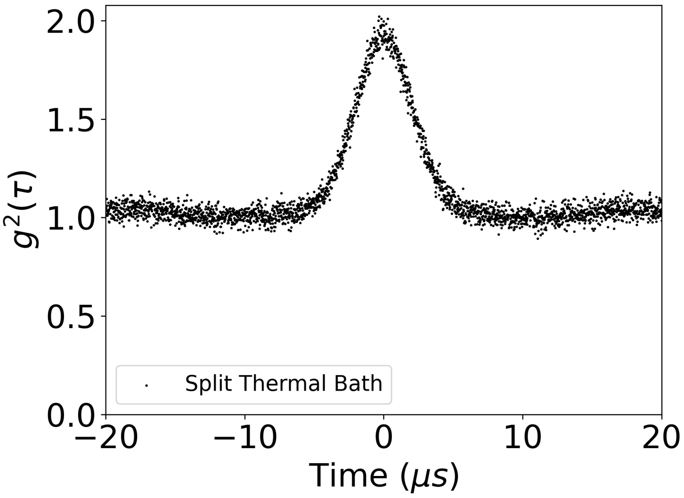

Figure 30 – Measurement of the $g^2(\tau)$ of for a split thermal beam.

source is that we want to guarantee that $\Delta N = 0$ is not because of the degradation of the light source after it's division, but because of the correlations between the modes.

4.1.3 Correlated Thermal Baths

An SPDC source produces correlated thermal baths as in figure 28 (b). It consist in a CW laser with $\lambda = 775$ *nm* that is focused, using a a less (L2) with f=400 *nm*, into a ppKTP Crystal inside a polarization-based Sagnac interferometer [125]. This is the same source described in section 3.2, and it generates a singlet state $|\Psi^-\rangle$ with $\lambda = 1550$ *nm*. However, here we are just using the classical correlations, neglecting the polarization of the photons. Here we sent the signal/idler to modes A/B to use the correlations in the photon number as a resource for the Demon.

4.1.4 Anti-correlated Thermal Baths

A two-photon NOON state produces Anti-correlated thermal baths. Here we connect the SPDC source from figure 28 (b) to a HOM interferometer as in figure 28 (c) that uses two delay lines to guarantee the spatial and temporal overlap between the signal and idler at the fiber beam-splitter. In this configuration, we produce the two-photon NOON state, as the dominating therm in our SPDC source is $|1,1\rangle$. It is essential to mention that this state is not a perfect thermal state. However, we are operating in the low photon number, making our state close to the one theoretically studied in [112]. For this state, we have the same situation as correlated thermal baths. Even if the states are quantum, the Demon operates just by classical correlations.

We characterized our two-photon NOON state by measuring a visibility $\nu^2 = 0.87 \pm 0.02$. It means that there is a probability of 0.87 that the pairs of photons from SPDC will bunch into a NOON state. This visibility was obtained in the HOM dip as in

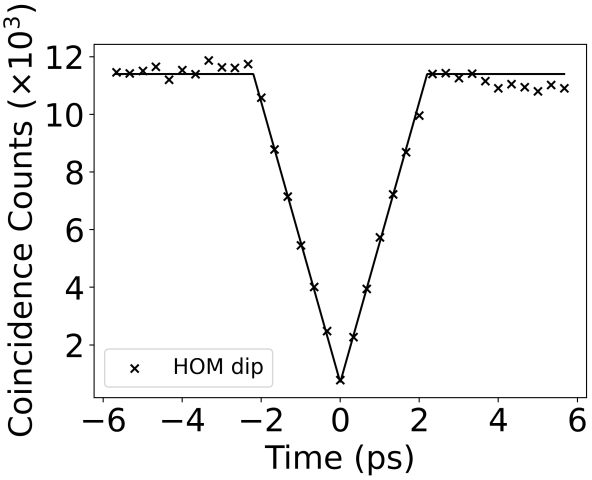

Figure 31 – This figure presents the measurement of the HOM dip for the two-photon NOON state. We obtained visibility of ν^2 = 0.87 ± 0.02 and a coherence shorter than 2 *ps* for this state.

figure 31. The coherence time of this state is shorter than 2 *ps*.

4.2 RESULTS

In this section, we present the results for our photonic Maxwell's Demon. In our experiment, we set the temperature of the thermal beams by using linear filters in the cross-state of the UFOS. After we set the temperature, we adjust the reflectivity of the tunable directional couplers. After the temperature and the reflectivity are adjusted, we perform the three measurements discussed before (cross, bar, and feed-forward), where we take measurements of 300 seconds for all sets, saving the single counts every second. We vary the reflectivity starting in 1% and then from 5% to 50% in steps of 5%.

We perform measurements with uncorrelated thermal baths in a higher photon number where the effect is more significant to guarantee that our photonic Maxwell's Demon is working. The figure 32 shows the first measurement where we have $\langle n \rangle$ = 2.71, 2.17, and 1.09, where we normalized the Demon's effect ΔN_{exp} by the coherence time. We can see that there is a clear effect that grows as $\langle n \rangle$ grows. The Demon's power grows as R grows until a limit where the Demon has a significant amount of information but no photons to deal with it, and it is power starts to decrease.

In the results from figure 32, we normalize the data by the coherence time to evaluate on average how many photons per bunch the Demon can transfer to mode A. Unfortunately, $\langle n \rangle$ is too high to be applied in theory from section 4.0.1.1.

For Uncorrelated thermal baths, considering the 5.42 μs, we measured the Demon effect for $\langle n \rangle$ = 0.151 ± 0.002, where it corresponds to an average photon number at D_A and D_B of $28,800 \pm 500$ *Hz*, where the error bars came by the standard deviation

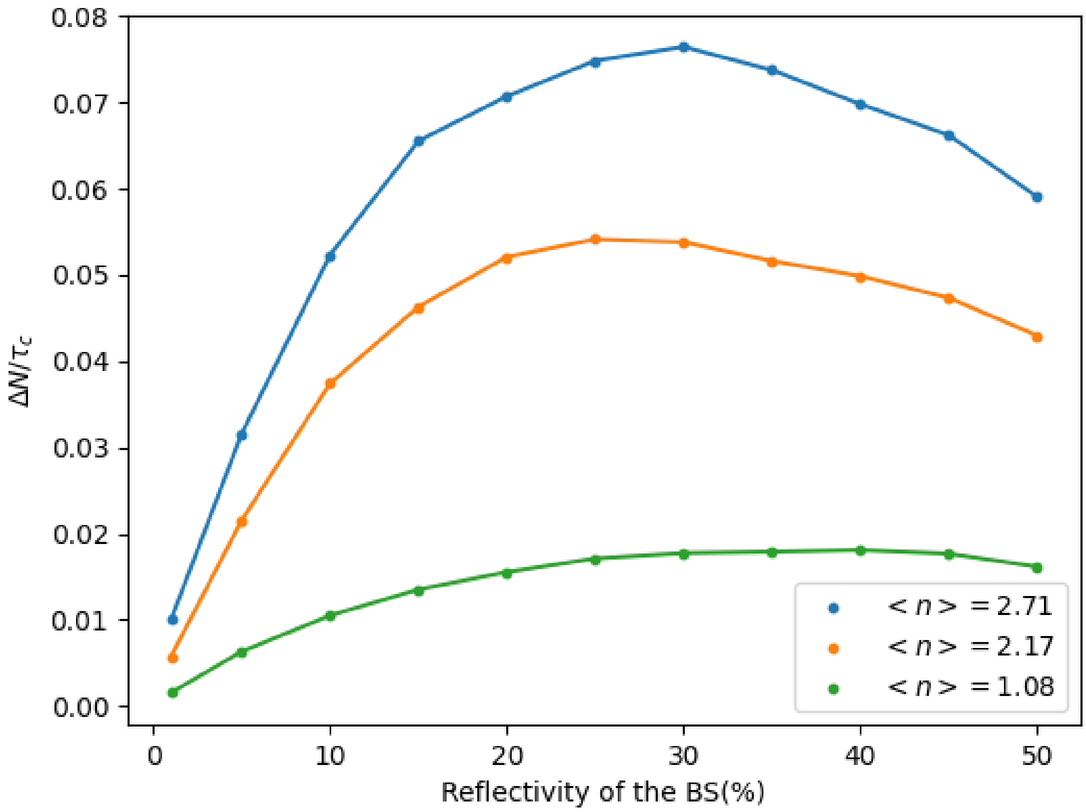

Figure 32 – First measurements of the photonic Maxwell's Demon with Uncorrelated thermal baths, where we vary the reflectivity, meaning the Demon's information, for a given $\langle n \rangle$.

of the measured single rates for the measurement set. The Demon's effect normalized by the single rate is shown in figure 33 represented by the red stars. The red line is the theory from equation 4.17, where the best parameter that fit's the experimental result is $\langle n \rangle = 0.05$. It can be due to our limited switching time in which we may cut some events, reducing the efficiency, and because of the experimental imperfections. These results are also plotted in figure 4.3 for the comparison with the results of thermal baths with correlation normalized by its correlations.

In the Split thermal state, we generate a state with $\langle n \rangle \approx 0.7$ after the division. To guarantee that the beam is still thermal, we measured the $g^2(0)$ in figure 30, showing that it tends to 2, allowing us to guarantee that the beam is still thermal. Each mode has an average photon number of $293,000 \pm 3000$ Hz. Thus, we have shown theoretically that the Demon's effect should be null. However, in the experimental results, presented as violet diamonds in figure 33, we can see the result is not precisely zero. The slight variation came from the difficulty to measure something around the noise of the system and the fact that after splitting the thermal beam, the singles are not perfectly balanced as before. It came by the fact that the fiber-based beam-splitter does not allow us to equalize the counts using linear filters. For uncorrelated thermal baths, the linear filters are set before we couple the thermal state into the fiber. Nevertheless, we can see that the result is considerably smaller than the other baths.

For the correlated thermal bath, we first measure the coupling efficiency of the source as $\epsilon^2 = 0.14$. We then balance the single rates in the modes obtaining $168,00 \pm 1000$ *Hz*, where we have a $\langle n \rangle \approx 10^{-7}$. The small $\langle n \rangle$ is due to the short coherence time of the source (around ≈ 2 *ps*), measured at the HOM interference in figure 31. The result of the Demon's efficiency normalized by the singles is shown in figure 33 as green circles. The solid green line is the theory from equation 4.34 where it agrees with the experimental data using the experimental parameters of the SPDC source.

We measure the correlations for correlated thermal bath, as the sum of the coincidence rates between $Dem_A D_A$ and $Dem_B D_A$. With these coincidence rates, we can then obtain the experimental Demon's effect normalized by the correlations that we show in figure 34 as green circles. Thus, the theory from equation 4.35 and the experimental data have a good agreement.

The last measurement set is the Anti-correlated thermal bath, where we first characterized the visibility of our two-photon NOON state as $\nu^2 = 0.87 \pm 0.02$ in figure 31. We have approximately $141,00 \pm 3000$ *Hz* singles in D_A/D_B, resulting in $\langle n \rangle \approx 10^{-7}$ due to the ≈ 2 *ps* coherence time. The experimental results normalized by the singles are shown in figure 33 as blue pentagons, and the the theory for the same regime as in equation 4.45 is the blue line. The theory with experimental parameters and the experimental results have a good agreement.

The correlations for anti-correlated baths are measured in the same way as correlated thermal baths. The only difference is that we change the term that is resulted by switching the modes. The experimental results normalized by the correlations, blue pentagons, and the theoretical results from equation 4.46, blue solid line, are shown in figure 34. As shown theoretically, the anti and correlated baths should have the same effect in the low photon regime for a perfect NOON state. However, as expected by our visibility, the Demon's power is reduced.

In figure 33 we can observe that the Demon's effect is more significant when the correlations come into consideration, even having a considerably smaller $\langle n \rangle$. Another essential point to mention is that when we normalize by the single rates, we are considering the imperfections in the pair generation. When these imperfections disappear, normalizing by the correlations, the effect grows almost two orders of magnitude. Thus, we became near to the theoretical regime where the Demon can extract 0.5 photons per bunch in the correlated thermal bath.

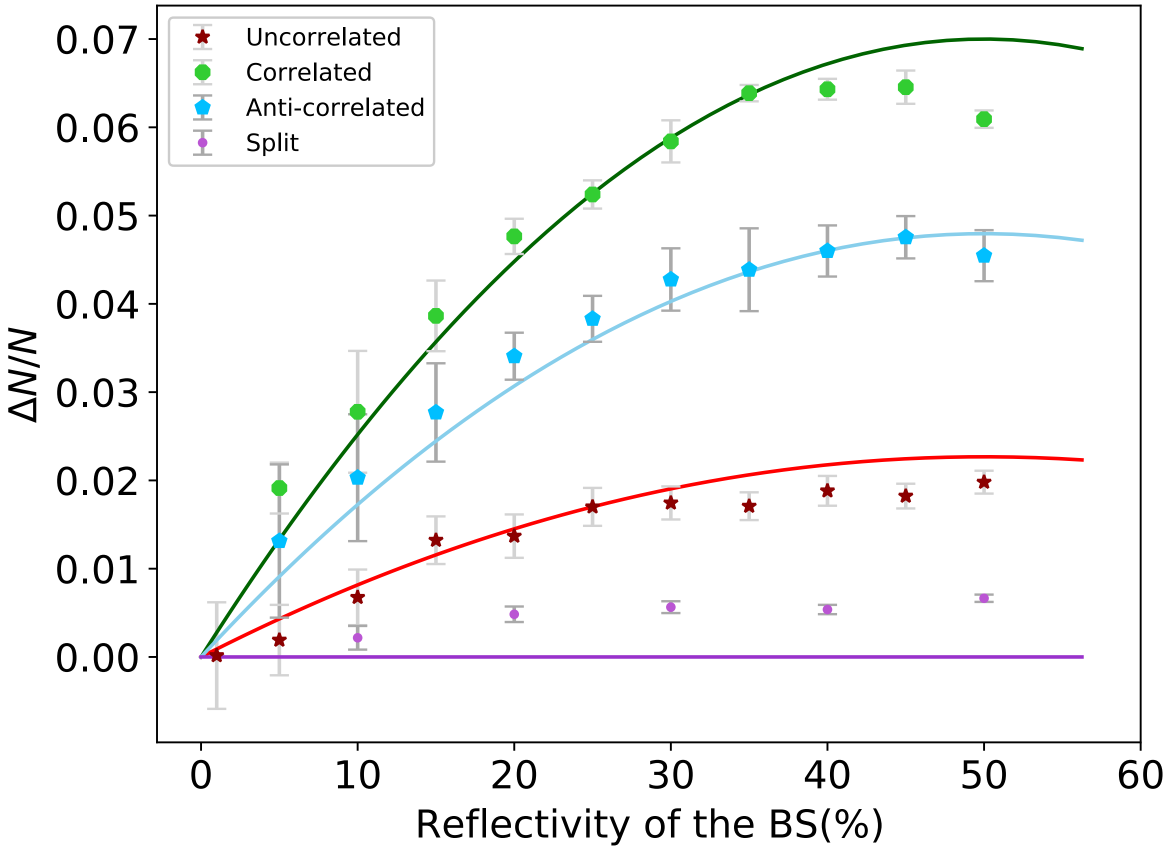

Figure 33 – Here we present the experimental results for the Demon's effect normalized by the singles rate. The experimental errors are calculated by the standard deviation of the singles in every measurement set. Better details of the experimental parameters and theoretical curve are given during the text.

4.3 CONCLUSIONS

Here we presented a photonic Maxwell's Demon that allows measuring the Demon's efficiency with no post-selection, where our feed-forward scheme acts in real-time. Another critical point of our setup is the versatility that allows us to implement various statistics using the same setup, where the only modification that needs to be done is to adapt the switching logic according to the different ways each bath provides the information for the Demon.

We can see that the experimental results for thermal baths with correlations agree with our theory without any adjustment of the parameters for the theory. Moreover, the theory has an excellent agreement for uncorrelated thermal baths when we fit the $\langle n \rangle$. However, our experimental limitations for uncorrelated thermal baths related to the switching time that is approximately half of the coherence time of our thermal beams could be the reason for the reduction in the Demon's efficiency in compassion with theory. Another possible explanation is that our theory is simplified without considering any losses or detection efficiencies that are present in the experimental scenario.

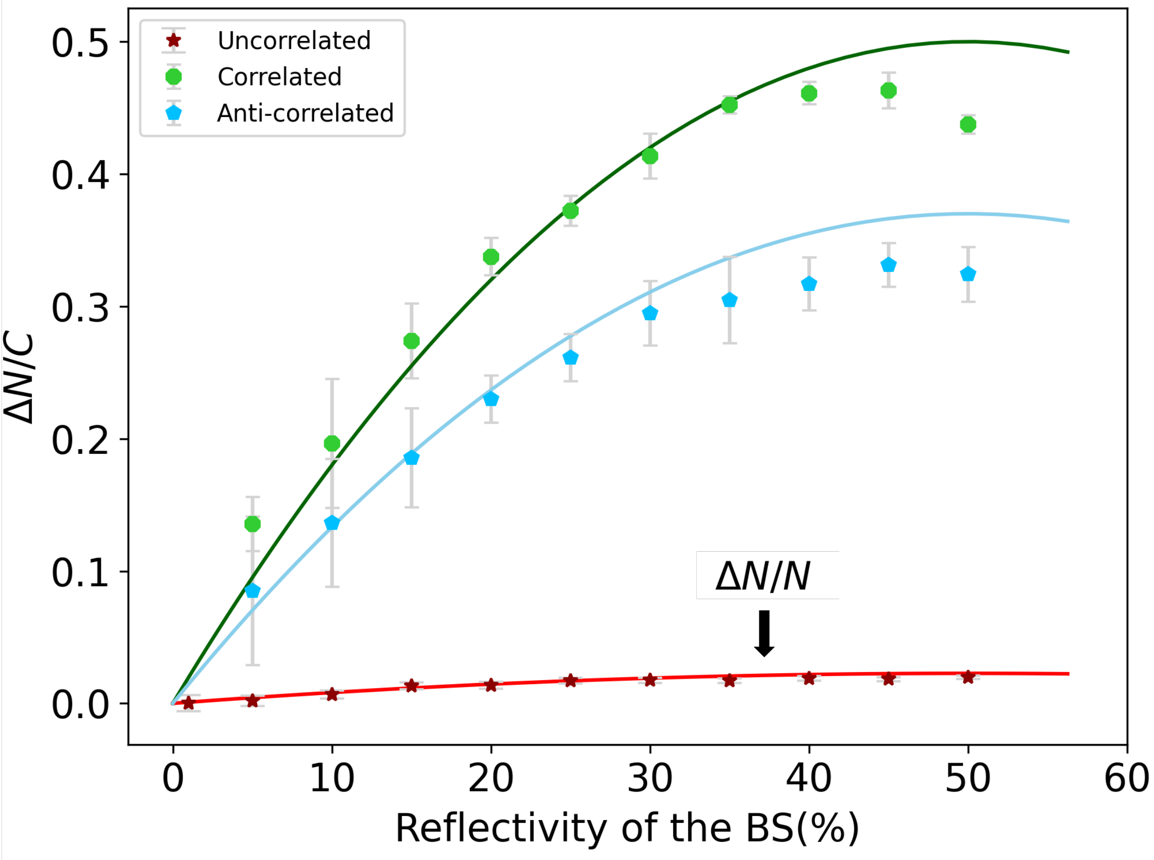

Figure 34 – Here we present the experimental results for the Demon's effect normalized by the singles rate. The experimental errors are calculated by the standard deviation of the singles in every measurement set. We also presented the result for Uncorrelated thermal baths normalized by the singles rates to make it easier the comparison between the baths with and without correlations. Better details of the experimental parameters and theoretical curve are given during the text.

We have shown that the Demon's efficiency of thermal baths with correlations overpass the efficiency with uncorrelated thermal baths when we are normalizing by the single counts, even when the $\langle n \rangle$ is smaller by several orders of magnitude. When we normalize with the correlations, the anti-correlated thermal bath have a factor of approximately 16 times bigger than the Uncorrelated. By comparing with the correlated thermal baths this factors grows to 28 times, showing the power of the classical correlations on the Maxwell's Demon protocol.

Here we show the first photonic Maxwell's Demon with active feed-forward and how these correlations could enhance the Demon's efficiency. For the low photon regime, the Correlated thermal baths are the most efficient one. However, for higher photon numbers, we expect that the anti-correlated thermal baths would be even more efficient [112]. In higher photon numbers, this protocol is applicable in fluctuation relations [111], where it is possible to extract how much information the Demon uses to extract work. This analysis is a future work where we are starting to implementing this protocol.

5 CONCLUSIONS

In this thesis, we have described experiments using optical systems aiming at building experimental platforms for the study of Quantum Thermodynamics. Optical systems allow a high degree of control over several degrees of freedom, as well as the ability of making use of quantum properties of the light like entanglement. The experiments described in the thesis deal with the orbital angular momentum of the light, photon number statistics and the polarization degres of freedom.

In chapter 2 we demonstrate the production and manipulation of thermal states using the OAM as a degree of freedom. We also study how to control the temperature of the distributions in a very simple fashion by controlling the detection area of one of the detectors. Our results show that it is possible to prepare single photons in OAM thermal states, which can be used for several purposes in Quantum Thermodynamics ranging from experimental tests of fluctuation relations to Thermodynamic cycles like thermal engines.

In chapter 3 we have demonstrated a feed-forward technique that allowed us to perform the remote state preparation at the single-photon level with the highest fidelity reported to date, to the best of our knowledge. It also demonstrates that UFOS are suitable devices to implement feed-forward protocols, as they are very fast, present low losses and easy electronic control. Another important point of this device is the possibility of application integrated to existing fiber networks. It can also be used in other applications like measurement-based quantum computation and causal order experiments.

In chapter 4, we have described the implementation of the first photonic Maxwell's Demon with active feed-forward. We have used an approach similar to the one described in chapter 3 for the feed-forward protocol, allowing us to realize the action of the demon and to measure the its power per second without post-selection. We also demonstrate how the classical correlations present in thermal baths with correlations and anti-correlation can overpass the Demon's power with uncorrelated thermal baths. We have also developed a theory for the low photon number regime, which is appropriated for our experimental conditions and agrees well with experimental results.

The perspective for futures work is to use OAM single-photon thermal states in thermodynamic processes and heat engines. This step is challenging because photons do not interact with each other and thermalization is still an issue.

The fact that we can use the UFOS to efficiently manipulate light degrees of freedom like polarization and photon number opens several perspectives for experiments on Quantum Thermodynamics that might explore the study about classical and quantum thermalization and the realization of processes to extract work efficiently from the heat. Another possibility concerns the study of the connections between informational and thermodynamic entropies, which is also related to the problem of the arrow of time.

BIBLIOGRAPHY

[1] M. Planck, “Ueber irreversible strahlungsvorgänge”, *Annalen der Physik* **1901**, *311*, 818–831.

[2] M. Planck, “Ueber das Gesetz der Energieverteilung im Normalspectrum Ann. d”, *Phys. Lpz. IV* **1901**, 553–63.

[3] A. Einstein, “Über einem die Erzeugung und Verwandlung des Lichtes betreffenden heuristischen Gesichtspunkt”, *Annalen der physik* **1905**, *4*.

[4] A. Einstein, “Strahlungs-emission und-absorption nach der Quantentheorie”, *Verh. Deutsch. Phys. Gesell.* **1916**, *18*, 318–323.

[5] A. Einstein, “Zur quantentheorie der strahlung”, *Phys. Z.* **1917**, *18*, 124.

[6] T. H. MAIMAN, “Stimulated Optical Radiation in Ruby”, *Nature* **1960**, *187*, 493–494.

[7] D. N. Klyshko, A. N. Penin, B. F. Polkovnikov, “Parametric luminescence and light scattering by polaritons”, *Soviet Journal of Experimental and Theoretical Physics Letters* **1970**, *11*, 5.

[8] D. C. Burnham, D. L. Weinberg, “Observation of simultaneity in parametric production of optical photon pairs”, *Physical Review Letters* **1970**, *25*, 84.

[9] J. D. Franson, “Bell inequality for position and time”, *Physical review letters* **1989**, *62*, 2205.

[10] J. C. Howell, R. S. Bennink, S. J. Bentley, R. W. Boyd, “Realization of the Einstein-Podolsky-Rosen paradox using momentum-and position-entangled photons from spontaneous parametric down conversion”, *Physical Review Letters* **2004**, *92*, 210403.

[11] A. Mair, A. Vaziri, G. Weihs, A. Zeilinger, “Entanglement of the orbital angular momentum states of photons”, *Nature* **2001**, *412*, 313–316.

[12] P. G. Kwiat, K. Mattle, H. Weinfurter, A. Zeilinger, A. V. Sergienko, Y. Shih, “New high-intensity source of polarization-entangled photon pairs”, *Physical Review Letters* **1995**, *75*, 4337.

[13] S. Vinjanampathy, J. Anders, “Quantum thermodynamics”, *Contemporary Physics* **2016**, *57*, 545–579.

[14] C. Jarzynski, “Nonequilibrium Equality for Free Energy Differences”, *Phys. Rev. Lett.* **1997**, *78*, 2690–2693.

[15] H. Tasaki, “Jarzynski Relations for Quantum Systems and Some Applications”, *arXiv e-prints* **2000**, cond–mat/0009244.

[16] T. B. Batalhão, A. M. Souza, L. Mazzola, R. Auccaise, R. S. Sarthour, I. S. Oliveira, J. Goold, G. De Chiara, M. Paternostro, R. M. Serra, “Experimental Reconstruction of Work Distribution and Study of Fluctuation Relations in a Closed Quantum System”, *Phys. Rev. Lett.* **2014**, *113*, 140601.

[17] S. An, J.-N. Zhang, M. Um, D. Lv, Y. Lu, J. Zhang, Z.-Q. Yin, H. T. Quan, K. Kim, “Experimental test of the quantum Jarzynski equality with a trapped-ion system”, *Nature Physics* **2014**, *11*, Article, 193.

[18] D. Marcuse, *Light transmission optics*, Robert E. Krieger, **1989**.

[19] G. L. Zanin, T. Häffner, M. A. A. Talarico, E. I. Duzzioni, P. H. S. Ribeiro, G. T. Landi, L. C. Céleri, “Experimental Quantum Thermodynamics with Linear Optics”, *Brazilian Journal of Physics* **2019**, *49*, 783–798.

[20] R. M. de Araújo, T. Häffner, R. Bernardi, D. S. Tasca, M. P. J. Lavery, M. J. Padgett, A. Kanaan, L. C. Céleri, P. H. S. Ribeiro, “Experimental study of quantum thermodynamics using optical vortices”, *Journal of Physics Communications* **2018**, *2*, 035012.

[21] P. H. S. Ribeiro, T. Häffner, G. L. Zanin, N. R. da Silva, R. M. de Araújo, W. C. Soares, R. J. de Assis, L. C. Céleri, A. Forbes, “Experimental study of the generalized Jarzynski fluctuation relation using entangled photons”, *Phys. Rev. A* **2020**, *101*, 052113.

[22] J. C. Maxwell, *Theory of heat*, Longman, **1871**.

[23] S. Toyabe, T. Sagawa, M. Ueda, E. Muneyuki, M. Sano, “Experimental demonstration of information-to-energy conversion and validation of the generalized Jarzynski equality”, *Nature Physics* **2010**, *6*, 988–992.

[24] A. Bérut, A. Arakelyan, A. Petrosyan, S. Ciliberto, R. Dillenschneider, E. Lutz, “Experimental verification of Landauer’s principle linking information and thermodynamics”, *Nature* **2012**, *483*, 187–189.

[25] J. V. Koski, V. F. Maisi, T. Sagawa, J. P. Pekola, “Experimental Observation of the Role of Mutual Information in the Nonequilibrium Dynamics of a Maxwell Demon”, *Phys. Rev. Lett.* **2014**, *113*, 030601.

[26] M. Debiossac, D. Grass, J. J. Alonso, E. Lutz, N. Kiesel, “Thermodynamics of continuous non-Markovian feedback control”, *Nature Communications* **2020**, *11*, 1360.

[27] S. Seah, S. Nimmrichter, V. Scarani, “Maxwell’s Lesser Demon: A Quantum Engine Driven by Pointer Measurements”, *Phys. Rev. Lett.* **2020**, *124*, 100603.

[28] T. Admon, S. Rahav, Y. Roichman, “Experimental Realization of an Information Machine with Tunable Temporal Correlations”, *Phys. Rev. Lett.* **2018**, *121*, 180601.

[29] B.-L. Najera-Santos, P. A. Camati, V. Métillon, M. Brune, J.-M. Raimond, A. Auffèves, I. Dotsenko, "Autonomous Maxwell's demon in a cavity QED system", *Phys. Rev. Research* **2020**, *2*, 032025.

[30] A. Kumar, T.-Y. Wu, F. Giraldo, D. S. Weiss, "Sorting ultracold atoms in a three-dimensional optical lattice in a realization of Maxwell's demon", *Nature* **2018**, *561*, 83–87.

[31] N. Cottet, S. Jezouin, L. Bretheau, P. Campagne-Ibarcq, Q. Ficheux, J. Anders, A. Auffèves, R. Azouit, P. Rouchon, B. Huard, "Observing a quantum Maxwell demon at work", *Proceedings of the National Academy of Sciences* **2017**, *114*, 7561–7564.

[32] W.-B. Wang, X.-Y. Chang, F. Wang, P.-Y. Hou, Y.-Y. Huang, W.-G. Zhang, X.-L. Ouyang, X.-Z. Huang, Z.-Y. Zhang, H.-Y. Wang, L. He, L.-M. Duan, **2018**, *35*, 040301.

[33] Y. Masuyama, K. Funo, Y. Murashita, A. Noguchi, S. Kono, Y. Tabuchi, R. Yamazaki, M. Ueda, Y. Nakamura, "Information-to-work conversion by Maxwell's demon in a superconducting circuit quantum electrodynamical system", *Nature Communications* **2018**, *9*, 1291.

[34] G. Engelhardt, G. Schaller, "Maxwell's demon in the quantum-Zeno regime and beyond", *New Journal of Physics* **2018**, *20*, 023011.

[35] M. D. Vidrighin, O. Dahlsten, M. Barbieri, M. S. Kim, V. Vedral, I. A. Walmsley, "Photonic Maxwell's Demon", *Phys. Rev. Lett.* **2016**, *116*, 050401.

[36] S. Giacomini, F. Sciarrino, E. Lombardi, F. De Martini, "Active teleportation of a quantum bit", *Physical Review A* **2002**, *66*, 030302.

[37] F. Sciarrino, M. Ricci, F. De Martini, R. Filip, L. Mišta Jr, "Realization of a minimal disturbance quantum measurement", *Physical review letters* **2006**, *96*, 020408.

[38] P. Böhi, R. Prevedel, T. Jennewein, A. Stefanov, F. Tiefenbacher, A. Zeilinger, "Implementation and characterization of active feed-forward for deterministic linear optics quantum computing", *Applied Physics B* **2007**, *89*, 499–505.

[39] X.-s. Ma, S. Zotter, J. Kofler, R. Ursin, T. Jennewein, Č. Brukner, A. Zeilinger, "Experimental delayed-choice entanglement swapping", *Nature Physics* **2012**, *8*, 479–484.

[40] J. H. Poynting, "The wave motion of a revolving shaft, and a suggestion as to the angular momentum in a beam of circularly polarised light", *Proceedings of the Royal Society of London. Series A Containing Papers of a Mathematical and Physical Character* **1909**, *82*, 560–567.

[41] M. Padgett, L. Allen, "Light with a twist in its tail", *Contemporary Physics* **2000**, *41*, 275–285.

[42] B. E. A. Saleh, M. C. Teich, *Fundamentals of Photonics*, Wiley, **1991**.

[43] L. Allen, M. Padgett, M. Babiker in, (Ed.: E. Wolf), Progress in Optics, Elsevier, **1999**, pp. 291–372.

[44] M. P. Lavery, C. Peuntinger, K. Guenthner, T. Bauer, P. Banze, D. Elser, R. W. Boyd, M. Padgett, C. Marquardt, G. Leuchs in Lasers Congress 2016 (ASSL, LSC, LAC), Optical Society of America, **2016**, LTh3B.1.

[45] M. Krenn, J. Handsteiner, M. Fink, R. Fickler, R. Ursin, M. Malik, A. Zeilinger, “Twisted light transmission over 143 km”, *Proceedings of the National Academy of Sciences* **2016**, *113*, 13648–13653.

[46] D. C. Burnham, D. L. Weinberg, “Observation of Simultaneity in Parametric Production of Optical Photon Pairs”, *Phys. Rev. Lett.* **1970**, *25*, 84–87.

[47] S. Walborn, C. Monken, S. Pádua, P. S. Ribeiro, “Spatial correlations in parametric down-conversion”, *Physics Reports* **2010**, *495*, 87–139.

[48] J. P. Torres, A. Alexandrescu, L. Torner, “Quantum spiral bandwidth of entangled two-photon states”, *Phys. Rev. A* **2003**, *68*, 050301.

[49] J. Kurchan, “A Quantum Fluctuation Theorem”, *arXiv e-prints* **2000**, cond–mat/0007360.

[50] S. Mukamel, “Quantum Extension of the Jarzynski Relation: Analogy with Stochastic Dephasing”, *Phys. Rev. Lett.* **2003**, *90*, 170604.

[51] T. Häffner, G. L. Zanin, R. M. Gomes, L. C. Céleri, P. H. S. Ribeiro, “Remote preparation of single photon vortex thermal states”, *The European Physical Journal Plus* **2020**, *135*, 601.

[52] C. H. Monken, P. H. S. Ribeiro, S. Pádua, “Transfer of angular spectrum and image formation in spontaneous parametric down-conversion”, *Phys. Rev. A* **1998**, *57*, 3123–3126.

[53] D. P. Caetano, PhD thesis, **2004**.

[54] C. K. Hong, L. Mandel, “Theory of parametric frequency down conversion of light”, *Phys. Rev. A* **1985**, *31*, 2409–2418.

[55] H. H. Arnaut, G. A. Barbosa, “Orbital and Intrinsic Angular Momentum of Single Photons and Entangled Pairs of Photons Generated by Parametric Down-Conversion”, *Phys. Rev. Lett.* **2000**, *85*, 286–289.

[56] S. Franke-Arnold, S. M. Barnett, M. J. Padgett, L. Allen, “Two-photon entanglement of orbital angular momentum states”, *Phys. Rev. A* **2002**, *65*, 033823.

[57] G. A. Barbosa, H. H. Arnaut, “Twin photons with angular-momentum entanglement: Phase matching”, *Phys. Rev. A* **2002**, *65*, 053801.

[58] J. L. W. V. Jensen, “Sur les fonctions convexes et les inégalités entre les valeurs moyennes”, *Acta Mathematica* **1906**, *30*, 175–193.

[59] S. Jevtic, D. Newman, T. Rudolph, T. M. Stace, “Single-qubit thermometry”, *Phys. Rev. A* **2015**, *91*, 012331.

[60] L. Mancino, M. Sbroscia, I. Gianani, E. Roccia, M. Barbieri, “Quantum Simulation of Single-Qubit Thermometry Using Linear Optics”, *Phys. Rev. Lett.* **2017**, *118*, 130502.

[61] M. P. Almeida, F. de Melo, M. Hor-Meyll, A. Salles, S. P. Walborn, P. H. S. Ribeiro, L. Davidovich, “Environment-Induced Sudden Death of Entanglement”, *Science* **2007**, *316*, 579–582.

[62] Maxwell’s demon, https://commons.wikimedia.org/wiki/File:Maxwell%27s$_d$*emon.svg*.

[63] G. C. G. Berkhout, M. P. J. Lavery, J. Courtial, M. W. Beijersbergen, M. J. Padgett, “Efficient Sorting of Orbital Angular Momentum States of Light”, *Phys. Rev. Lett.* **2010**, *105*, 153601.

[64] V. Parigi, A. Zavatta, M. Bellini, “Implementation of single-photon creation and annihilation operators: experimental issues in their application to thermal states of light”, *Journal of Physics B: Atomic Molecular and Optical Physics* **2009**, *42*, 114005.

[65] W. Martienssen, E. Spiller, “Coherence and Fluctuations in Light Beams”, *American Journal of Physics* **1964**, *32*, 919–926.

[66] F. T. Arecchi, “Measurement of the Statistical Distribution of Gaussian and Laser Sources”, *Phys. Rev. Lett.* **1965**, *15*, 912–916.

[67] F. Arecchi, E. Gatti, A. Sona, “Time distribution of photons from coherent and Gaussian sources”, *Physics Letters* **1966**, *20*, 27–29.

[68] M. Malik, M. O’Sullivan, B. Rodenburg, M. Mirhosseini, J. Leach, M. P. J. Lavery, M. J. Padgett, R. W. Boyd, “Influence of atmospheric turbulence on optical communications using orbital angular momentum for encoding”, *Opt. Express* **2012**, *20*, 13195–13200.

[69] B. Rodenburg, M. P. J. Lavery, M. Malik, M. N. O’Sullivan, M. Mirhosseini, D. J. Robertson, M. Padgett, R. W. Boyd, “Influence of atmospheric turbulence on states of light carrying orbital angular momentum”, *Opt. Lett.* **2012**, *37*, 3735–3737.

[70] A. Hamadou Ibrahim, F. S. Roux, M. McLaren, T. Konrad, A. Forbes, “Orbital-angular-momentum entanglement in turbulence”, *Phys. Rev. A* **2013**, *88*, 012312.

[71] L. Burger, I. Litvin, A. Forbes, “Simulating atmospheric turbulence using a phase-only spatial light modulator : research article”, *South African Journal of Science* **2008**, *104*, 129–134.

[72] R. G. Lane, A. Glindemann, J. C. Dainty, “Simulation of a Kolmogorov phase screen”, *Waves in Random Media* **1992**, *2*, 209–224.

[73] B. Rodenburg, M. Mirhosseini, M. Malik, O. S. Magaña-Loaiza, M. Yanakas, L. Maher, N. K. Steinhoff, G. A. Tyler, R. W. Boyd, “Simulating thick atmospheric turbulence in the lab with application to orbital angular momentum communication”, *New Journal of Physics* **2014**, *16*, 033020.

[74] P. Kok, W. J. Munro, K. Nemoto, T. C. Ralph, J. P. Dowling, G. J. Milburn, “Linear optical quantum computing with photonic qubits”, *Reviews of modern physics* **2007**, *79*, 135.

[75] E. Knill, R. Laflamme, G. J. Milburn, “A scheme for efficient quantum computation with linear optics”, *nature* **2001**, *409*, 46–52.

[76] A. J. F. Hayes, A. Gilchrist, C. R. Myers, T. C. Ralph, “Utilizing encoding in scalable linear optics quantum computing”, *Journal of Optics B: Quantum and Semiclassical Optics* **2004**, *6*, 533–541.

[77] N. Yoran, B. Reznik, “Deterministic linear optics quantum computation with single photon qubits”, *Physical review letters* **2003**, *91*, 037903.

[78] R. Raussendorf, H. J. Briegel, “A one-way quantum computer”, *Physical Review Letters* **2001**, *86*, 5188.

[79] P. Walther, K. J. Resch, T. Rudolph, E. Schenck, H. Weinfurter, V. Vedral, M. Aspelmeyer, A. Zeilinger, “Experimental one-way quantum computing”, *Nature* **2005**, *434*, 169–176.

[80] R. Raussendorf, D. E. Browne, H. J. Briegel, “Measurement-based quantum computation on cluster states”, *Physical review A* **2003**, *68*, 022312.

[81] H. J. Briegel, R. Raussendorf, “Persistent entanglement in arrays of interacting particles”, *Physical Review Letters* **2001**, *86*, 910.

[82] M. A. Nielsen, “Optical quantum computation using cluster states”, *Physical review letters* **2004**, *93*, 040503.

[83] H. J. Kimble, “The quantum internet”, *Nature* **2008**, *453*, 1023–1030.

[84] R. Ursin, T. Jennewein, M. Aspelmeyer, R. Kaltenbaek, M. Lindenthal, P. Walther, A. Zeilinger, “Quantum teleportation across the Danube”, *Nature* **2004**, *430*, 849–849.

[85] R. Valivarthi, S. I. Davis, C. Peña, S. Xie, N. Lauk, L. Narváez, J. P. Allmaras, A. D. Beyer, Y. Gim, M. Hussein, G. Iskander, H. L. Kim, B. Korzh, A. Mueller, M. Rominsky, M. Shaw, D. Tang, E. E. Wollman, C. Simon, P. Spentzouris, D. Oblak, N. Sinclair, M. Spiropulu, “Teleportation Systems Toward a Quantum Internet”, *PRX Quantum* **2020**, *1*, 020317.

[86] C. H. Bennett, D. P. DiVincenzo, P. W. Shor, J. A. Smolin, B. M. Terhal, W. K. Wootters, “Remote state preparation”, *Physical Review Letters* **2001**, *87*, 077902.

[87] M. K. Vijayan, A. P. Lund, P. P. Rohde, “A robust W-state encoding for linear quantum optics”, *Quantum* **2020**, *4*, 303.

[88] F. Kaneda, P. G. Kwiat, “High-efficiency single-photon generation via large-scale active time multiplexing”, *Science advances* **2019**, *5*, eaaw8586.

[89] E. Meyer-Scott, N. Prasannan, I. Dhand, C. Eigner, V. Quiring, S. Barkhofen, B. Brecht, M. B. Plenio, C. Silberhorn, Exponential enhancement of multi-photon entanglement rate via quantum interference buffering, **2019**.

[90] B. L. Higgins, D. W. Berry, S. D. Bartlett, H. M. Wiseman, G. J. Pryde, “Entanglement-free Heisenberg-limited phase estimation”, *Nature* **2007**, *450*, 393–396.

[91] L. A. Rozema, D. H. Mahler, A. Hayat, P. S. Turner, A. M. Steinberg, “Quantum data compression of a qubit ensemble”, *Physical review letters* **2014**, *113*, 160504.

[92] T. Pittman, B. Jacobs, J. Franson, “Demonstration of feed-forward control for linear optics quantum computation”, *Physical Review A* **2002**, *66*, 052305.

[93] R. Prevedel, P. Walther, F. Tiefenbacher, P. Böhi, R. Kaltenbaek, T. Jennewein, A. Zeilinger, “High-speed linear optics quantum computing using active feed-forward”, *Nature* **2007**, *445*, 65–69.

[94] V. Saggio, A. Dimić, C. Greganti, L. A. Rozema, P. Walther, B. Dakić, “Experimental few-copy multipartite entanglement detection”, *Nature physics* **2019**, *15*, 935–940.

[95] G. L. Zanin, M. J. Jacquet, M. Spagnolo, P. Schiansky, I. A. Calafell, L. A. Rozema, P. Walther, “Fiber-compatible photonic feed-forward with 99% fidelity”, *Optics Express* **2021**, *29*, 3425–3437.

[96] C. Gerry, P. Knight, P. L. Knight, *Introductory quantum optics*, Cambridge university press, **2005**.

[97] X. Peng, X. Zhu, X. Fang, M. Feng, M. Liu, K. Gao, “Experimental implementation of remote state preparation by nuclear magnetic resonance”, *Physics Letters A* **2003**, *306*, 271–276.

[98] T. Kim, M. Fiorentino, F. N. C. Wong, “Phase-stable source of polarization-entangled photons using a polarization Sagnac interferometer”, *Phys. Rev. A* **2006**, *73*, 012316.

[99] D. F. V. James, P. G. Kwiat, W. J. Munro, A. G. White, “Measurement of qubits”, *Phys. Rev. A* **2001**, *64*, 052312.

[100] M. A. Nielsen, I. L. Chuang, *Quantum Computation and Quantum Information: 10th Anniversary Edition*, 10th, Cambridge University Press, New York, NY, USA, **2011**.

[101] K. Lee, G. S. Kanter in 2018 IEEE Photonics Society Summer Topical Meeting Series (SUM), IEEE, **2018**, pp. 201–202.

[102] J.-P. W. MacLean, K. Ried, R. W. Spekkens, K. J. Resch, “Quantum-coherent mixtures of causal relations”, *Nature communications* **2017**, *8*, 1–10.

[103] D. J. Saunders, A. J. Bennet, C. Branciard, G. J. Pryde, “Experimental demonstration of nonbilocal quantum correlations”, *Science advances* **2017**, *3*, e1602743.

[104] F. Vedovato, C. Agnesi, M. Tomasin, M. Avesani, J.-Å. Larsson, G. Vallone, P. Villoresi, “Postselection-loophole-free Bell violation with genuine time-bin entanglement”, *Physical review letters* **2018**, *121*, 190401.

[105] Y. Shen, N. C. Harris, S. Skirlo, M. Prabhu, T. Baehr-Jones, M. Hochberg, X. Sun, S. Zhao, H. Larochelle, D. Englund, et al., “Deep learning with coherent nanophotonic circuits”, *Nature Photonics* **2017**, *11*, 441.

[106] A. Schreiber, A. Gábris, P. P. Rohde, K. Laiho, M. Štefaňák, V. Potoček, C. Hamilton, I. Jex, C. Silberhorn, “A 2D quantum walk simulation of two-particle dynamics”, *Science* **2012**, *336*, 55–58.

[107] J. Tiedau, E. Meyer-Scott, T. Nitsche, S. Barkhofen, T. J. Bartley, C. Silberhorn, “A high dynamic range optical detector for measuring single photons and bright light”, *Optics express* **2019**, *27*, 1–15.

[108] G. Rubino, L. A. Rozema, A. Feix, M. Araújo, J. M. Zeuner, L. M. Procopio, Č. Brukner, P. Walther, “Experimental verification of an indefinite causal order”, *Science advances* **2017**, *3*, e1602589.

[109] W. THOMSON, “Kinetic Theory of the Dissipation of Energy”, *Nature* **1874**, *9*, 441–444.

[110] L. Szilard, “über die Entropieverminderung in einem thermodynamischen System bei Eingriffen intelligenter Wesen”, *Zeitschrift für Physik* **1929**, *53*, 840–856.

[111] T. Sagawa, M. Ueda, “Second Law of Thermodynamics with Discrete Quantum Feedback Control”, *Phys. Rev. Lett.* **2008**, *100*, 080403.

[112] A. Shu, J. Dai, V. Scarani, “Power of an optical Maxwell’s demon in the presence of photon-number correlations”, *Phys. Rev. A* **2017**, *95*, 022123.

[113] G. L. Zanin, M. Antesberger, M. J. Jacquet, P. H. S. Ribeiro, L. A. Rozema, P. Walther, Enhanced Photonic Maxwell’s Demon with Correlated Baths, **2021**.

[114] K. Katamadze, G. Avosopiants, Y. I. Bogdanov, S. Kulik, “How quantum is the “quantum vampire” effect?: testing with thermal light”, *Optica* **2018**, *5*, 723–726.

[115] A. Zavatta, V. Parigi, M. Kim, M. Bellini, “Subtracting photons from arbitrary light fields: experimental test of coherent state invariance by single-photon annihilation”, *New Journal of Physics* **2008**, *10*, 123006.

[116] R. Loudon, *The quantum theory of light*, OUP Oxford, **2000**.

[117] B. Yurke, M. Potasek, “Obtainment of thermal noise from a pure quantum state”, *Physical Review A* **1987**, *36*, 3464.

[118] B. Blauensteiner, I. Herbauts, S. Bettelli, A. Poppe, H. Hübel, “Photon bunching in parametric down-conversion with continuous-wave excitation”, *Physical Review A* **2009**, *79*, 063846.

[119] I. Afek, O. Ambar, Y. Silberberg, “High-NOON states by mixing quantum and classical light”, *Science* **2010**, *328*, 879–881.

[120] L. A. Rozema, J. D. Bateman, D. H. Mahler, R. Okamoto, A. Feizpour, A. Hayat, A. M. Steinberg, “Scalable spatial superresolution using entangled photons”, *Physical review letters* **2014**, *112*, 223602.

[121] W. Martienssen, E. Spiller, “Coherence and fluctuations in light beams”, *American Journal of Physics* **1964**, *32*, 919–926.

[122] F. T. Arecchi, “Measurement of the statistical distribution of Gaussian and laser sources”, *Physical Review Letters* **1965**, *15*, 912.

[123] F. Arecchi, E. Gatti, A. Sona, “Time distribution of photons from coherent and Gaussian sources”, *Physics Letters* **1966**, *20*, 27–29.

[124] R. H. Brown, R. Q. Twiss, “Correlation between photons in two coherent beams of light”, *Nature* **1956**, *177*, 27–29.

[125] R.-B. Jin, R. Shimizu, K. Wakui, M. Fujiwara, T. Yamashita, S. Miki, H. Terai, Z. Wang, M. Sasaki, “Pulsed Sagnac polarization-entangled photon source with a PPKTP crystal at telecom wavelength”, *Optics Express* **2014**, *22*, 11498–11507.